Metabolic alterations in Charcot-Marie-Tooth disease type 1A

Dissertation

for the award of the degree

“Doctor rerum naturalium” (Dr. rer. nat.)

of the Georg-August University Göttingen

within the doctoral program Biology

of the Georg-August University School of Science (GAUSS)

Submitted by

Lisa Linhoff

born in Frankfurt am Main, Germany

Göttingen, 2020

Thesis Committee

Members of the Examination Board

Prof. Dr. Michael Sereda (Reviewer)
Molecular and Translational Medicine
Max-Planck Institute of Experimental Medicine, Göttingen

Department of Clinical Neurophysiology and Neurology
University Medical Center Göttingen (UMG), Göttingen

Prof. Dr. Susann Boretius (Second Reviewer)
Functional Imaging
German Primate Center (DPZ), Göttingen

Prof. Dr. Ralf Heinrich
Cellular Neurobiology
Johann-Friedrich-Blumenbach-Institute for Zoology and Anthropology, Göttingen

Further members of the Examination Board

Prof. Klaus-Armin Nave, PhD
Neurogenetics
Max-Planck Institute of Experimental Medicine, Göttingen

Prof. Dr. Dr. Hannelore Ehrenreich
Clinical Neuroscience
Max-Planck Institute of Experimental Medicine, Göttingen

Prof. Dr. Christine Stadelmann-Nessler
Neuropathology
University Medical Center Göttingen (UMG), Göttingen

Date of the oral examination: 31st March 2021

Declaration

I hereby declare that the PhD thesis entitled “Metabolic alterations in Charcot-Marie-Tooth disease type 1A” was written independently and with no other sources and aids than quoted.

Göttingen, 30.12.2020

“I open at the close.”

Deathly Hallows, J.K. Rowling

Acknowledgements

First and foremost, I would like to thank my supervisor Prof. Dr. Michael Sereda for giving me the opportunity to work on this project. Thank you for scientific discussions and guidance in letting me form ideas and hypothesis around this topic and giving me the possibility to explore so many techniques.

Secondly, I would like to thank Prof. Klaus-Armin Nave for the possibility to work in his department and his scientific input and discussions. I want to extend my gratitude to Prof. Dr. Paulus for giving me the opportunity to work on this project.

I would like to extend my appreciation to my Thesis Advisory Committee members, Prof. Dr. Susann Boretius and Prof. Dr. Ralf Heinrich. Thank you for all the advice and input during the Progress Reports of this thesis.

Additionally, I would like to thank the members of the Extended Committee Prof. Klaus-Armin Nave, Prof. Dr. Dr. Hannelore Ehrenreich and Prof. Dr. Christine Stadelmann-Nessler for taking the time to participate in the process of my thesis and on this special day.

My gratitude goes to Dr. Theresa Kungl. Thank you for introducing me to the work on the peripheral nervous system and sharing your excitement for Schwann Cells with me. Thank you so much for discussing this project time and again and for helping in “the final hours” of this thesis, even during Christmas. Thank you, that hours outside the lab, under the water, were equally fun.

I want to thank Dr. Andrea Trevisiol for introducing me to FLIM measurements and that frustration levels do not mean anything. Thank you for bearing with me, when all I saw was whiny scripts.

My thank goes to Dr. David Ewers and Dr. Markus Schwab for scientific discussions and input for this thesis.

Big thanks goes to the entire PNS group, to Christian Maack, Christian Wieczoreck, Beate Veith, Lorenz Winter and Michael Kothe for all your technical support in the lab. Doris Krauter, Theresa Kungl and Stephanie Wernick for making the lab a place to feel comfortable in and for sharing so many laughs while huge experimental days seemed too long to fit into a single day. Doris, thank you for sharing every step of our PhD time. From the first day in the lab to finally submitting in the midst of a pandemic.

I am so grateful for being able to share my project with Katrin Haase during her master thesis. Thank you for all the work and fun hours during your thesis.

Many thanks go to the entire Neurogenetics department for such a nice atmosphere in the lab. Especially to Kathrin Kusch for crisis solving help in the lab and outside of the lab. Thanks to Annette Fahrenholz, Torben Ruhwedel, Dr. Wiebke Möbius and Dr. Miso Mitkovski for help around histology, electron microscopy and light microscopy.

I want to thank all collaborators on this project for the help on this work: Dr. Karsten Hiller, Dr. Joris van Dort, Dr. Katrin Willig, Dr. Nirmal Kannaiyan, Prof. Dr. Moritz Rossner and the investigators, technical staff and coordinator of study centers of the German CMT-NET.

Many thanks go to...

… Dr. Anke Schräpler, Dr. Ursula Fünfschilling and Dr. Sarah Kimmina for support on mouse work, breeding and TVAs.

… all animal care takers, Sarah Schulze, Tanja Hoffmeister, Dennis Funk, Marion Wehe and Kerstin Claus for making the animal work much easier.

… the IT department, Martin, Rolf, Hajo, Lothar and Beate for all assistance around crashing software.

… Michaela Schmalstieg and Marion Kurze for administrative help. Thank you Ela for rescue missions and fun lunch breaks.

… all “positive possums” and PhDs from the MPI-EM for a cheerful Community at the institute and the department.

… Lena, Maria, Constanze and Stefan for food supply, discussions and outside the lab hours, which gave me new motivation.

… my family most importantly. Thank you Mama and Papa for loving and supporting me every step of the way and giving me a safe space to return to no matter what. Thank you Kathi and Jan Ole for making “Geschwisterding” a thing and your continuous support.

… especially Thomas for supporting me, even when I got close to being crazy. Thank you for making sure, that I ate and took a break every once in a while. I am so grateful, that you are there!

Table of Content

List of Figures and Tables

Abbreviations

aCSF:	Artificial cerebrospinal fluid
Akr1b1:	Aldose reductase
AR:	Aldose reductase
AraC:	Cytosine β-D-arabinofuranoside hydrochloride
ATP:	Adenosine triphosphate
BPE:	Bovine pituitary extract
BSA:	Bovine serum albumin
CAP:	Compound action potential
Caspr:	Contactin-associated protein
CDA:	Cytidine deaminase
CMAP:	Compound action muscle action potential
CMAP:	Compound muscle action potential
CMT1A:	Charcot-Marie-Tooth disease type 1A
CMT-FOM:	CMT functional outcome measure
CMTNS:	CMT neuropathy score
CMTPedS:	CMT pediatric scale
Cnp:	2',3'-, Cyclic 3'- phosphodiesterase
CNS:	Central nervous system
COX:	Cytochrome C oxidase
Ctrl:	Control
CTSA:	Cathepsin A
DB-cAMP:	2'- O- Dibutyryladenosine- 3', 5'- cyclic monophosphate
DTT:	Dithiothreitol
E:	Embryonic day
ENPP1:	Ectonucleotide pyrophosphatase/phosphodiesterase 1
FCS:	Fetal calf serum
FRET:	Förster or fluorescence resonance energy transfer
Fru:	Fructose
G6pd:	*Glucose-6-phosphate dehydrogenase*
Glc:	Glucose
GLUT:	Glucose transporter
Gly:	Glycogen
GSTT2:	Glutathione S-transferase theta 2
Gys1:	*Glycogen synthase*
Hk1:	Hexokinase1
IENFD:	Intra epidermal nerve fiber density
IRF:	Instrument response function
JXP:	Juxtaparanode
KO:	Knockout
K&S:	Karlsson & Schulz
K^+:	Potassium
Lac:	Lactate
Lkb1:	Liver kinase 1B
Mag:	Myelin-associated glycoprotein

Mbp:	Myelin basic protein
MCT:	Monocarboxylate transporters
MGB:	Modified Gitschier buffer
Mpz:	Myelin protein zero (P0)
mtCo1:	*Mitochondrial encoded cytochrome C oxidase I*
Nav1.6:	Voltage-gated sodium (Na^+)
NEM:	*N*-Ethylmaleimide
Nf:	Neurofascin
NfL:	Neurofilament light chain
NGF:	Neuronal growth factor
NRG:	Neuregulin
NT:	Neurotrophin
ONLS:	Overall neuropathy limitation score
P:	Postnatal day
PB:	Phosphate buffer
PCR:	Polymerase chain reactions
Pfkm:	*Phosphofructokinase M*
PLL:	Poly-L-lysine
Plp1:	Proteolipid protein
PMP22:	Peripheral myelin protein 22
PNS:	Peripheral nervous system
PPARG:	Peroxisome proliferator-activated receptor gamma
Prx :	Periaxin
PVDF:	Polyvinylidene diuoride
Pygb:	*Glycogen phosphorylase B*
Pyr:	Pyruvate
qRT-PCR:	Quantitative real time polymerase chain reaction
ROS:	Reactive oxygen species
SC:	Schwann cells
SCP:	Schwan cell precursor
Slc2a1:	*Solute carrier family 2 member 1*
SLI:	Schmidt-Lanterman incisures
Tag:	Transient axonal glycoprotein
TCA:	Tricarboxylic acid cycle
Tfam:	*Mitochondrial transcription factor A*
TGF:	Transforming growth factor
TMPRSS5:	Transmembrane protease serine 5
V:	Visit
W:	Weeks
WT:	Wildtype

1. Abstract

Axo-glia interaction extend beyond myelination itself. Glial cells support axons with metabolites and trophic factors. In numerous disease models, primary glial mutations result in the disturbance of normal nerve conduction. In Charcot-Marie-Tooth disease type 1A (CMT1A), an overexpression of peripheral myelin protein 22 (PMP22) in Schwann cells (SC), the myelinating glial cells of the peripheral nervous system, results in severely reduced nerve conduction velocities and eventually loss of compound muscle action potentials (CMAP) in patients as well as in a rat model (*Pmp22^{tg}*). Previous studies have reported that reduced axonal numbers and alterations in mRNA expression of the metabolic machinery correlate with disease severity. Recent evidence implicating failed metabolic support in other models of peripheral neuropathies highlight its importance for functional axo-glial interaction. Here, we hypothesize that in CMT1A the challenged SC is no longer able to metabolically support axonal function. In a metabolomics approach complemented with qRT-PCR analysis in nerve lysates of *Pmp22^{tg}* animals alterations in glucose metabolism were observed. Interestingly, free glucose was enriched while a downregulation of the polyol pathway was observed and no increase of glycogen storages or glycolysis machinery was detected. Glucose transporter1 was increased and localized to Schmidt-Lanterman Incisures as well as the ab- and adaxonal SC surface possibly allowing for the shuttling of free glucose to the axon. We hypothesize that free glucose concentrations fuel the axonal metabolism in peripheral nerves of *Pmp22^{tg}* animals. Mitochondria of diseased axons showed morphological alterations and adenosine triphosphate (ATP) levels of axons in old *Pmp22^{tg}* animals decreased as compared to wild type animals. The expression of the mitochondrial gene *COX6C* detected in blood of CMT1A patients correlated with handgrip strength underlining the importance of mitochondrial alterations in disease pathogenesis. Our data suggest that free glucose is not primarily metabolized in SC, but instead is transported to the axons to meet metabolic demands. During the course of the disease, the increased supply becomes deleterious as a potential axonal glucose overload might drive axonal loss, neuromuscular junction degeneration and muscle atrophy. Understanding the details of axo-glial metabolic coupling in health and its alteration in diseases may promote novel therapeutic targets.

2. Introduction

The central nervous system (brain and spinal cord, abbrev. CNS) and the peripheral nervous system (peripheral nerves, abbrev. PNS) collaborate to perceive stimuli from the outside world, integrate them into respective circuits and initiate appropriate actions in response to the stimuli (Nave & Werner 2014).

In large vertebrates, some of these peripheral nerves are up to several meters long and myelin, an co lipid rich membrane is wrapped around axons to enable rapid impulse propagation (Nave & Werner 2014). Myelin insulates the axons thus restricting action potentials during impulse propagation to only short stretches of unmyelinated segments (nodes of Ranvier) leading to so called saltatory conduction (Nave & Werner 2014, Tasaki 1939). Myelin is formed and maintained by glial cells, the second cell type of the nervous system next to neurons. Besides myelination, glial cells fulfill a multitude of other tasks in the central and peripheral nervous system, as trophic and metabolic support, homeostasis or immunological functions. In the CNS, astrocytes play a role in the blood-brain-barrier and surround synapses where they help to clear neurotransmitters and play a role in metabolic support. Microglia function as resident macrophage-like cells in the CNS, whereas oligodendrocytes form myelin and metabolically support the axons. On the other hand, in the PNS with regard to axonal integrity all those functions are fulfilled by Schwann cells, with a specialized SC type. They form myelin and support the axon with metabolic and trophic factors. Satellite cells cover autonomic ganglia and sensory cell bodies in ganglia, while neuromuscular junctions (the connection between axons and muscles) are in contact with terminal glia cells, which play a role in stability and synaptic transmission (reviewed in (Jessen 2004)). Henceforth, this thesis will focus on Schwann cells and their respective roles in peripheral nerves.

2.1. Schwann cells, the superheroes of the PNS

Schwann cells develop from neural crest cells over Schwan cell precursor (SCP) to immature SC to become myelinating or non-myelinating Schwann cells. They play an important role in neuronal survival during development and in repair responses after nerve injury (Bao et al 2003, Jessen 2004, Jessen & Mirsky 2002). Additionally, it has been suggested that Schwann cells provide trophic and metabolic support to axons (Nave 2010).

2.1.1. Myelin structure

Myelin is the extension of the Schwann cell membrane, which wraps spirally around the axon. 70%-75% of the membrane's dry weight is made up by lipids (Norton & Poduslo 1973). The main myelin proteins of the PNS are P0 (*Mpz*; 44% of protein), Periaxin (*Prx*; 15%), Myelin basic protein (*Mbp*; 18%), 2',3'-, Cyclic 3'-phosphodiesterase (*Cnp*; 0.33%), Myelin-associated glycoprotein (*Mag;* 0.2%) and Proteolipid protein (*Plp1*; 0.17%) (Siems et al 2020). SC cover one internode along the axon each. Between adjacent SC nodes of Ranvier are formed. The longitudinal edges of SC are specialized structures that attach the SC to the axon, forming so called para- and juxtaparanode.

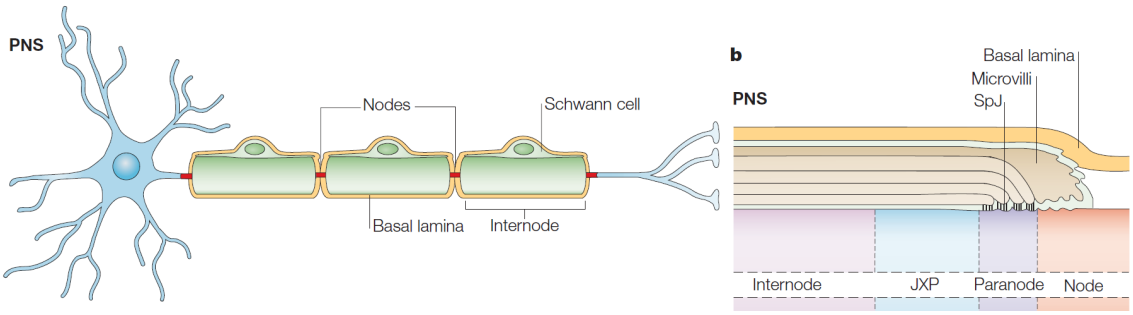

Figure 1: Structure of peripheral nerve fibers. One class of fibers is covered by Schwann cells producing a compacted myelin sheath forming an Internode (left side). Between the adjacent Internodes, Nodal regions are formed made up of Juxtaparanode (JXP), Paranode and Node (right side). The node is contacted by microvilli extended from the Schwann cell and all is covered by the basal lamina. Figure is taken from Poliak & Peles 2003.

Figure 1 displays the resulting structure of nodes, paranodes and juxtaparanodes, which is formed by tightly regulated axonal and SC specializations (Poliak & Peles 2003). In the PNS, Schwann cells produce a basal lamina and cover the nodes with microvilli (Landon & Langley 1971, Poliak & Peles 2003). Along the axon, neighboring Schwann cells are connected by tight junctions (Berthold & Rydmark 1983, Poliak et al 2002). At the nodes, necessary voltage-gated sodium (Na^+) Nav1.6 (and sometimes Nav1.9) channels are clustered in the axonal membrane. (Caldwell et al 2000, Fjell et al 2000). Additionally, other cytoskeletal or transmembrane proteins are localized to the nodal region, e.g. Ankyrin G or neurofascin 186 to stabilize this complex structure (Davis et al 1996, Kordeli et al 1990). At the paranode the single myelin wraps end in cytoplasm filled paranodal loops that are connected to the axonal membrane by septate-like junctions, which are, formed between contactin 1, contactin-associated protein (Caspr) 1 and the glial neurofascin (Nf 155) (Boyle et al 2001, Pillai et al 2009, Stathopoulos et al 2015, Tao-Cheng & Rosenbluth 1983). The following juxtaparanode

is known to have potassium (K^+) channels ($K_v1.1$, K_v 1.2) which are, following speculations, important for the upkeep of the axonal resting potential. In addition, Caspr2, transient axonal glycoprotein (Tag) 1 and connexin 29 localize there as well (Altevogt et al 2002, Li et al 2002, Traka et al 2002). The following internode and the juxtaparanode are consist of compact myelin. Compacted areas contain no cytoplasm and are stacked layers of inner and outer cell membrane. Part of the structure are also uncompacted myelin regions, which are filled with cytoplasm, the already mentioned paranodal loops, the innermost (adaxonal), the outermost (abaxonal) layer and the Schmidt-Lanterman incisures (SLI), which connect the two layers, thereby providing putative transport routes for e.g. metabolic support (Arroyo & Scherer 2000, Nave & Werner 2014).

2.1.2. The Schwann cell journey - from the neural crest via radial sorting to myelination

Schwann cells originate from neural crest cells during early embryonic development and differentiate via two transitions to mature Schwann cell subtypes. The stages, depicted in **Figure 2**, follow a tightly regulated path.

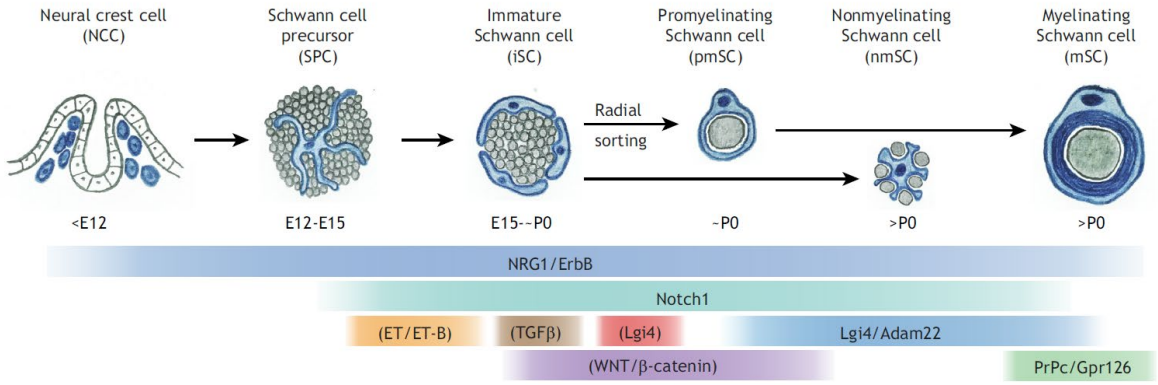

Figure 2: The developmental path of Schwann cells from the neural crest. The numerous stages in development of Schwann cells and the two subgroups formed. The day in development of mice and the marker expressed at the respective stage are indicated. Figure is taken from Fledrich et al 2019.

Neural crest stem cells migrate in the mesenchyme to their target nerves where they form SCP at embryonic day (E) 14-15 in rats (mouse E12-13) (Le Douarin et al 1991). These SCPs differ in their glial-like phenotype to their precursors, the obvious one being the first time the lineage is in close contact with axons (Jessen & Mirsky 2019). At this time, they change the expression of several genes (Buchstaller et al 2004). Another difference is their high dependence on neuregulin (NRG) 1 type III expression

on axons and the interaction with the ErbB2/ErbB3 receptor for their survival and migration. The positive effect on survival is amplified by Notch expression in SCP (Birchmeier 2009, Birchmeier & Nave 2008, Lyons et al 2005, Taveggia et al 2005, Winseck & Oppenheim 2006, Woodhoo et al 2009). At E17-18 in rats (15-16 in mice) SCP further develop into immature Schwann cells that can be found until around the time of birth. This switch is positively influenced by NRG1 type III and Notch signaling (Dong et al 1995, Woodhoo et al 2009). A negative regulation on the transition is endothelin signaling, as a knockout of the receptor leads to an earlier appearance of immature Schwann cells (Brennan et al 2000). The major differences to the preceding stage is their ability to survive in an autocrine survival loop manner (e.g. IGF2, NT3, PDGF-B) and the formation of a basal lamina (Dong et al 1995, Jessen et al 1994, Meier et al 1999, Wanner et al 2006). Besides immature SC, SCPs also give rise to fibroblasts, demonstrating a multipotency of SCP (Jessen & Mirsky 2005, Joseph et al 2004). At the stage of immature Schwann cells, several mechanisms are controlling for an appropriate Schwann cell number in comparison to the existing axons. Transforming growth factor (TGF) β with the TGFβ type II receptor has been shown to induce Schwann cell death at this stage (D'Antonio et al 2006). On the other hand, when interfering with HDAC1/2 during embryonic development, cell death amongst Schwann cells is observed right after birth (Jacob et al 2011). SPCs and immature Schwann cells have been shown to impact neuronal survival positively as well, as shown in mutants interfering with *Sox10* or NRG1 signaling. Additional developmental steps that fail in these mutants are fasciculation and the proper formation of the neuromuscular junction (Britsch et al 2001, Riethmacher et al 1997, Woldeyesus et al 1999, Wolpowitz et al 2000). Fasciculation means groups of fibers are bundled together and surrounded by the so-called perineurium (connective tissue). All smaller bundles are then held together by the surrounding epineurium. Since fasciculation is impaired it is heavily hypothesized, that NRG1 also plays a role in a process called radial sorting (Feltri et al 2016). Radial sorting starts at the stage of immature Schwann cells and continues until postnatal day (P) 10 in rodents. At the initial stage, immature Schwann cells form a border around a group of axons and organize a basal lamina around them. Immature Schwann cells then start to elongate processes towards the axons and start sorting out the bigger axons. By proliferation the immature Schwann cells make smaller bundles until the larger axons are in a 1:1 relationship with so called pro-myelin Schwann cells, which go on to myelinate the axons larger than 1µm in

diameter. This group of fibers includes A fibers, known to mediate motor functions, and C fibers, known to mediate the faster sensory signals. The slower sensory fibers are the axons smaller than 1µm, which stay in the bundles covered by non-myelinating Schwann cells forming Remak-bundles (Feltri et al 2016, Jessen & Mirsky 2005, Webster et al 1973). Schwann cells integrate the signal of axonal NRG1 type III abundance via ErbB2/ErbB3 to sense axon caliber as key signal for myelination and myelin sheath thickness (Lyons et al 2005, Michailov et al 2004, Nave & Werner 2014, Riethmacher et al 1997, Taveggia et al 2005, Woldeyesus et al 1999). Particularly in myelinating SC lipid biosynthesis, translation and precise trafficking of myelin proteins is important. Disturbances in the highly regulated processes can lead to neuropathies (Fledrich et al 2018, Fledrich et al 2012b). While axonal signals play a role in regulating myelin sheath thickness there are evidences for a regulation of axonal caliber size by Schwann cell proteins (Eichel et al 2020, Yin et al 1998).

2.1.3. Schwann cell - axon interactions

As already mentioned, interactions of glial cells and axons go beyond the event of myelination itself. Schwann cells dedifferentiate into repair cells during acute injury (reviewed in (Jessen & Mirsky 2016)) and there has been emerging evidence for metabolic and trophic support (Nave 2010). From an evolutionary view, glia-like cells have emerged before the occurrence of myelin. In the lamprey unmyelinated axons are arranged in a Remak-bundle like structure and are associated with a glia-like cell type. This suggests an axonal support function beyond myelin itself (Bouçanova & Chrast 2020, Weil et al 2018). Especially when keeping the structure of the fibers in mind. Axons are covered completely by SC membranes keeping them completely from outside molecules like metabolites, highlighting the need for a support route. Evidence towards separating myelination from axonal support has been emerging from several studies and an uncoupling of these events has been suggested (Nave 2010). In models of *Cnp* deficient animals, axons in the CNS appear to be myelinated normally with the only alteration reported to be enlarged inner tongues of oligodendrocytes. Nonetheless, axons degenerate, a phenomenon thought to be due to disruption of axo-glial coupling (Edgar et al 2009, Lappe-Siefke et al 2003, Rasband et al 2005). In the PNS, when disrupting liver kinase B1 (LKB1) in Schwann cells of adult mice, axon degenerate without a myelination defect (Beirowski et al 2014). It seems, even if intact myelin is provided, axons can lack support of glial cells, e.g. metabolic factors.

Additionally, axons seem to be able to survive without myelin providing normal axo-glial coupling. In a study of chronic demyelination in the CNS, no axonal degeneration was observed despite severe demyelination (Smith et al 2013). In studies of mice lacking cholesterol synthesis in oligodendrocytes and SCs, myelin was not formed due to improper transport of P0. However, no axonal degeneration was observed in PNS or CNS (Saher et al 2009). Taken together, Schwann cells perform several independent support functions for the underling axon, which will be discussed in the following.

2.2. Schwann cell functions beyond myelination

In the CNS, oligodendrocytes have been shown to be important for the metabolic support of axons (Fünfschilling et al 2012, Lee et al 2012) and a model has been proposed to explain metabolic support of neurons. The so called ‘lactate shuttle’ proposes, that astrocytes and oligodendrocytes take up glucose where it is metabolized to pyruvate/lactate during glycolysis. Lactate is presumed to be transported to the neuron, where it can be used by mitochondria in oxidation (Fünfschilling et al 2012, Pellerin & Magistretti 1994). Axons of the PNS are shielded quite well from the surrounding, as depicted in **Figure 3**. Metabolites need to be taken up from blood vessels within the nerve. Similar as in the CNS, a blood-nerve-barrier covers the blood vessels. Single fascicle are covered by connective tissue, the perineurium and single fibers are shielded by the endoneurium (Jha & Morrison 2018). As mentioned, in the PNS are no astrocytes in comparison to the CNS. Seeing that neuronal cell bodies are sometimes long distances away, axons are depending on the support of SCs in contact to supply them with metabolites. In the following, experimental evidence towards metabolic support by SCs in the PNS will be discussed.

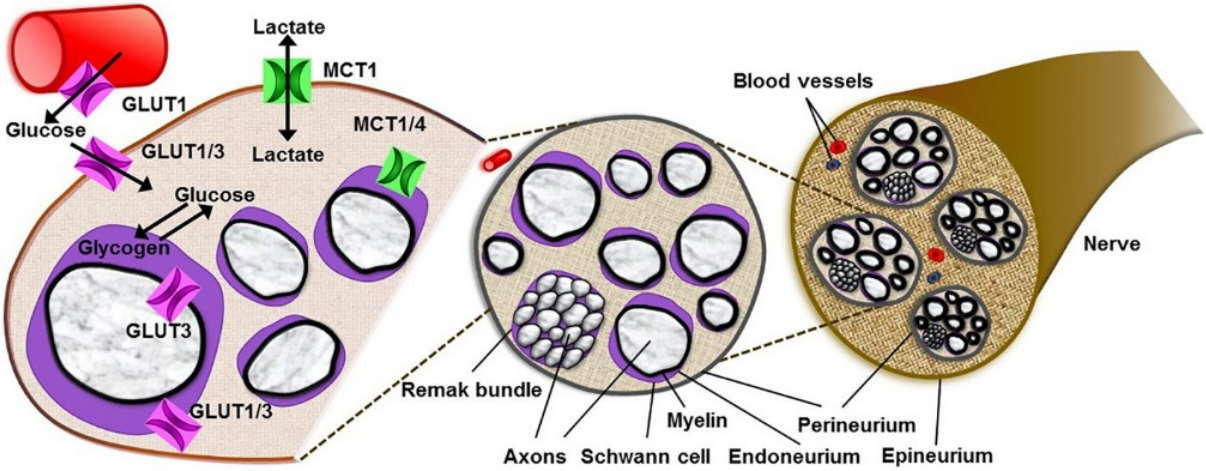

Figure 3: Morphology of peripheral nerve fibers. Single axons are covered by myelin, shielding it from the surroundings. GLUT1/3 have been localized to the peripheral nerve. Glucose is taken up from vessels and transported into the fibers. Several axons and Remak bundles are grouped together in fascicles, which are covered by perineurium. One nerve is made up of several fascicles, which are covered by epineurium. Figure is taken from Jha & Morrison 2018.

2.2.1. Transporter in SLIs of Schwann cells

Even though most of the myelin sheath is compacted, parts of the Schwann cell remain non-compacted, cytoplasmic regions. As already mentioned this is the case for the ab- and adaxonal layers (inner and outer tongue) and the SLIs. These regions would be a suitable route of transport for metabolites. Interestingly, transporters known from the CNS can be found in the PNS as well (Jha & Morrison 2018) such as Monocarboxylate transporters (MCT). MCT1 has been localized to the SLIs and paranodal loops while MCT4 can be found in the cajal bands and the SC cytoplasm. Additionally, MCT1 was found in DRG neurons, whereas MCT2 could not be localized yet even though it is expressed in peripheral nervous tissue (Domènech-Estévez et al 2015, Morrison et al 2015). Glucose transporters (GLUT) 1 and 3, similar to the CNS, have been proposed to be the primary glucose transporters in peripheral nerves as well. GLUT1 localizes to SLI and paranodal regions. GLUT3 was localized to paranodal regions in aged animals and has been shown to be the primary neuronal transporter (Magnani et al 1996, Muona et al 1992, Stuart et al 2000). Interestingly, GLUT3 has been shown to have a greater affinity for glucose as GLUT1 and higher transport capacity as well (Simpson et al 2008). Additionally, Connexin32 and 29 have been localized to several sites of SCs forming Gap Junctions and thereby connecting SC Cytoplasm with other

non-compact regions via SLIs (Cisterna et al 2019). Adjacent cells have been reported to be connected by tight junctions (Poliak et al 2002, Poliak & Peles 2003).

2.2.2. Substrates

So far, a few *ex vivo* studies have been published that evaluate the ability of different substrates to support peripheral nerve compound action potential (CAP) propagation. Sciatic nerves survive in **glucose** baths *ex vivo*, the efficiency of which is influenced by the substrate concentration in the medium (Brown et al 2012, Stecker & Stevenson 2014). Myelinating SCs store excess glucose as **glycogen** and are able to use it under substrate free conditions, which makes A fibers less susceptible to CAP failure than C fibers (Brown et al 2012). **Lactate** has been shown to be released during activity of axons and seems to be equally efficient as glucose in upholding A fiber CAP, while it is lacking in efficiency for C fibers (Brown et al 2012). In a study from Rich and Brown (2018), blocking lactate transport *ex vivo,* leads to the failure of fructose to support A fiber CAP. **Fructose** only supports the A fiber CAP in high concentrations while C fibers can use fructose in low concentrations as well. This support seems to be lactate independent (Rich & Brown 2018). Interestingly, peripheral nerve axons do not depend on lactate shuttling for glucose to support CAP function. Instead, maybe glucose can be taken up by axons directly if needed (Rich & Brown 2018, Véga et al 2003).

2.2.3. Schwann cell metabolism

What happens when the Schwann cell metabolism is changed? In the last 10 years, many studies have been conducted using genetic knockouts to test this question (summarized in (Bouçanova & Chrast 2020, Fledrich et al 2019)). SCs themselves seem to be able to survive on a mainly aerobic glycolytic metabolism as studies interfering with mitochondrial oxidation either by disrupting *mitochondrial transcription factor A (TFAM)* (Viader et al 2011, Viader et al 2013), Cox10 (Fünfschilling et al 2012) or the tumor suppressor LKB1 (Beirowski et al 2014, Pooya et al 2014) showed no influence on their own survival. Axons however, seem to degenerate in these models, with sensory populations being more prone to damage than motoric fibers. LKB1 mutants show no signs of demyelination if the deletion happens in adulthood. If the loss happens earlier, LKB1 and TFAM seem to eventually myelinated normally while COX10 shows more developmental influence. Interestingly, many models showed a

reduction in lipid levels. An increase in lactate was reported as well, which seemed to be a compensatory mechanism, as the removal increased axonal degeneration. Only recently it has been shown, that after nerve crush Schwann cells switch to a more glycolytic phenotype via activating mTORC1 and C-Myc/Hif1α thereby protecting axons after injury presumably by providing more lactate (Babetto et al 2020).

2.3. Charcot-Marie-Tooth disease type 1A

2.3.1. Patients and animal models

In the PNS, the most common inherited disorders are motor and sensory neuropathies also termed Charcot-Marie-Tooth (CMT) diseases with a prevalence rate of 10-28/100 000 (Pareyson et al 2017). Patients present with distal limb weakness and sensory loss that has a distal to proximal progression with the feet being affected first leading to food deformities. CMT diseases are classed into demyelinating or CMT1, where the primary genetic defect occurs in Schwann cells, or axonal (CMT2) forms, where most of the defects occur in the axons. The two classes are clearly to be discerned by the motor nerve conduction velocity as in CMT1 is always <38m/s while CMT2 is above that (Rossor et al 2015). CMT1A mostly caused by a duplication of parts of chromosome 17 (17p11.1-12), including the *PMP22* gene (*peripheral myelin protein 22*) (Raeymaekers et al 1991), is accounting for at least 90% of CMT1 (around 40-50% of all CMT cases). CMT1A, a slowly progressive form, mostly diagnosed in the second decade of life and has no influence on life span (Rossor et al 2015). Disease severity shows a high variability between patients, even between monozygotic twins (Garcia et al 1995). Histological hallmarks are demyelination, onion bulb formation (multiple proliferating Schwann cells around amyelinated axon) and secondary axonal loss (Shy et al 2005b). Multiple animal models have been generated over the years. Two models, the “CMT rat” generated by introducing copies of the murine gene (Sereda et al 1996) and the C61 mouse model by introducing human copies (Huxley et al 1998) model the disease pathology well as, in both models similar overexpression in comparison to patients on mRNA level of *Pmp22* (CMT rat ~1.6 fold; C61 ~2 fold; patients ~1.7 fold) leads to gait abnormalities, hind limb weakness, muscle atrophy, dysmyelination and secondary axonal loss whereas the life span is not affected to great extend (Fledrich et al 2012b).

2.3.2. Treatment options

Having animal models that closely resemble the disease in patients allows to conduct preclinical trials, which in best-case scenario can be translated into patients. Multiple treatments aiming at the reduction of PMP22 overexpression have been proposed. Progesterone antagonist have been proven to be successful in preventing axonal loss in CMT rats, while a transfer to patients is not likely due to severe side effects (Meyer zu Horste et al 2007, Sereda et al 2003). In another treatment PXT3003, a combination of low doses of baclofen, naltrexone and sorbitol aimed at reducing PMP22 expression in a synergistic approach, failed to do so but has been proven to be beneficial for disease outcome in the animal model and a phase II clinical trial (Attarian et al 2014, Prukop et al 2019, Prukop et al 2020). Fledrich and colleagues (2014) showed that treating animals early with NRG1 prevents axonal loss well into adulthood. This has been shown to act via normalizing the dysbalance of PI3K-AKT/MEK-ERK signaling. However, this is yet another example of a treatment, which will not be transferred easily to patients due to side effects (Fledrich et al 2014, Rossor et al 2016). Trials to affect neuronal survival directly by genetic approaches in the CMT rats (Wlds mutants (Meyer zu Horste et al 2011)) and a small patient studies (8 patients) using neurotrophin (NT) 3 had positive effects on axonal numbers and disease outcome. Further, efforts to use ascorbic acid as antioxidant in animal models improved the phenotypic and histological outcome. However, transferring this to clinical trials failed as the outcome measures itself failed to detect changes (Fledrich et al 2012b, Rossor et al 2016). In an approach of lipid, supplementation in an animal model rescued the observed reduction of myelinated fibers (Fledrich et al 2018). As of now, most therapies are aimed at reducing symptoms. Due to the fact, that CMT1A is caused by an overexpression of PMP22 recent efforts have went into the direction of gene therapy trying to reduce protein expression by targeting the gene itself (Gautier et al 2020, Lee et al 2019).

2.3.3. Biomarkers as clinical outcome measures

Seeing that CMT1A is a slowly progressive disease, it is difficult to conduct positive clinical trials. The need for sensitive outcome measures to be able to detect small changes over short periods in relatively small groups is high. To this end many studies have been conducted in recent years (reviewed in (Pareyson et al 2017, Rossor et al 2020)) and are summarized in **Table 1**. Many clinical or functional outcome measures

have failed to detect small changes for treatment effects in conducted studies (as mentioned for ascorbic acid). Thus, many efforts have been made to identify surrogate disease markers (e.g. MRI, plasma levels of proteins, mRNA transcripts in skin) to be used in clinical studies as endpoints.

Table 1: Summary of outcome measures for disease severity in CMT1A patients.

Outcome measure	Reference	Included measures	Comments
Clinical outcome measures			
ONLS	(Graham & Hughes 2006)	Upper and lower limb function	-Insensitive in ascorbic acid trials -Approved outcome measure of FDA
CMTNS	(Shy et al 2005a)	Symptoms, clinical examination, tasks, neurophysiology	-Proven unsuitable in ascorbic acid trials
CMTNSv2	(Murphy et al 2011)	Modified from Version 1	-Unsuitable for mild to moderate patients
Rasch modified version of CMTNSv2	(Wang et al 2017)		-Significant progression over two years
Functional Outcome measures			
CMTPedS	(Burns et al 2012)	Strength, dexterity, sensation, gait, balance, power, endurance	-Specific for children -Sensitivity has been demonstrated in NHS (Cornett et al 2017)
CMT-FOM	(Eichinger et al 2018)	Hand grip, ankle-foot dorsiflexion/ plantar-flexion strength, nine-hole peg, balance beam, timed walk, stair climb	
Patient reported			
CMT health index	(Johnson et al 2018)	Questionnaire assessing Quality of life	
Biomarker			
Muscle MRI fat fraction	(Morrow et al 2018, Morrow et al 2016)	MRI skeletal muscle calf level	-Reproducible over different sites
Plasma NfL	(Sandelius et al 2018)	As a marker for axonal damage	-Holds true in some animal models as well
TMPRSS5	(Wang et al 2020)	Protein Plasma levels	-Seems to distinguish CMT1A patients from controls and other subtypes
Cluster of five transcripts	(Fledrich et al 2017, Fledrich et al 2012a)	mRNA transcripts (*CDA, CTSA, ENPP1, GSTT2, PPARG*) in skin	-Holds true in animal model
IENFD	(Hartmannsberger et al 2020)	Glabrous skin from finger	

Table 1 continued

Outcome measure	Reference	Included measures	Comments
PMP22	(Svaren et al 2019)	Transcript levels in skin (normalized to SC marker)	Suitable for gene targeting therapies

Adapted from Rossor et al 2020. ONLS: Overall neuropathy limitation score; CMTNS: CMT neuropathy score; CMTPedS: CMT pediatric scale; CMT-FOM: CMT Functional outcome measure; NfL: neurofilament light chain; TMPRSS5: transmembrane protease serine 5; CDA: Cytidine deaminase; CTSA: Cathepsin A; ENPP1: Ectonucleotide pyrophosphatase/phosphodiesterase 1; GSTT2: glutathione S-transferase theta 2; PPARG: Peroxisome proliferator-activated receptor gamma; IENFD: intra epidermal nerve fiber density

2.4. Aim of the study

In CMT1A, patients present with a severely reduced NCV right from the beginning, while the CMAP declines with time leading to axonal loss. This points towards two steps in the pathology. First, the dysmyelination and shorter internodes followed by a secondary axonal degeneration and denervation. Axonal loss correlates strongly with disease severity highlighting the importance to unravel the mechanisms that drive axonal loss after demyelination. It has been proposed, that myelination and axonal metabolic support can be uncoupled events making it even more relevant (Nave 2010). Unmyelinated axons could survive well under functioning metabolic support of glial cells. However, Ravera and colleagues presented evidences for changes in Schwann cell compartmental oxidative phosphorylation and an increased mitochondrial number in demyelinated axons (Ravera et al 2013), a phenomenon that has been reported in patients as well (Saporta et al 2009, Soldevilla et al 2017), implicating short comings in energy supply of axons. Involvement of metabolic alterations in CMT1A have been reported in a gene ontology based study (Fledrich et al 2012a). Recently, the involvement of lipid metabolism was described on transcriptional level and its merit as substitution therapy shown in the animal model (Fledrich et al 2018). We want to unravel the alterations in metabolic pathways in *Pmp22* overexpressing Schwann cells and how these consequently influence in the complex relationship of axo-glial coupling and by this drives disease pathogenesis in a process possibly independent from myelination. Insight into the interplay fueling axonal function could provide options to develop novel therapeutic targets.

In patients, CMT1A presents with a high disease variability, which is poorly understood. Clinical symptoms progress slowly over time. Sensitive markers to predict disease progression in the long term would add benefits to patient counseling. Therapy plans could be adapted accordingly and knowing what is to come could adapt psychological care of patients. Additionally, to be able to establish new translational therapy options, successful clinical trials and high correlation of animal model to patients is necessary. This powers the need of highly sensitive, easily accessible surrogate markers for disease progression. Blood transcript levels are promising candidates, seeing that this is feasible and repetitively to be integrated in standard outpatient care. The sampling is easy accessible by minimally invasive procedure and the first steps of processing can easily be done in the field. A translational approach was planned to identify marker in a cohort of *Pmp22*^{tg} rats and to translate the findings to patients in a longitudinal cohort. In the second part of this study, it was therefore the aim to identify new surrogate markers for CMT1A disease progression, able to decipher marginal changes, in blood samples of a patient cohort from Germany.

3. The glial axonal support in CMT1A peripheral nerves

3.1. Results

3.1.1. Sciatic nerves of *Pmp22*^{tg} rats show an altered metabolite profile

In CMT1A patients and animals have been reported to present with a detrimental axonal loss over time. Additionally, disease severity correlates to reduction in axonal number and the consequently following decline of CMAP and muscle strength. This cannot only be explained by the dysmyelination phenotype of the disease, which is reported early on in disease. It has been shown in peripheral nerves of animals harbouring additonal copies of the *Pmp22* gene (*Pmp22*^{tg}) as well as in skin biopsies of patients with CMT1A, that mitochondrial density in axons of CMT1A increases in myelinated fibers (Ravera et al 2013, Saporta et al 2009). Additionally, it has been suggested that a loss of mitochondrial enzymatic machinery preceedes the loss of fibers in skin biopsies of patients (Soldevilla et al 2017). These studies suggesting a failure of metabolic support by SCs. Fledrich and colleagues (2012) have mentioned the involvement of dysregulated metabolic processes in *Pmp22*^{tg} animals in a gene onthology annotation based RNA profiling (Fledrich et al 2012a). A RNAseq study over time showed a dysregulation in lipid metabolism in CMT1A animals (Fledrich et al 2018).

Therefore, the here presented study aimed at identifying changes in metabolic support of axons by Schwann cells overexpressing *Pmp22*. Sciatic nerves of *Pmp22*^{tg} rats at postnatal day (P)18 and at 9 weeks (W) were isolated and the epineurium removed, to enrich SCs. In the obtained nerve lysates, metabolites were measured in an MS-based approach (Lisa Schlicker, Yannic Nonnemacher, Karsten Hiller (TU Braunschweig)). 102 metabolites were measured and the amount of each metabolite compared to the age matched control group. The differences are shown as log2 fold changes in relation to the p-value. At P18, 10% of measured metabolites are enriched, while almost 4% are reduced in CMT1A nerve lysates (**Figure 4 A**). This pattern intensified over time. At 9W a quarter of all measured compounds was detected to be enriched in comparison to the control group and 15% were detected in a reduced amount (**Figure 4 B**). When comparing fold changes of P18 versus 9W for each experimental group equal patterns were detected therefore neglecting a developmental switch (data not shown). All identified compounds significantly altered for one of the time points are shown in a heat map for both time points (**Figure 4 C**). Exact values of all

measurements depicted (Mean±SD, p-values) are shown in **Table S 1** of the supplement. In the following, some of the most intriguing findings are being highlighted.

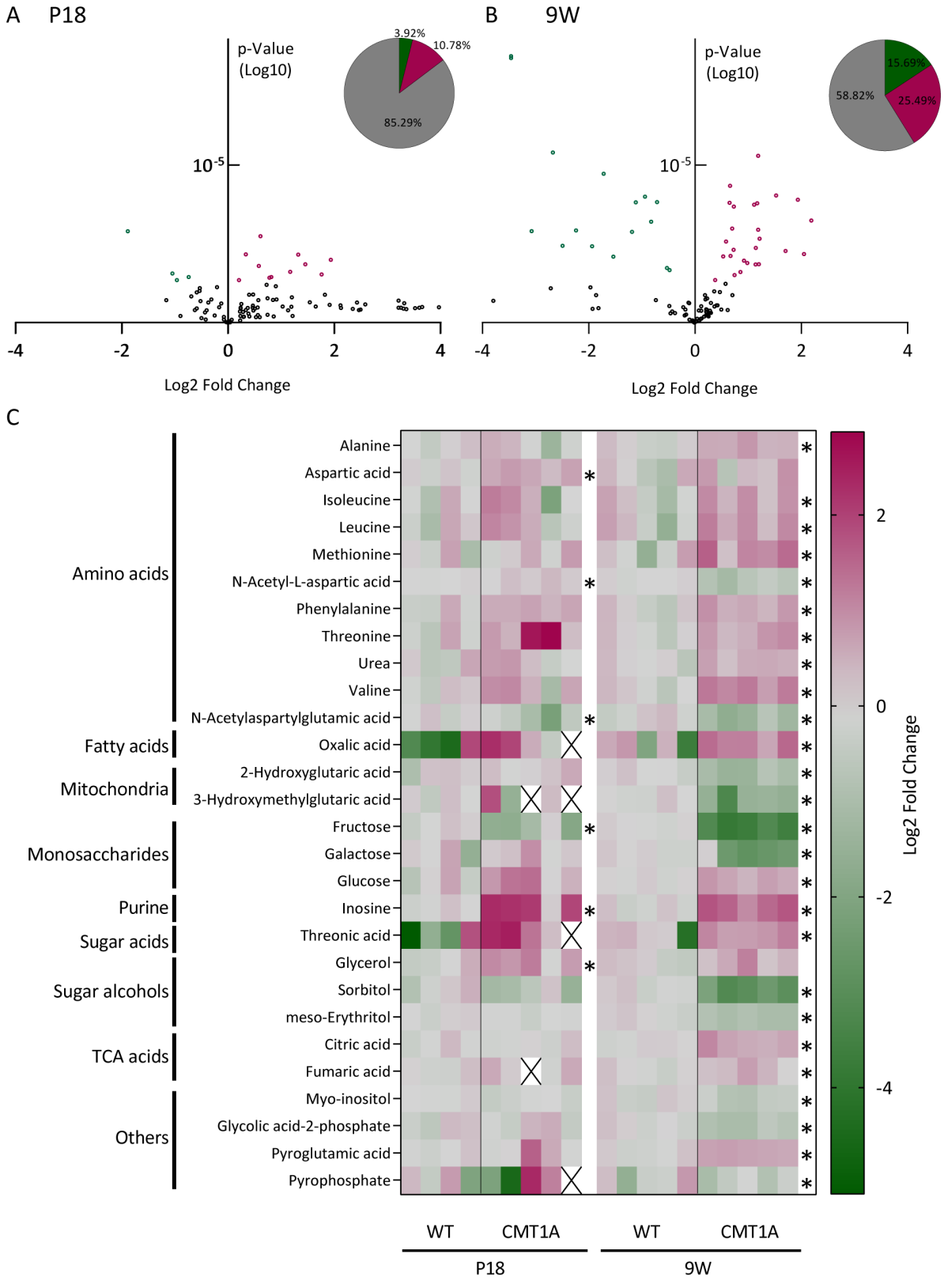

Figure 4: Alterations in metabolite profile in *Pmp22*^{tg} rats. An MS-based analysis of metabolites in sciatic nerve lysates of P18 (A) and 9W (B) *Pmp22*^{tg} rats revealed significant differences in metabolite abundance compared to age matched controls. (C) Compounds with

3.1.2. While glucose is enriched, peripheral nerves of *Pmp22^{tg}* animals show reduced activity of the polyol pathway and do not increase their glycogen storages

Two of the most prominent changes were the 10-fold reductions of sorbitol and fructose at 9W. These are metabolites processed in the polyol pathway, a pathway known to be upregulated to process up to 30% of glucose under hyperglycemic conditions (González et al 1984), while normally 3% of all glucose goes toward the pathway (Morrison et al 1970), first described in 1956 (Hers 1956, Yabe-Nishimura 1998). Glucose is reduced to sorbitol by aldose reductase depending on NADPH. In a second step, sorbitol dehydrogenase (depending on NAD+) metabolizes sorbitol further to fructose. In numerous studies this pathway has been implicated to play an important role in the pathophysiology of diabetes (Sango et al 2014). In **Figure 5A** the alterations in polyol pathway observed in this study are shown. Despite an observed increase in glucose, sorbitol and fructose were highly depleted in nerve lysates of *Pmp22^{tg}* animals. In quantitative real time polymerase chain reaction (qRT-PCR) analysis of tibial nerves at 9W a decreased expression of *Akr1b1* (aldose reductase) could be detected. As shown in **Figure 5D**, expression of *Akr1b1* in sciatic nerves was upregulated in wild type (WT) animals between P6 and P18. This upregulation was almost completely abolished in *Pmp22^{tg}* animals, an effect that did not normalize until 16W.

Glucose is taken up into peripheral nerves from circulating blood glucose pools. Next, the blood glucose level in the periphery of CMT1A rats were analyzed. At 30W the levels of circulating glucose were unchanged in comparison to age matched controls (WT: 86mg/dL ± 11.8; CMT1A: 91mg/dL ± 10.2; p=0.5) (**Figure 5B**). Metabolites reach the cells in peripheral nerves in small vessels interspersed among the axons. The amount of these vessels was quantified in semi thin cross sections of sciatic nerves of CMT1A animals at 26W which remained unchanged in numbers (WT: 47.3 vessels ± 10; CMT1A: 51 vessels ± 2.2; p=0.7) (**Figure 5C**).

Figure 4 continued:
significant changes are shown. Values are depicted as log2 fold change to the age matched control group. Significance is shown to the right of the CMT1A row for each age group. Samples without data are marked with X. Metabolome analysis performed by Lisa Schlicker, Yannic Nonnenmacher and Karsten Hiller (TU Braunschweig). Table with all exact values in supplement (Table S 1) (n=4-5; Students T-Test p-value ≤0.05*)

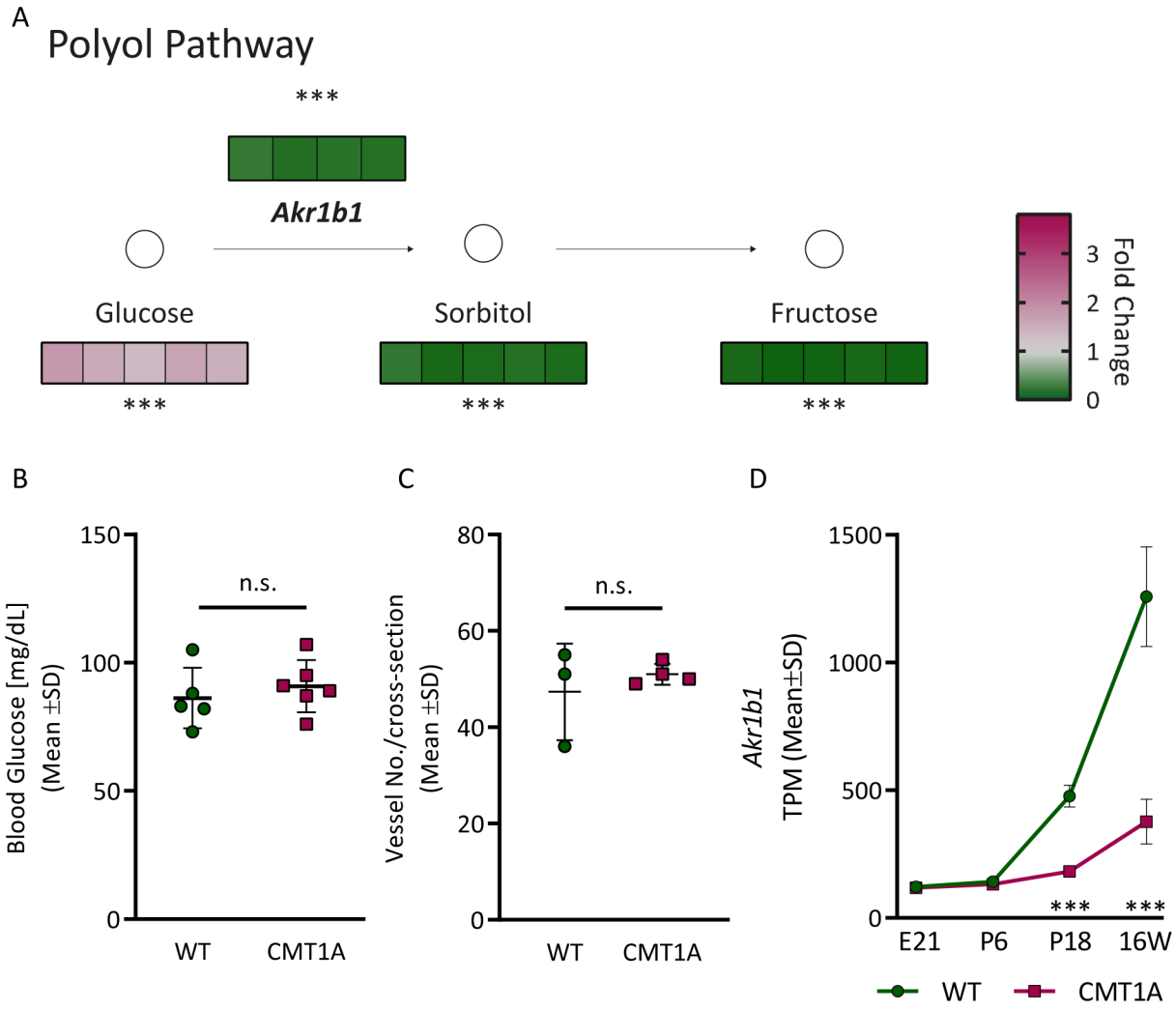

Figure 5: Glucose is enriched in peripheral nerves of *Pmp22*^{tg} rats, with no evidence for "diabetic" Schwann cells. Polyol Pathway corresponding metabolites and mRNA of enzymes are reduced in CMT1A animals (A). Metabolites: 9W metabolome data depicted as fold change to control group. Enzyme mRNA of 9W tibial nerve lysates analyzed by qRT-PCR. Key enzyme is marked in bold. A table with all values is provided in the supplement (**Table S 2**). Blood glucose measurements are unaltered (B) and the number of vessels per nerve cross section is not influenced (C). Blood glucose: 30W animals and age matched controls. Vessel analysis: 26W and age matched controls on semi-thin cross sections of sciatic nerve. (D) Reanalysis of RNAseq data from (Fledrich et al 2018) performed by Ting Sun. Sciatic nerve analysis from WT versus *Pmp22*^{tg} rats at E21, P6, P18 and 16W. Depicted are TPM for *Akr1b1*. (Mean ± SD; Students T-Test, p-value ≤0.001***)

In Schwann cells, glucose can be stored as glycogen (Brown et al 2012). This lead to the question whether the increase in glucose is mirrored in an increase in storage glycogen. By a colorimetric plate assay glycogen content in sciatic nerves of *Pmp22*^{tg} mice at 12W was measured in pooled samples of 3 animals (**Figure 6B**). Glycogen amounts were normalized to protein content of the sample. *Pmp22*^{tg} animals showed a non-significant trend towards 60% of WT levels (WT: 0.005 µg/µg protein ± 0.001; CMT1A: 0.003µg/µg protein ± 0, 0019; p=0.12) (**Figure 6C**). As shown in **Figure 6A**,

key levels of enzymes of glycogen metabolism were maintained in *Pmp22*^{tg} rats. Both findings do not point towards an increase in glycogen storages, but rather show a trend of reduced storage activity.

In conclusion, glucose was enriched in nerve lysates of *Pmp22*^{tg} rats, while the polyol pathway was significantly down regulated. Despite higher glucose concentrations, glycogen storages remained unaltered.

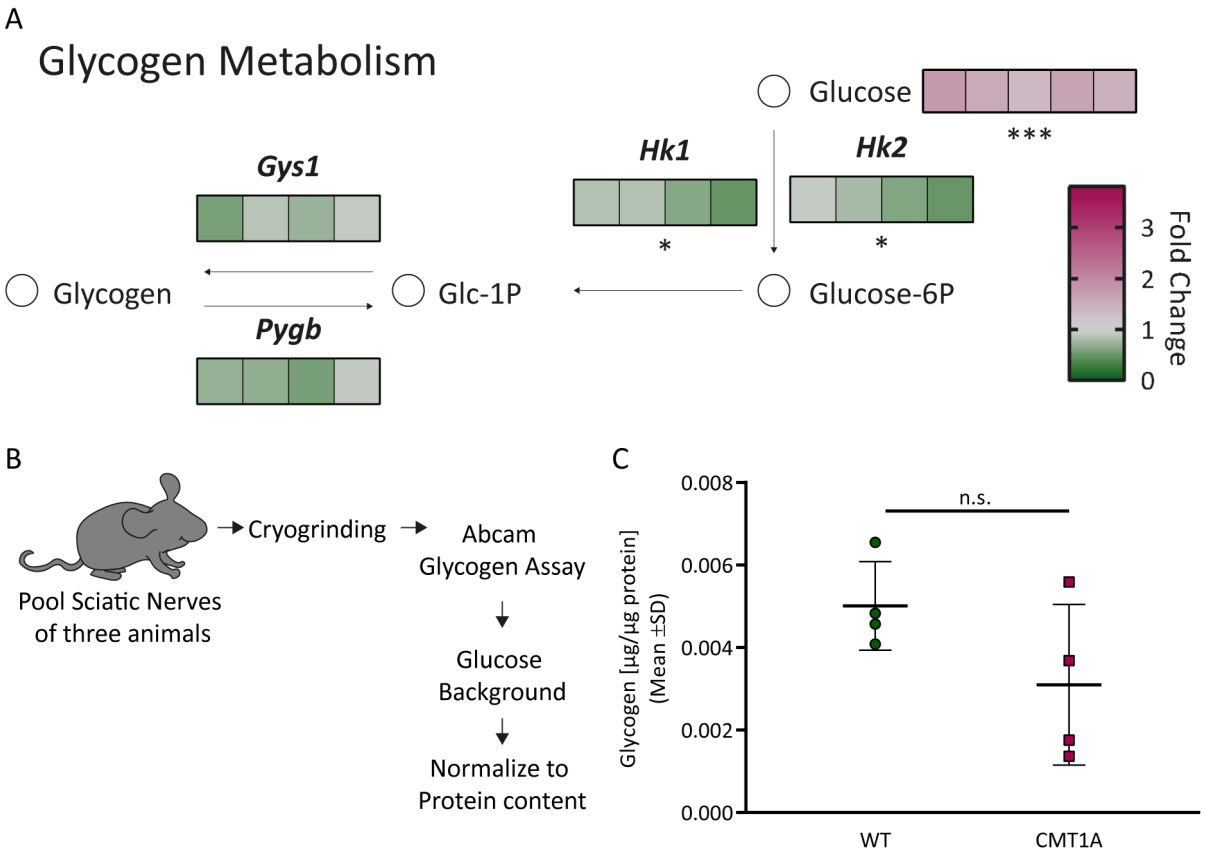

Figure 6: Trend towards a decrease in glycogen storages in Schwann cells in *Pmp22*^{tg} mice. Key enzyme mRNA levels of glycogen metabolism show a trend towards decreased expression in *Pmp22*^{tg} animals (A). (Enzyme mRNA 9W tibial nerve lysates analyzed by qRT-PCR. Key enzymes are marked in bold. A table with all values is provided in the supplement (**Table S 2**)) Glycogen content of sciatic nerve lysates of *Pmp22*^{tg} mice at 12W (B,C) shows a trend of depletion despite enriched glucose levels. (Mean ± SD Students, T-Test, p-value ≤0.001***)

3.1.3. Expression of glycolytic genes is decreased while free glucose is enriched

Glucose can be partially metabolized to pyruvate by glycolysis. This process results in two ATP molecules from ADP and reduces two NAD^+ to NADH (Dienel 2019, Yellen 2018). To test, whether the increase in free glucose is accompanied by an upregulation of glycolysis itself mRNA expression patterns were analyzed. In the conducted metabolome analysis, the glycolysis products pyruvate and in a next step lactate, as

well as the intermediate glyceraldehyde 3-P were measured in CMT1A sciatic nerve lysates at 9W in comparable amounts to WT (**Figure 7**).

Regulatory enzymes of glycolysis are Hexokinase (phosphorylating glucose after import into the cell cytoplasm), Phosphofructokinase, (the first pathway committed step) and pyruvate kinase (the last step of the glycolysis) (Dienel 2019, Yellen 2018). All of these enzymes were significantly down regulated on mRNA level in tibial nerves of *Pmp22*^{tg} animals. Additionally, enzymes metabolizing intermediate steps of the pathway were down regulated as well.

Glucose is assumed to be transported by GLUT1 (*Slc2a1*) and GLUT3 (*Slc2a3*) in peripheral nerves (Jha & Morrison 2018). Both, *Slc2a1* and *Slc2a3*, expression are reduced in a qRT-PCR analysis at 9W. The lactate transporters MCT1 (*Slc16a1*) and MCT2 (*Slc16a7*), which show unchanged mRNA levels in CMT1A compared to WT controls.

In summary, enzymes involved in glycolysis were down regulated on mRNA levels and glycolysis end products were unchanged in CMT1A nerve lysates.

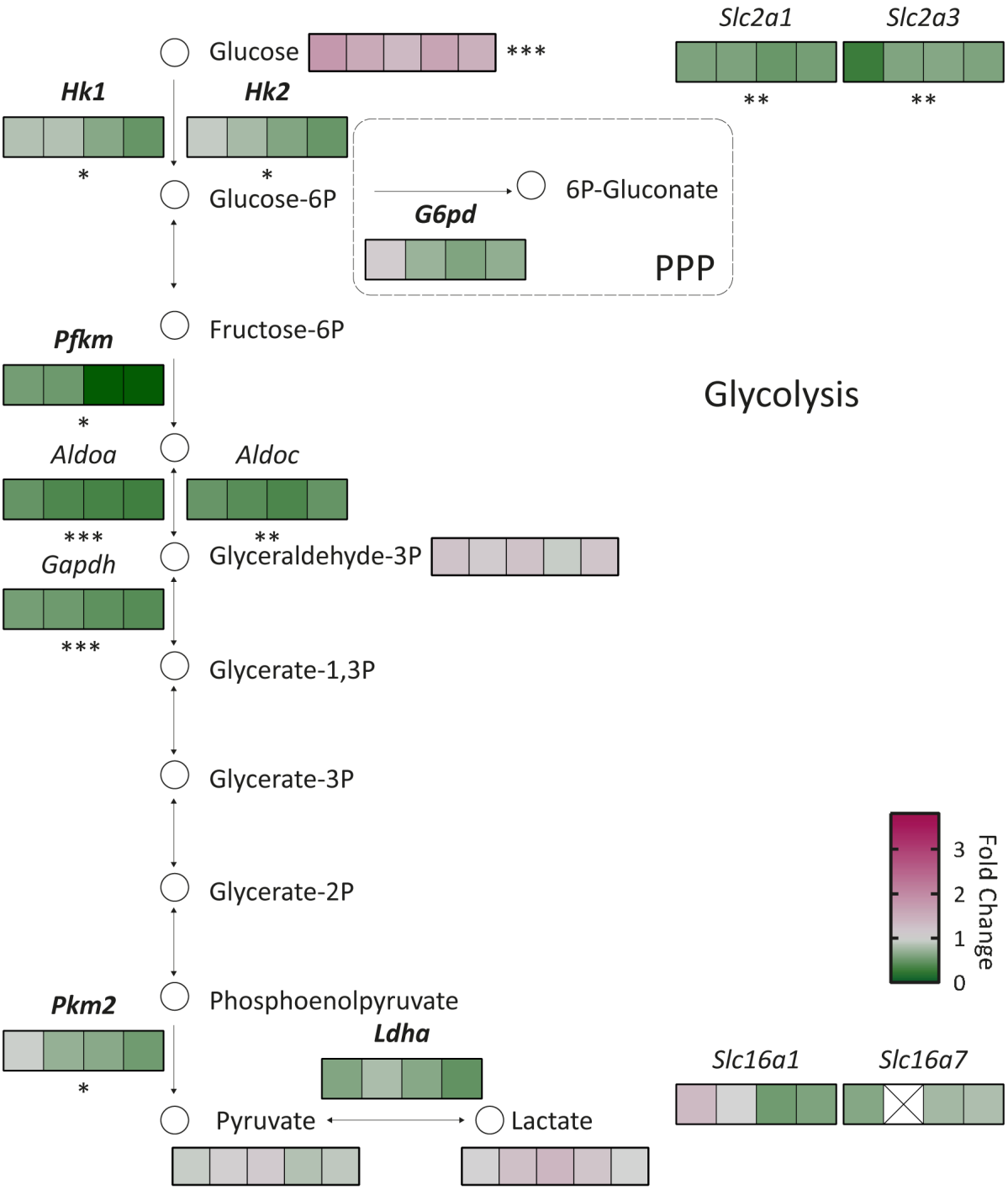

Figure 7: Expression of glycolytic enzymes is downregulated despite enrichment of glucose. Expression of all key enzymes of glycolysis is down regulated significantly in CMT1A, as well as several intermediate steps. While there is a significant increase of glucose, other metabolites are not enriched. (Metabolites: 9W metabolome data depicted as fold change to control group. Enzyme mRNA 9W tibial nerve lysates analyzed by qRT-PCR. Key enzymes are marked in bold.) Exact values are provided in **Table S 2**. (Mean ± SD Students T-Test, p-value ≤0.05 *, ≤0.01**, ≤0.001***)

3.1.4. GLUT1, MCT1 and HK1 are enriched in sciatic nerves of *Pmp22^{tg}* rats.

With the enriched glucose levels and a decrease of glycolysis enzymes on mRNA levels, the question was, whether the free glucose could be transported between cells. Glucose transporters in the PNS are reported to be GLUT1 in the glial compartment whereas GLUT3 is assumed to be the transporter localized to the axonal compartment. Closer analyses were conducted towards the transporters.

In a first step the protein expression of GLUT1 at 9W in sciatic nerve lysates of *Pmp22^{tg}* and control rats was analyzed (**Figure 8A** and **B**). GLUT1 was significantly increased 6.33± 2.35-fold in comparison to controls (WT: 1± 0.76; CMT1A: 6.33± 2.35; p=0.005). Subsequently, the localization of the transporter was studied. Thus, stainings on sciatic nerve teased fiber preparation were performed labeling for GLUT1 (left panel) and MAG (middle panel) as a marker for non-compact myelin (**Figure 8C**). In the overlay (right panel) one can appreciate the localization of GLUT1 to the SLI clearly labelled with MAG. Additionally, GLUT1 was localized at the abaxonal SC membrane and along the axon. However, in these specimens one was not able to differentiate clearly between adaxonal SC membrane and axonal membrane itself. In the fibers of *Pmp22^{tg}* animals GLUT1 staining showed the same pattern of localization than the wild type controls (lower panels). To verify these findings by an additional experimental approach, Immunoelectron microscopy was used to label GLUT1 with gold particles in cross sections of tibial nerves of 44W old CMT1A animals in comparison to control animals (**Figure 8D**). Observation of a localization of GLUT1 to SLIs, abaxonal membranes and localization at the interface of SC and axon in WT as well as in CMT1A were confirmed. In conclusion, protein levels of GLUT1 were elevated and it appears the transporter maintained localization under pathology.

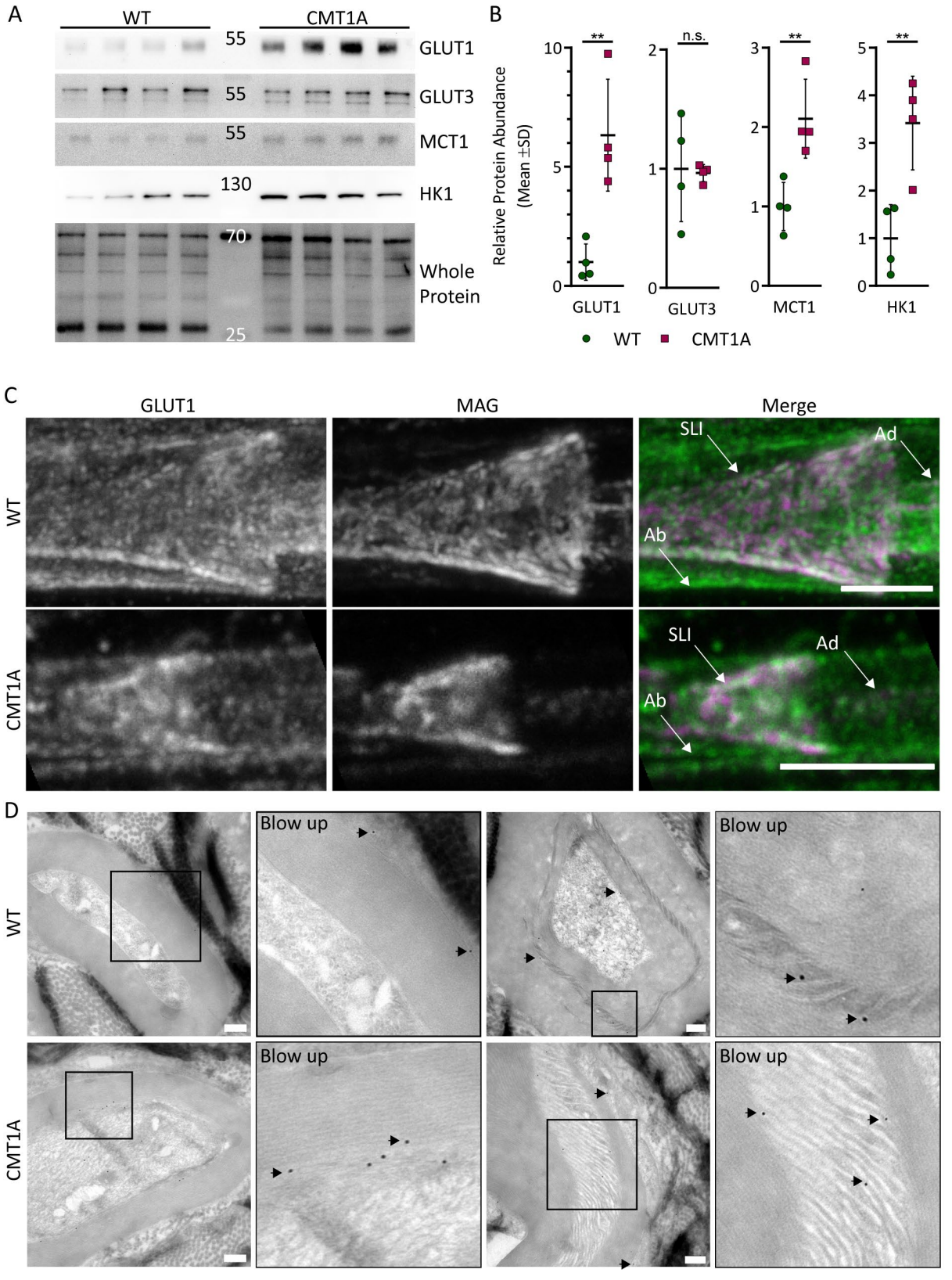

Figure 8: GLUT1 is increased in peripheral nerves of *Pmp22*^{tg} rats but correctly localized to non-compact regions of myelin. Western Blot analysis of transporters GLUT1, GLUT3 and MCT1 and the enzyme HK1 (A) in 9W sciatic nerve lysates and quantification normalized to total protein load (B) show an increase for GLUT1, MCT1 and HK1. Immunofluorescent staining of 9W sciatic nerve teased fibers with GLUT1 and MAG, as a marker for non-compact myelin. SLI, abaxonal (Ab) and adaxonal (Ad) membrane are marked with a white arrow (C)

The presumed axonal glucose transporter GLUT3 on the other hand remained unchanged on protein level (WT: 1± 0.44; CMT1A: 0.96± 0.07; p=0.88), MCT1 was significantly increased two-fold in comparison to the control group (WT: 1± 0.3; CMT1A: 2.11± 0.5; p=0.009) (**Figure 8A** and **B**).

Hexokinases are the first enzymes to metabolize glucose upon transport into the cytoplasm. Glucose is phosphorylated into glucose-6P which prevents the export via glucose transporters (Dienel 2019). In sciatic nerve lysates of *Pmp22^{tg}* animals at 9W, HK1 was upregulated three-fold in comparison to controls (WT: 1± 0.7; CMT1A: 3.42± 0.98; p=0.007). This could, together with the increase of GLUT1, facilitate an increased glucose transport. Where is the glucose transported to? Accordingly, a staining for HK1 in cross sections of femoral nerves at 18W was done using TUJ1 as an axonal marker. Hexokinase1 was localized to cytoplasmic pockets of Schwann cells and to axons in WT controls (**Figure 9** upper row). When comparing this to *Pmp22^{tg}* animals, there was no Hexokinase positive labeling in organized SC pockets observed but rather an increase in punctate like stainings localized to the axons (**Figure 9** lower row). In conclusion, while the axonal transporter for glucose was unchanged in CMT1A fibers, an increase of HK1 and a localization in axons could be shown.

Does the localization of HK1 to the axon actually indicate that more glucose is transported to the axon in CMT1A? In an attempt to show glucose transport in fibers, acutely teased fibers of sciatic nerves were used and fluorescently labelled glucose (2-NBDG) was added to trace transported glucose *ex vivo*. 2-NBDG is transported via GLUTs as well and can be phosphorylated by hexokinases (Yellen 2018). Unfortunately, in this live imaging set up, only an increase of intensity along compact myelin structures in the fiber preparations was detected (**Figure 10A**) rendering this approach not useful for this study.

Figure 8 continued:
(scale bar 5µm) (STED imaging done with Joris van Dort). Findings were verified in Immuno-EM labeling of GLUT1 in tibial nerve cross-sections of 44W animals. Gold dots are marked with black arrowheads (scale bar 250µm) (D). Blow ups are indicated with black boxes and displayed to the right of the respective image. (Students T-Test, p-value ≤0.01**)

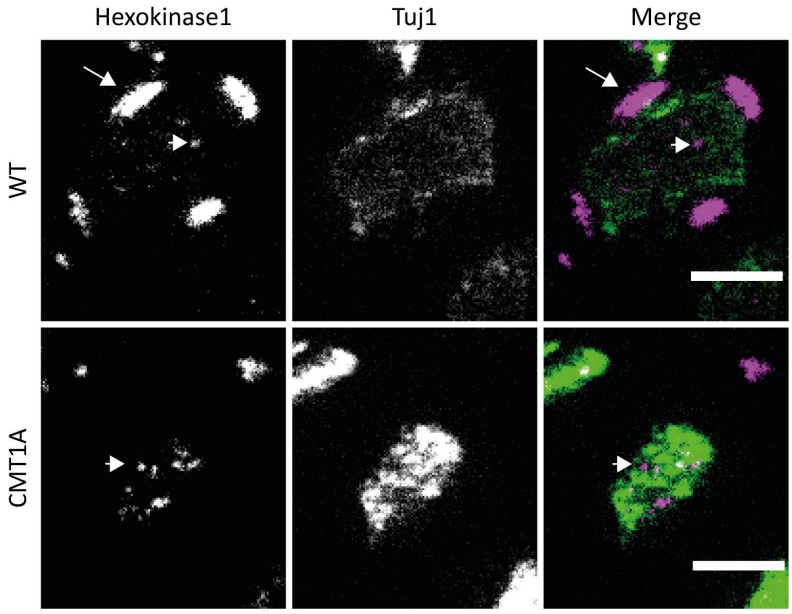

Figure 9: Hexokinase 1 localizes to the axon and cytoplasmic pockets in Schwann cells. Staining of Hexokinase 1 (left panels) and tubulin1 as axonal marker (middle panels). Right panels are Hexokinase1 (magenta) and TUJ1 (green) as overlay. Upper panels WT and in comparison to CMT1A (lower panels). Arrow marks cytoplasmic pockets of Schwann cells and arrowheads mark punctate staining localized to the axon. (staining by Katrin Haase during a master's project (supervision credits). Femoral nerves 18W (Scale Bar 5µm)

Another approach to localize free metabolites, e.g. glucose or lactate, to different cellular compartments is the usage of Förster or fluorescence resonance energy transfer (FRET) sensors. These sensors emit fluorescence at one wavelength when the donor fluorophore is excited and at another when the so-called acceptor fluorophore is close enough to the donor, that upon excitation energy is transferred from the donor to the acceptor and the acceptor emits fluorescence (of another wavelength). Upon binding to the substrate, the sensor undergoes a structural change, altering the distance between donor and acceptor, changing the wavelength of the emitted fluorescent signal. This permits us to measure the intensity at the different wavelength and to conclude from the ratio of the two, whether more bound or unbound sensor molecules are in an analyzed sample (Bajar et al 2016). FRET sensors for different metabolites have been engineered in the past and they can be expressed as transgenes in different cell types of mice.

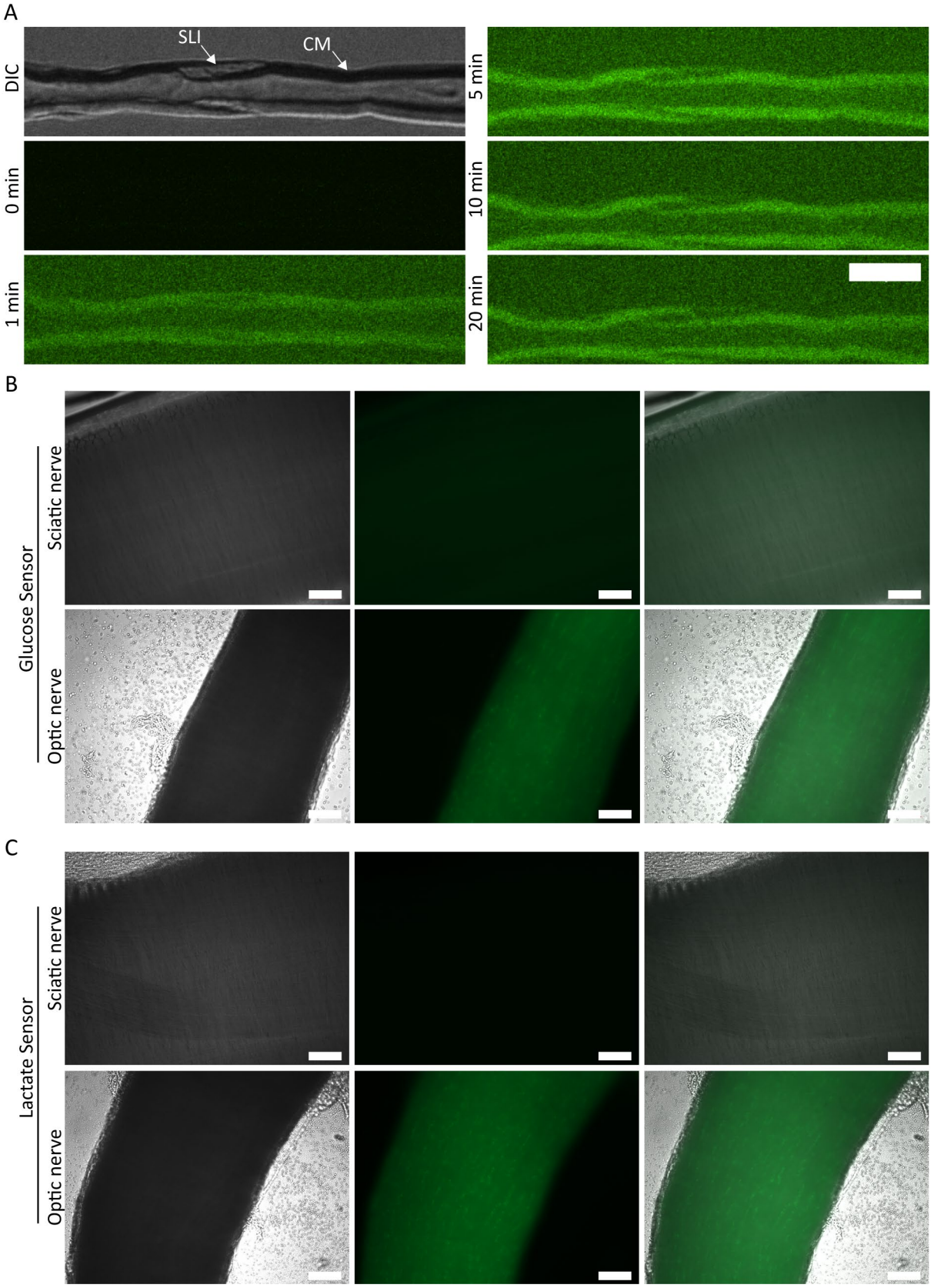

Figure 10: Localizing free glucose in peripheral nerves. In acute teased fiber preparation 2-NBDG addition led to a fluorescence labeling of compact myelin over time (A) (Scale bar 10µm). The structure in DIC image on the upper left is compact myelin (CM) and one can identify SLIs (both marked with arrows). After the image at 0 min the 2-NBDG was added to the medium and a time lapse was recorded (following panels). Expression of endogenously expressed glucose (B) and lactate (C) sensor under the Cnp promoter in sciatic (depicted in

The intensity of expression of a glucose sensor and a lactate sensor under the control of a *Cnp* promoter in mice was tested (generated at MPI-EM by Andrea Trevisiol and Johannes Hirrlinger). *Cnp* drives expression in oligodendrocytes in the CNS and in Schwann cells in the PNS. The intensity of fluorescence in the optical nerve (CNS) and the sciatic nerve (PNS) was compared. The results are shown in **Figure 10B** for the glucose sensor and **Figure 10C** for the lactate sensor. In comparison to the CNS, the expression of both sensors in the PNS was very dim. The fluorescence intensities did not reach levels to be able to use these transgenic mouse lines to detect lactate or glucose levels in WT or *Pmp22^{tg}* animals respectively.

3.1.5. Altered expression of genes encoding for mitochondrial complexes

Assuming glucose reaches a cell and is metabolized by glycolysis, the question arises whether pyruvate is metabolized in mitochondria afterwards. Under aerobic glycolysis, pyruvate is processed to Acetyl-CoA to enter the tricarboxylic acid (TCA) cycle and to be further used in oxidative phosphorylation and by ATP synthase to obtain 30 ATP molecules (Dienel 2019, Yellen 2018). At 9W in sciatic nerve, metabolites accounting for the TCA cycle were measured in the metabolome depicted in more detail in **Figure 11**.

Citrate, fumarate and oxaloacetate were significantly enriched in nerve lysates of *Pmp22^{tg}* rats while succinate and malate remained at WT levels at this age. In addition, several enzymes taking part in the TCA cycle were analyzed. *Sdha* and *Aco2* were significantly reduced on mRNA expression levels, while *Mdh2* remained unchanged.

The next step of energy producing mechanism in mitochondria is the electron transport chain and oxidative phosphorylation. Next, mRNA expression levels of nuclear and mitochondrial expressed marker for each of the complexes were investigated (**Figure 11**). The nuclear expressed markers for Complex I-III were significantly down regulated in tibial nerves of 9W old CMT1A rats. No significant alteration in the expression of the mitochondrial encoded candidates tested in this study was observed.

Figure 11 continued:
the upper panels) and optic nerve (depicted in the lower panels) in comparison showed very little intensity in the PNS (Scale bar: 100µm).

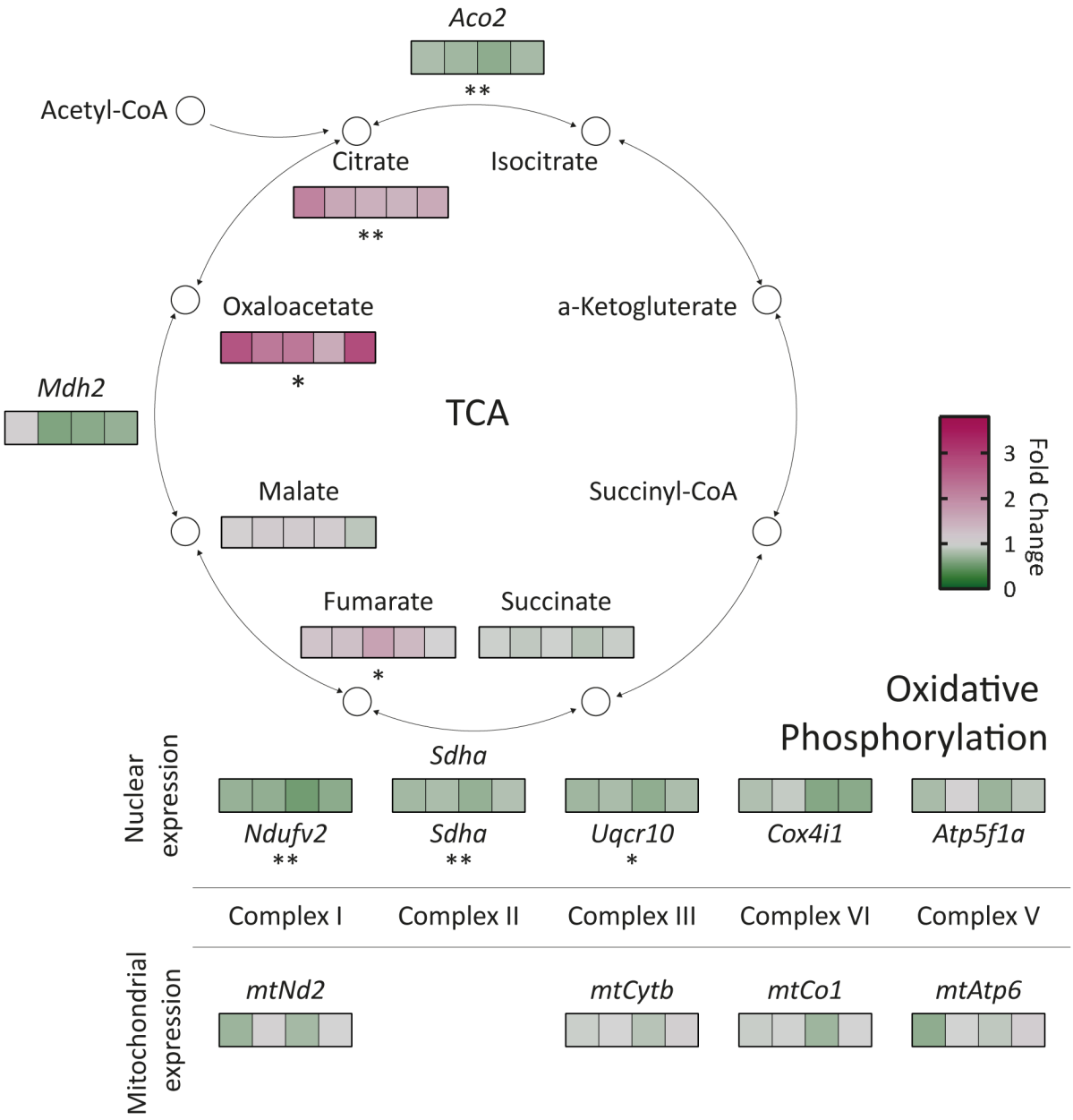

Figure 11: Alterations in metabolites and mRNA expression of TCA cycle and oxidative phosphorylation. Metabolites of TCA cycle are partially enriched in CMT1A while the expression of mRNA of enzymes is decreased. Expression of nuclear markers for OXPHOS are decreased significantly, while mitochondrial expressed markers remain at control levels. (Metabolites: 9W metabolome data depicted as fold change to control group. Enzyme mRNA 9W tibial nerve lysates analyzed by qRT-PCR. (qRT analysis done by Katrin Haase during her Master Thesis (supervision credits)) Exact values are provided in **Table S 2**. (Mean ± SD Students T-Test, p-value ≤0.05 *, ≤0.01**)

A closer look at one mitochondrial expressed marker on protein level revealed a significant increase of MT-CO1 by almost nine-fold in comparison to WT samples in sciatic nerves of *Pmp22*^{tg} rats at 9W (WT: 1± 0.39; CMT1A:8.84± 1.22; p=0.00002) (**Figure 12G** and **I**). To compare this drastic up regulation to existing expression changes in primary Schwann cells *in vitro,* cell cultures of *Pmp22*^{tg} animals were

generated. Cultures were either stimulated to induce expression of myelination markers, e.g. myelin proteins, or in unstimulated conditions, SCs did not show a comparable up regulation of protein levels as shown in **Figure 12 H** and **J** (unstim: WT: 1±0.12; CMT1A:0.84±0.18; p=0.18; Stim: WT: 1±0.13; CMT1A: 0.85±0.13; p=0.16). It can be concluded, that the observed effect is not intrinsic to the Schwann cell, but rather arises from the interaction with axons or is dominated by effects in the axons itself.

As a next step, the morphology of axonal mitochondria was analyzed to test for obvious alterations in morphology or numbers. An increase in mitochondrial numbers in CMT1A has been reported by Ravera and Colleagues (Ravera et al 2013). First electron micrographs of femoral nerves at 16W were used to measure cross sectional area of the mitochondria (**Figure 12A**). One can appreciate in **Figure 12** the changed distribution in the area of mitochondria displayed as violin plot (**Figure 12C**) and as relative frequency distribution (**Figure 12D**). CMT1A nerves showed a trend towards increased mitochondrial area in cross sections. Another parameter measured was the number of mitochondria in one axonal cross section. In rats overexpressing *Pmp22* more axons contained 10 or more mitochondria at once in comparison to the WT control group **(Figure 12E**). Noteworthy, this analysis only displayed a cross sectional area of the organelles. One cannot conclude whether the mitochondria are elongated or rather round and cannot decipher the true volume. Therefore, animals expressing *Thy1* promoter driven roGFP2 targeted to the mitochondrial matrix were used as mitochondrial reporter in axons in the PNS and cross bred to *Pmp22*^{tg} mice. When imaging teased fiber preparations of sciatic nerves at 12W and using Ilastik to analyze the volume of the mitochondria differences became apparent. As one can appreciate in the exemplary images in (**Figure 12B**) that in wild types mitochondria were elongated and oriented along the axons. In *Pmp22*^{tg} animals, the mitochondria appeared smaller and fragmented. The quantification, as graphed in a violin plot in **Figure 12F**, nicely illustrates the altered distribution of the observed volumes.

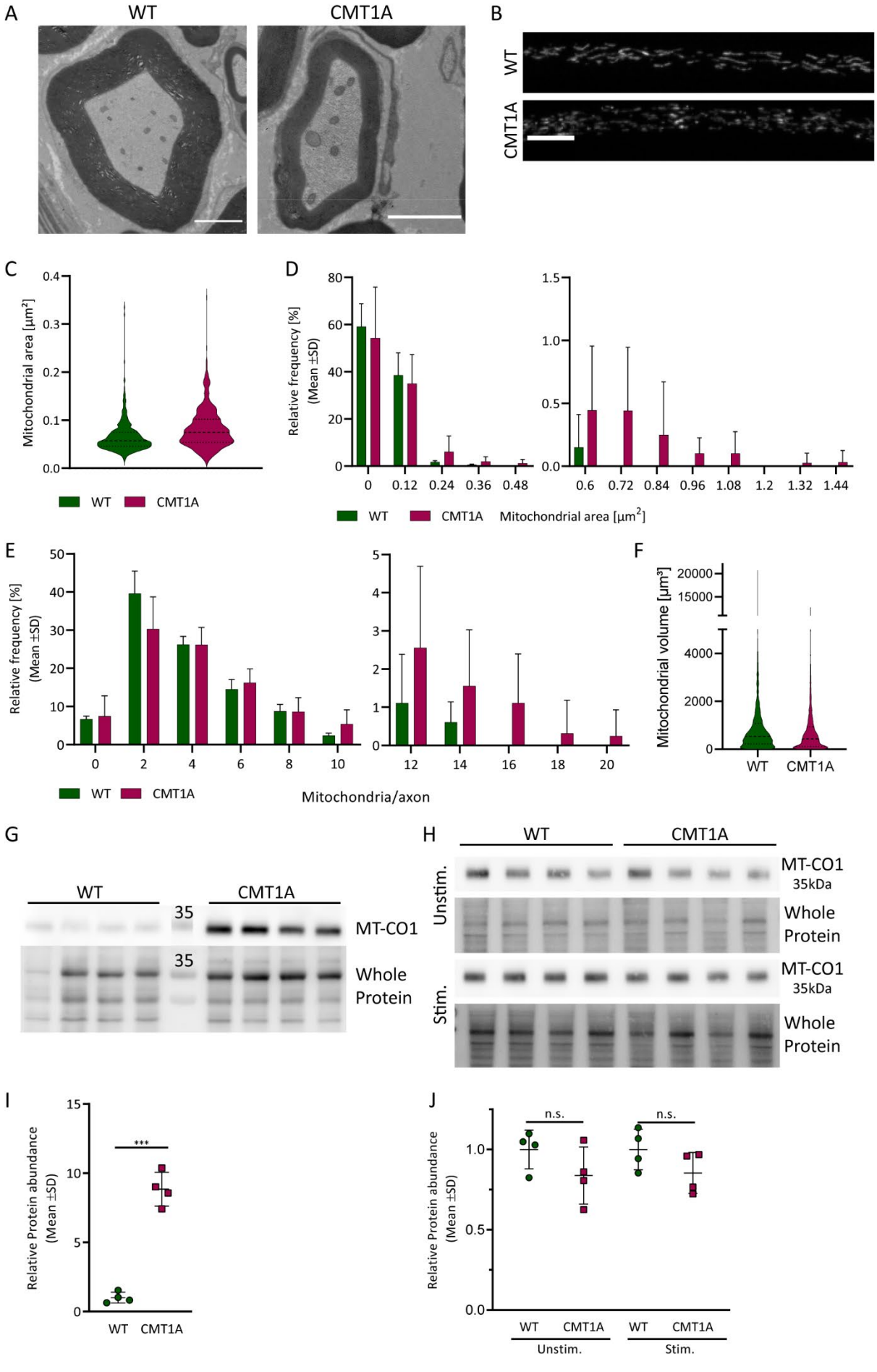
A
WT
CMT1A
B
WT
CMT1A
C
Mitochondrial area [µm²]
WT
CMT1A
D
Relative frequency [%] (Mean ±SD)
Mitochondrial area [µm²]
E
Relative frequency [%] (Mean ±SD)
Mitochondria/axon
F
Mitochondrial volume [µm³]
G
WT
CMT1A
35
MT-CO1
Whole Protein
H
Unstim.
Stim.
MT-CO1 35kDa
Whole Protein
I
Relative Protein abundance (Mean ±SD)
***
J
Relative Protein abundance (Mean ±SD)
n.s.
Unstim.
Stim.

3.1.6. Axonal mitochondria present with reduced ATP levels over time and decreased oxidation ratio in peripheral nerves of *Pmp22^{tg}* mice

More important than the morphological changes observed is the functionality of mitochondria to efficiently produce ATP in axons. The already mentioned sensor animals *Thy1*-mito-*Grx1*-roGFP2 (Breckwoldt et al 2014) cross bred to *Pmp22^{tg}* mice were further used to analyze the sensor state (**Figure 13A** and **B**). RoGFP2 is a GFP changing its fluorescent properties upon oxidation.

In the animal model used, the sensor is fused to glutaredoxin. Thus, the sensor is reporting the redox state of GSH/GSSG. When normalizing the Redox ratio to the reduced ratio a significantly lower oxidized state could be shown in sciatic nerves of CMT1A mice at 12W (WT: 1.21±0.048; CMT1A:1.14±0.028; p=0.035; DTT:1; DA:1.54). The control images for expression are shown in **Figure S 2**.

Figure 12: Analysis of axonal mitochondria suggests abnormalities in *Pmp22^{tg}* rats. Exemplary electron micrographs (A) of axonal mitochondria analyzed on femoral nerve cross sections at 18W of age (scale bar 2µm). (C) and (D) Mitochondrial area on cross-sections seems to be increased for a subset of mitochondria in CMT1A. Analysis of number of mitochondria per axon (E) (WT: 3 animals, CMT1A: 9 animals; scale bar 10µm). (B) Teased fiber preparation of *Thy1*-mito-*Grx1*-roGFP2 animals and volume analysis (F) at 12W in *Pmp22^{tg}* mice (n=5). Western Blot of MT-CO1 (G) and quantification normalized to total protein (I) in 9W sciatic nerve lysates at 9W in comparison to primary Schwann cells (H) and (J) revealed an increase of protein amount only *in vivo*. (Mean ± SD, Students T-Test, p-value ≤0.001***)

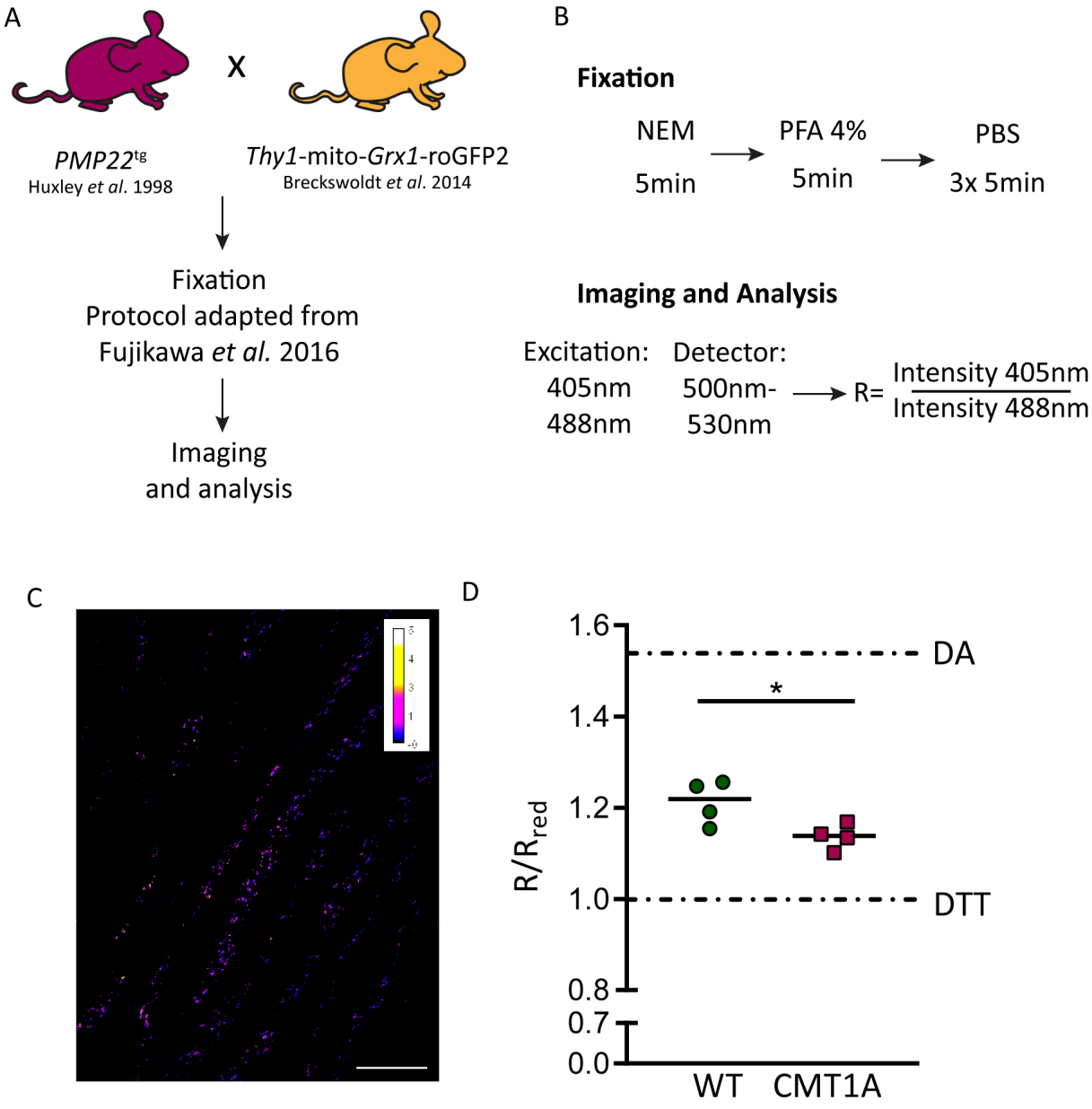

Figure 13: Axonal mitochondria present with reduced oxidation in *Pmp22*^{tg} mice. Analysis of *Pmp22*^{tg} mice cross bred to *Thy1*-mito-*Grx1*-roGFP2 animals (A) and the protocol for analysis of redox state of the sensor normalized to the reduced ratio (Fujikawa et al 2016) (B). An exemplary picture of the ratio (R) shown in LUT Fire (scale bar: 20µm) and the analysis for 12W old sciatic nerves (C). (D) The sensor is less oxidized in CMT1A. DTT as reduced reference and DA as completely oxidized one are shown as dashed line in the graph to indicate dynamic range of the sensor. (Mean ± SD, Students T-Test, p-value ≤0.05 *)

In the end, it comes down to the ATP levels in the axons. A mouse line expressing a ATP FRET sensor, AT1.03^{YEMK}, under the *Thy1* promoter was used (Trevisiol et al 2017) and cross bred to *Pmp22*^{tg} mice (**Figure 14A**). Sciatic nerves were isolated at three time points to analyze ATP levels in axons of CMT1A animals in comparison the control groups shown in **Figure 14B**. At 9W (WT: 0.547±0.032; CMT1A:0.547±0.033; p=0.97) and at 18W (WT: 0.574±0.056; CMT1A:0.587±0.042; p=0.584) there was no

change in ATP levels to be observed compared to control groups. However, at 26W *Pmp22*^{tg} animals show reduced levels of ATP in the axons (WT: 0.548±0.027; CMT1A:0.502±0.035; p=0.029). The control images for expression are shown in **Figure S 1**.

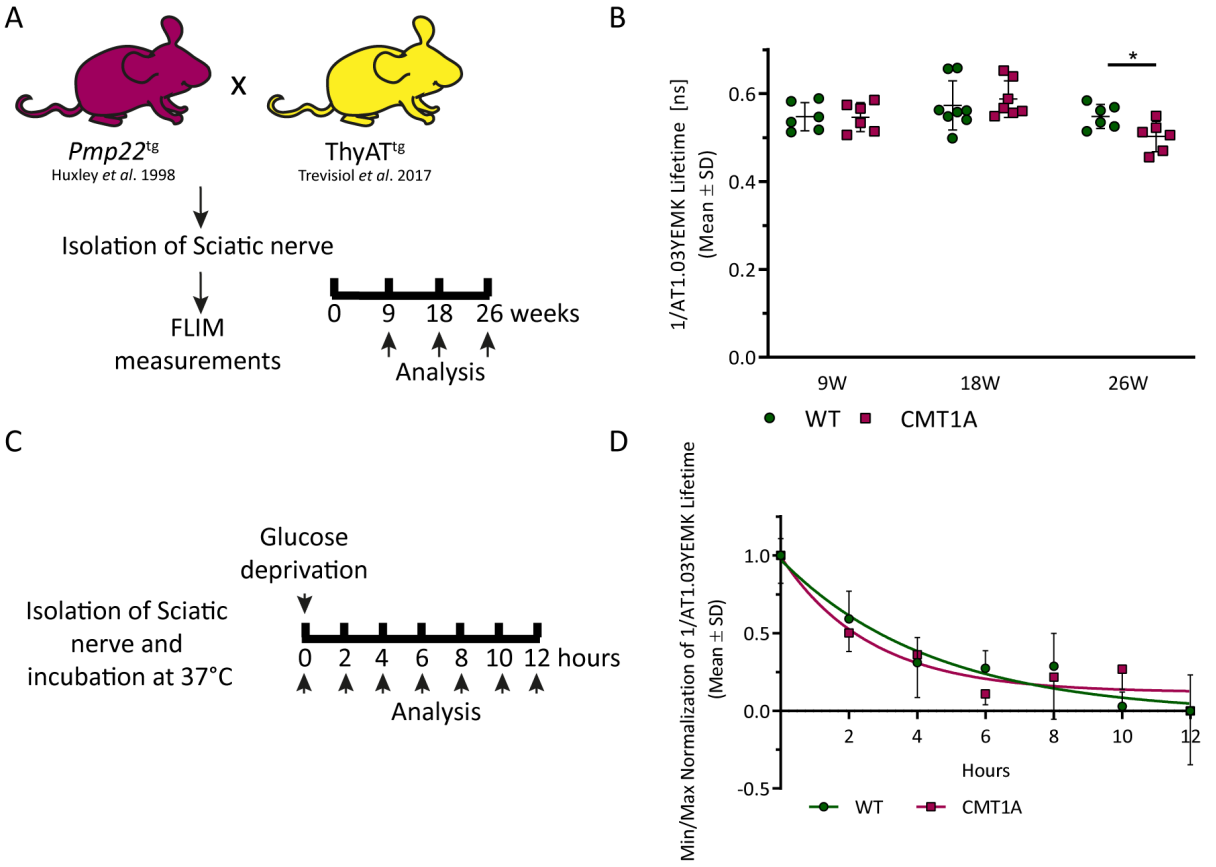

Figure 14: Reduced ATP levels in *Pmp22*^{tg} mice with old age. CMT1A mice were crossbred to ThyAT^{tg} animals (A). (B) FLIM analysis of lifetime of the FRET sensor in sciatic nerves at 9W, 18W and 26W. Values depicted as 1/lifetime. Glucose deprivation (C) analyzed over 12 hours (D) for sciatic nerves of 9W old animals (n=4). Values were normalized to Baseline at time point 0 (1) and final value at 12h time point (0). Analysis script for FLIM data written by Andrea Trevisiol (Trevisiol et al 2020). (Mean ± SD Students T-Test, p-value ≤0.05 *)

In an attempt to observe how *Pmp22*^{tg} nerves behave under challenges, sciatic nerves were freshly isolated from 9W old animals and incubated at 37°C without glucose. Nerves were measured at several time points up to 12 hours. The resulting lifetime values were normalized to 1 (at time point zero) and to 0 (at 12 hours) and a nonlinear regression was fitted. The curve of the WT and CMT1A nerves do not differ much (**Figure 14D**).

3.1.7. *Slc2a3* knockout (KO) in neurons of the peripheral nervous system

Taking into account all the presented results towards changes in glucose metabolism in *Pmp22*^{tg} animals, it would be of interest to decipher the role of glucose transport into the distinct compartments in peripheral nerves. GLUT3 is hypothesized to be the main neuronal glucose transporter in the PNS. *Slc2a3* floxed animals (Fidler et al 2017) were used and specific knock outs were generated by crossing the mice to a line expressing *cre* recombinase under the *Olig2* promoter (Dessaud et al 2007) (**Figure 15A**). *Olig2* is expressed in oligodendrocytes in the CNS, but in the PNS, the promoter drives expression in motor neurons, projecting motor fiber from the ventral horn into the periphery. Recombination PCR experiments were performed in several tissues to test for specific recombination. It was expected to show recombination bands in samples obtained from the CNS (e.g. animal three and four from the left) (**Figure 15B**). However, in a group of animals, exemplary depicted in the second animal from the left, recombination bands were detected in all tissue samples taken from the animals. In conclusion, in this breeding germline recombination is a common factor. Due to a high mortality of young animals (20% of all animals were found dead; mostly between 2-3W of age), breeding of this line was stopped.

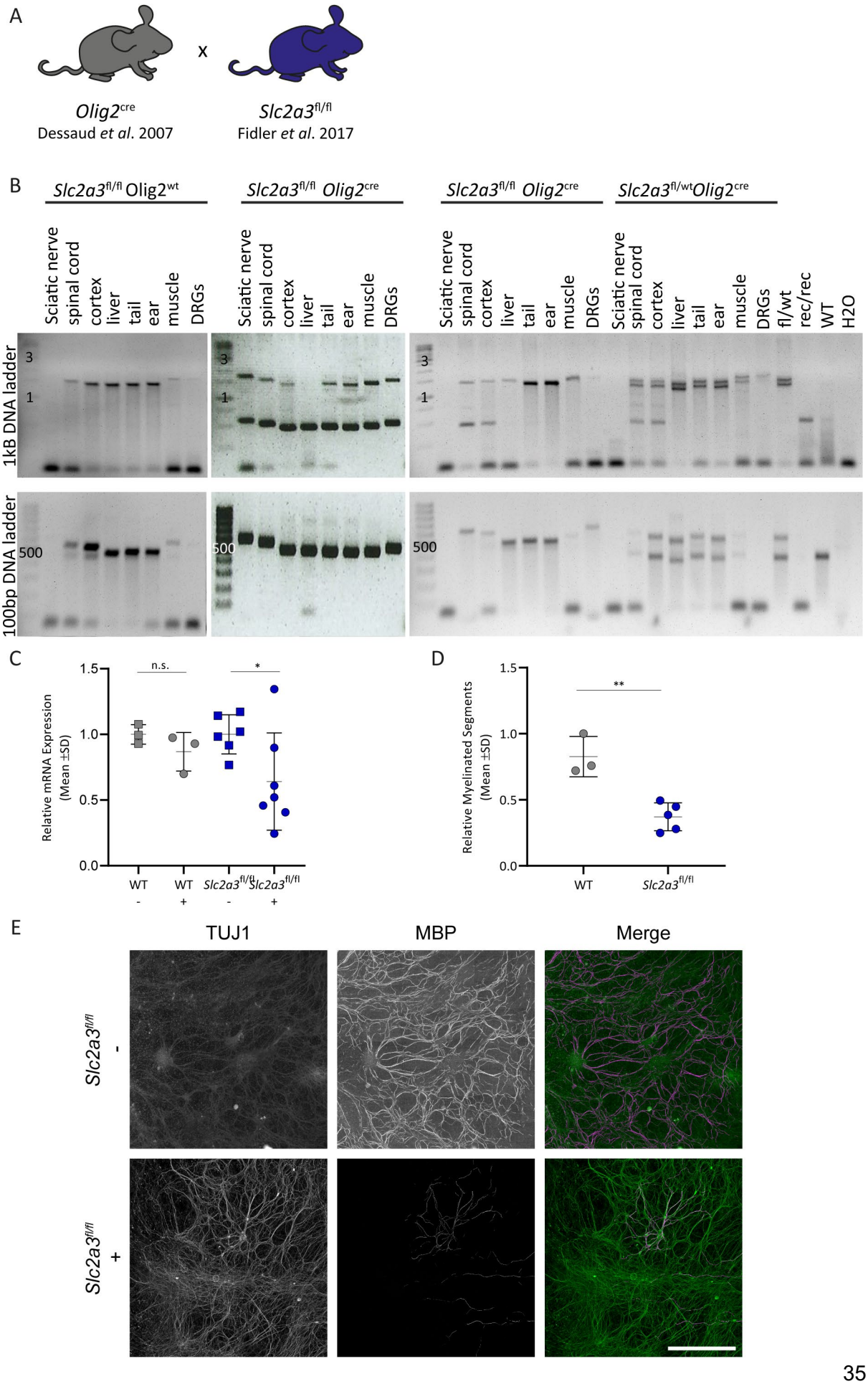
A
x
Olig2cre
Dessaud et al. 2007
Slc2a3fl/fl
Fidler et al. 2017
B
Slc2a3fl/fl Olig2wt
Slc2a3fl/fl Olig2cre
Slc2a3fl/fl Olig2cre
Slc2a3fl/wtOlig2cre
Sciatic nerve
spinal cord
cortex
liver
tail
ear
muscle
DRGs
fl/wt
rec/rec
WT
H2O
1kB DNA ladder
100bp DNA ladder
3
1
500
C
Relative mRNA Expression (Mean ±SD)
n.s.
*
WT
WT
Slc2a3fl/fl
Slc2a3fl/fl
D
Relative Myelinated Segments (Mean ±SD)
**
E
TUJ1
MBP
Merge
Slc2a3fl/fl
-
+

DRG co-cultures of the flox line of *Slc2a3* were used to analyze the effect of a neuronal specific KO. DRGs from embryos at E13.5 were dissected and cultured over several weeks. When inducing myelination by adding ascorbic acid to the culture medium, segments positive for compact myelin markers could be seen along the outgrown axons in culture. Co-cultures of *Pmp22^{tg}* embryos show lower amounts of myelinated segments, mirroring the histologic phenotypes observed in the animals later on. AAVs expressing cre recombinase under the human synapsin promoter were added to the medium of cultures from WT animals and from flox allele animals. As depicted in **Figure 15C** qRT-PCR of cell culture lysates was performed at the end of the protocol and a significant reduction in *Slc2a3* mRNA expression was detected in cultures harboring the flox allele with the AAVs in the medium in comparison to no viral particles, while this was not observed in the WT control cultures (WT (no AAV: 1±0.07; AAV added: 0.87±0.15; p=0.24), *Slc2a3*$^{fl/fl}$ (no AAV: 1±0.15; AAV added: 0.64±0.37; p=0.048)). When the myelinated segments were analyzed in the cultures a reduction in myelinated segments was observed in *Slc2a3$^{fl/fl}$* cultures with AAVs in the medium in comparison to WT cultures, while staining for axons (TUJ1) appeared unaltered (WT:0.83±0.15; *Slc2a3$^{fl/fl}$*:0.37±0.11; p=0.002) (**Figure 15D** and **E**).

3.1.8. Schwann cell specific *Slc2a1* deletion results in a mild phenotype in peripheral nerves and has no tremendous effect on *Pmp22^{tg}* mice

The next rational was to analyze the importance of GLUT1 in peripheral nerves of *Pmp22^{tg}* animals. In order to achieve a SC specific KO of *Slc2a1*, animals homozygous for the flox allele were bred (Young et al 2011) to animals expressing *cre* recombinase under the *Dhh* promoter (Jaegle et al 2003) and to *Pmp22^{tg}* mice (**Figure 16A**). Stainings for GLUT1 in teased fiber preparations confirmed the removal of the transporter from SCs (**Figure 16C**).

Figure 15: Knockout of *Slc2a3* in motor neurons in mice. *Slc2a3* floxed animals were crossbred with under *Olig2* promoter *cre* expressing animals (A). (B) PCR analysis for recombination of the floxed locus revealed germline recombination (PCR done by Katrin Haase during her Master Thesis (Supervision credits)). DRG co-cultures of floxed animals were treated with *cre* recombinase expressing AAVs in the culture medium and mRNA expression of *Slc2a3* (C) and myelinated segments depicted as fold change of +AAV condition of –AAV condition for the corresponding genotype (D). Exemplary images of staining of cultures quantified (E). Stained are Axons (TUJ1) and Myelinated Segments (MBP) (Scale bar: 500µm). (Mean ± SD Students T-Test, p-value ≤0.05 *, ≤0.01**)

From herein, the knockout of GLUT1 in SC is called SC-KO, while the removal of the transporter from SCs in *Pmp22^{tg}* animals is referred to as SC-KO *Pmp22^{tg}*.

A characterization of transporter expression was performed at 18W on mRNA (**Figure 16E**) and protein level (**Figure 16B** and **D**). *Slc2a1* expression was reduced significantly in SC-KO compared to a control group. The downregulation in *Pmp22*^{tg} animals was shown compared to Control (Ctrl). The expression was not further reduced by the SC-KO *Pmp22^{tg}* (Ctrl: 1±0.09; SC-KO: 0.72±0.11; *Pmp22^{tg}*:0.73±0.14; SC-KO *Pmp22^{tg}*:0.68±0.13 ;(p-values: WT/SC-KO=0.007; WT/*Pmp22^{tg}*=0.0026; *Pmp22^{tg}* /SC-KO *Pmp22^{tg}* =0.924). When analyzing GLUT1 expression, SC-KO showed partially reduced protein levels and *Pmp22^{tg}* animals showed the already observed increase in protein. This increase was reduced to SC-KO levels in SC-KO *Pmp22^{tg}* samples (Ctrl: 1±0.32; SC-KO: 0.74±0.14; *Pmp22^{tg}:*1.26±0.44; SC-KO *Pmp22*^{tg}: 0.61±0.32; (p-values: WT/SC-KO=0.18; WT/ *Pmp22^{tg}* =0.37; *Pmp22^{tg}* /SC-KO *Pmp22^{tg}* =0.054).

As a next step, the expression of GLUT3 was analyzed to control for possible compensations. *Slc2a3* was not significantly changed across any of the four groups (Ctrl: 1±0.24; SC-KO: 1.12±0.16; *Pmp22^{tg}*:1.23±0.16; SC-KO *Pmp22*^{tg}:1.19±0.16; (p-values: WT/SC-KO=0.49; WT/ *Pmp22^{tg}* =0.29; *Pmp22^{tg}* /SC-KO *Pmp22^{tg}* =0.85). Expression of GLUT3 protein remained at similar levels as well (Ctrl: 1±0.29; SC-KO: 1.27±0.39; *Pmp22^{tg}*:1.45±0.5; SC-KO *Pmp22^{tg}*:1.05±0.51; (p-values: WT/SC-KO=0.31; WT/ *Pmp22^{tg}* =0.17; *Pmp22^{tg}* /SC-KO *Pmp22^{tg}* =0.3).

The expression of monocarboxylate transporter was studied as well. *Slc16a1* was slightly reduced in SC-KO animals indicating a trend as well as significantly reduced in *Pmp22^{tg}* animals in comparison to the Control (Ctrl:1±0.06; SC-KO:0.83±0.14; *Pmp22^{tg}*:0.67±0.1; SC-KO *Pmp22^{tg}*:0.73±0.06; (p-values: WT/SC-KO=0.06; WT/*Pmp22^{tg}* =0.003; *Pmp22^{tg}*/SC-KO *Pmp22^{tg}*=0.3). However, in protein expression of MCT1 no alterations in abundance could be observed (Ctrl: 1±0.4; SC-KO: 1.07±0.54; *Pmp22^{tg}*:1.05±0.2; SC-KO *Pmp22^{tg}*:0.77±0.29; (p-values: WT/SC-KO=0.84; WT/*Pmp22^{tg}* =0.85; *Pmp22^{tg}*/SC-KO *Pmp22^{tg}* =0.18).

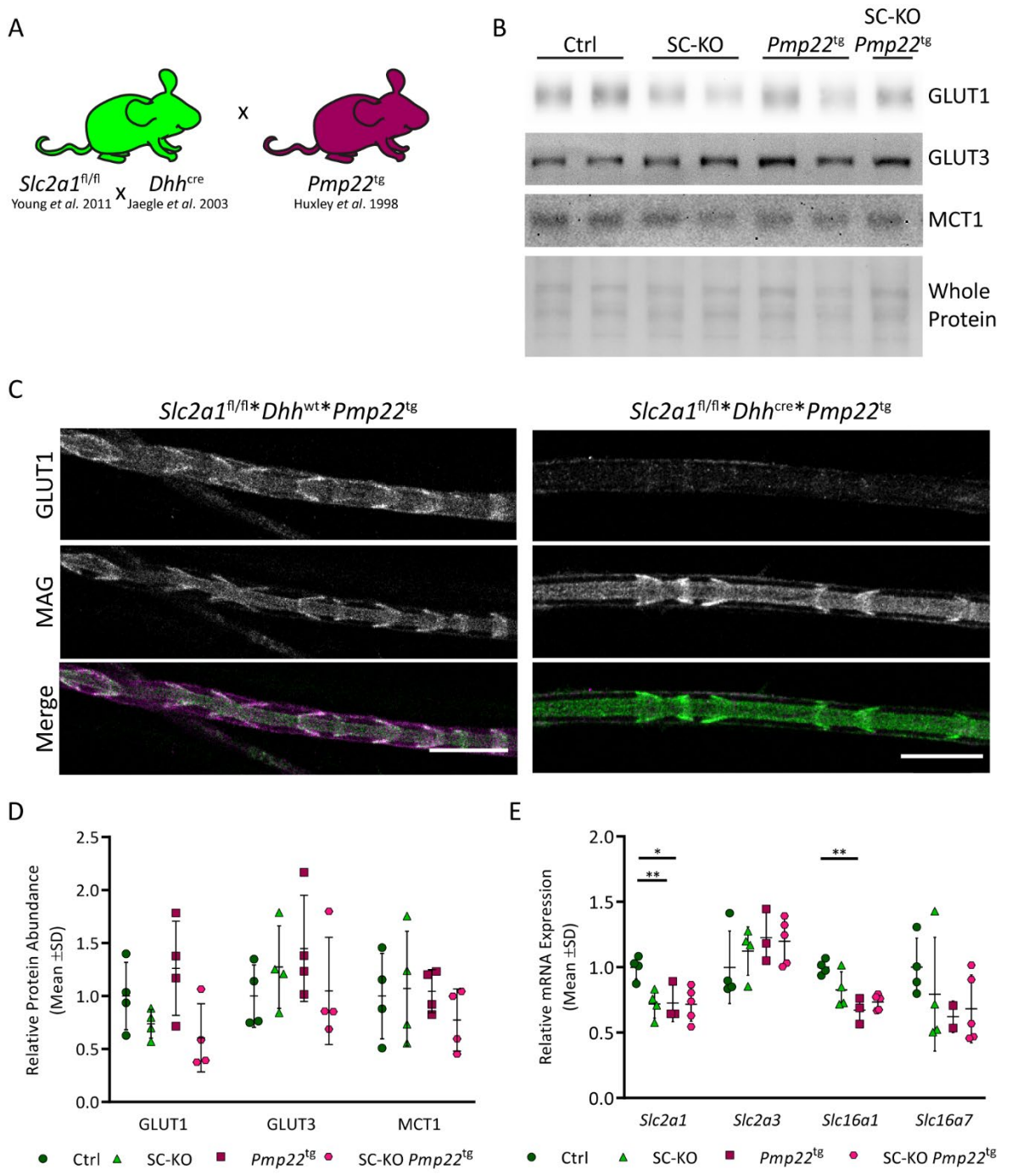

Figure 16: SC specific KO of *Slc2a1* in *Pmp22^{tg}* mice. (A) Animals with exons of Slc2a1 floxed were crossbred to animals expressing *cre* recombinase under the *Dhh* promoter and to *Pmp22^{tg}* mice. (C) Immunofluorescent labeling of GLUT1 and MAG (non-compact myelin) in teased fiber preparation of sciatic nerves verifies deletion of GLUT1 from Schwann cells. (B) and (D) Western blot analysis of sciatic nerve lysates and (E) qRT-PCR of tibial nerve lysates at 18W shows partial depletion of GLUT1 (*Slc2a1*) while other transporters as GLUT3 (*Slc2a3*) and MCT1 (Slc16a1) and Slc6a7 are not affected by the removal of GLUT1. (Mean ± SD, Students T-Test, p-value ≤0.05 *, ≤0.01**)

Slc16a7 encoding for MCT2, showed no significant changes in expression of mRNA across the four groups (Ctrl: 1±0.22; SC-KO: 0.79±0.43; *Pmp22^{tg}*:0.62±0.12; SC-KO *Pmp22^{tg}*:0.63±0.26; (p-values: WT/SC-KO=0.43; WT/*Pmp22^{tg}* =0.1; *Pmp22^{tg}*/SC-KO *Pmp22^{tg}* =0.77).

In conclusion, GLUT1 was successfully knocked out from SC. Upon KO, no evidences for compensatory upregulation of mRNAs of *Slc2a3, Slc16a1* and *Slc16a7* could be found. The already reported increase of GLUT1 levels in CMT1A could be replicated. The SC-KO in *Pmp22^{tg}* had no effect on transporter expression in peripheral nerves.

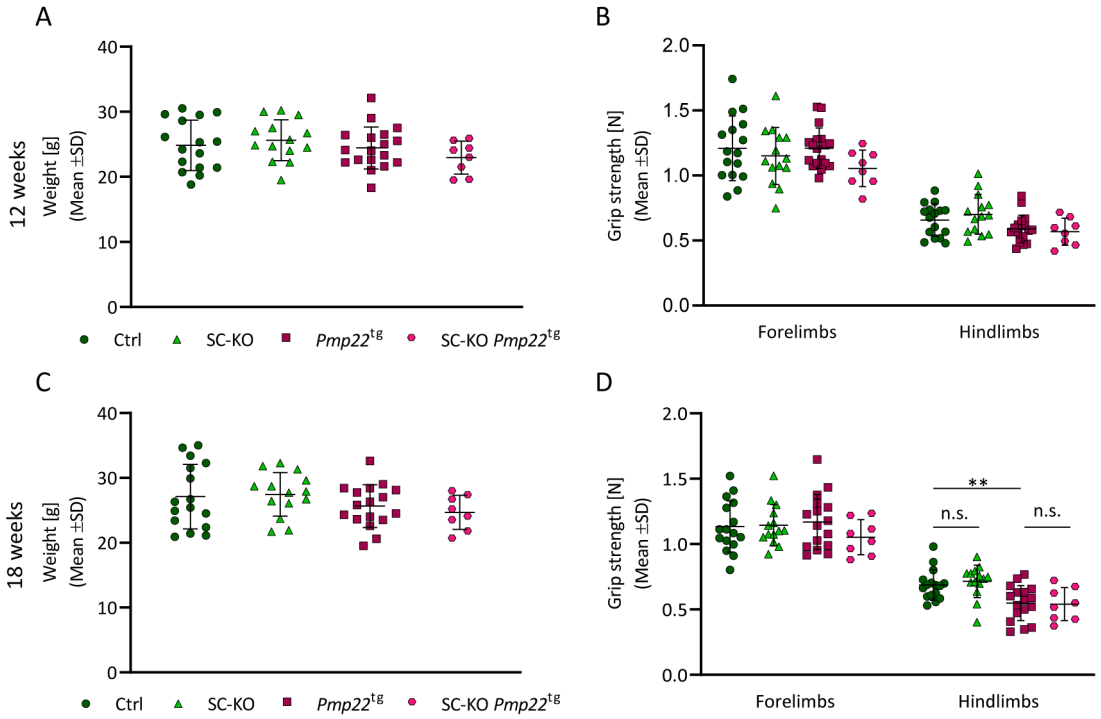

Figure 17: Grip strength measurements of SC-KO of GLUT1 in *Pmp22^{tg}* mice are unchanged. Weight of animals at 12W (A) and 18W(C) shows no obvious effect on body condition. Grip strength of forelimbs and hind limbs at 12W (B) and 18W (D) show a significant reduction in *Pmp22^{tg}* animals for hind limb grip strength at 18W. SC-KO in these animals had no effect on both measurements. Behavior was done together with Doris Krauter (Mean ± SD, nested 1way ANOVA, p-value ≤0.01**)

Subsequently, body weight of the animals was tracked at 12W and 18W to get an impression of overall condition. At 12W (Ctrl:24.8g±3.9, SC-KO:25.6g±3.1, *Pmp22^{tg}*:24.4g±3.2; SC-KO *Pmp22^{tg}*:23.0g±2.5; (p-values: WT/SC-KO=0.56; WT/*Pmp22^{tg}* =0.74; WT/SC-KO *Pmp22^{tg}*=0.22)) and at 18W (Ctrl:27g±5; SC-KO:27.5g±3.4; *Pmp22^{tg}*:25.6g±3.3; SC-KO *Pmp22^{tg}*:24.7g±2.6; (p-values: WT/SC KO=0.82; WT/*Pmp22^{tg}* =0.33, WT/SC-KO *Pmp22^{tg}* =0.21)) the three experimental groups did not differ from control animals (**Figure 17A** and **C**). Next, grip strength of forelimbs and hind limbs was analyzed at 12W and 18W. At 12W, the grip strength of the forelimbs was unchanged across all four groups (Ctrl: 1.21N±0.25; SC-KO: 1.15N±0.22; *Pmp22^{tg}*:1.21N±0.16; SC-KO *Pmp22^{tg}*:1.05N±0.14; (p-values: WT/SC-KO=0.42; WT/ *Pmp22^{tg}* =0.99; *Pmp22^{tg}*/SC-KO *Pmp22^{tg}*=0.07)). For the hind limbs, all animals performed around the same strength measured (Ctrl: 0.66N±0.13; SC-KO:

0.70N±0.15; *Pmp22*^{tg}:0.59N±0.11; SC-KO *Pmp22*^{tg}:0.57N±0.1; (p-values: WT/SC-KO=0.25; WT/ *Pmp22*^{tg}=0.12; *Pmp22*^{tg}/SC-KO *Pmp22*^{tg}=0.67) (**Figure 17B**).

At 18W, the measurements were repeated. Again, no obvious differences for forelimb grip strength in all animals was detected (Ctrl: 1.13N±0.2; SC-KO: 1.14N±0.16; *Pmp22*^{tg}:1.17N±0.21; SC-KO *Pmp22*^{tg}:01.05N±0.13 (p-values: WT/SC-KO=0.88, WT/ *Pmp22*^{tg}=0.45, *Pmp22*^{tg}/SC-KO *Pmp22*^{tg}=0.11). However, at 18W the already reported reduced grip strength of *Pmp22*^{tg} animals in comparison to control animals could be replicated (Ctrl: 0.69N±0.12; SC-KO: 0.72N±0.12; *Pmp22*^{tg}:0.55N±0.13; SC-KO *Pmp22*^{tg}:0.54N±0.13; (p-values: WT/SC-KO=0.55; WT/ *Pmp22*^{tg}=0.003; *Pmp22*^{tg}/SC-KO *Pmp22*^{tg}=0.87). SC-KO animals did not show a difference in comparison to a Control group of animals, as well as the SC-KO in CMT1A did not differ from the group of *Pmp22*^{tg} animals (**Figure 17D**).

After grip strength analysis at 18W, the animals were anesthetized and electrophysiology measurements performed. SC-KO animals showed no difference in electrophysiological profiles compared to the Control group. *Pmp22*^{tg} animals showed the expected differences typical for the mouse model, stated in the following. Nerve conduction velocity, as already described, is severely reduced in CMT1A. **In Figure 18B** a highly significant reduction was observed in the experimental group (Ctrl: 27.66m/s ±2.04; SC-KO: 30.57m/s ±8.23; *Pmp22*^{tg}:24.38m/s ±2.72; SC-KO *Pmp22*^{tg}:23.46m/s ±5.08; (p-values: WT/SC-KO=0.2; WT/ *Pmp22*^{tg}=0.0007; *Pmp22*^{tg}/SC-KO *Pmp22*^{tg}=0.57)). An additional KO of GLUT1 in SC did not alter the NCV compared to *Pmp22*^{tg}.

Additionally, amplitudes of CMAPs after proximal and distal sciatic nerve stimulations were analyzed (**Figure 18A**). In CMT1A, it has been described that amplitudes of CMAPs reduce corresponding to the reduced muscle strength observed as well. In our study, amplitudes after distal stimulation (Ctrl:32.39mV ±9.63; SC-KO:27.65mV ±10.07; *Pmp22*^{tg}:21.69mV ±6.5; SC-KO *Pmp22*^{tg}:22.93mV ±7.65; (p-values: WT/SC-KO=0.2; WT/ *Pmp22*^{tg}=0.0007, *Pmp22*^{tg}/SC-KO *Pmp22*^{tg}=0.91)) as well as amplitudes after proximal stimulation (Ctrl:26.9mV ±5.94; SC-KO:24.53mV ±5.61; *Pmp22*^{tg}:17.83mV ±5.23; SC-KO *Pmp22*^{tg}:19.15mV ±7.44; (p-values: WT/SC-KO=0.29; WT/*Pmp22*^{tg}=0.0001, *Pmp22*^{tg}/SC-KO *Pmp22*^{tg} =0.62)) were reduced for *Pmp22*^{tg} animals compared to control animals, while SC-KO did not alter the amplitudes significantly.

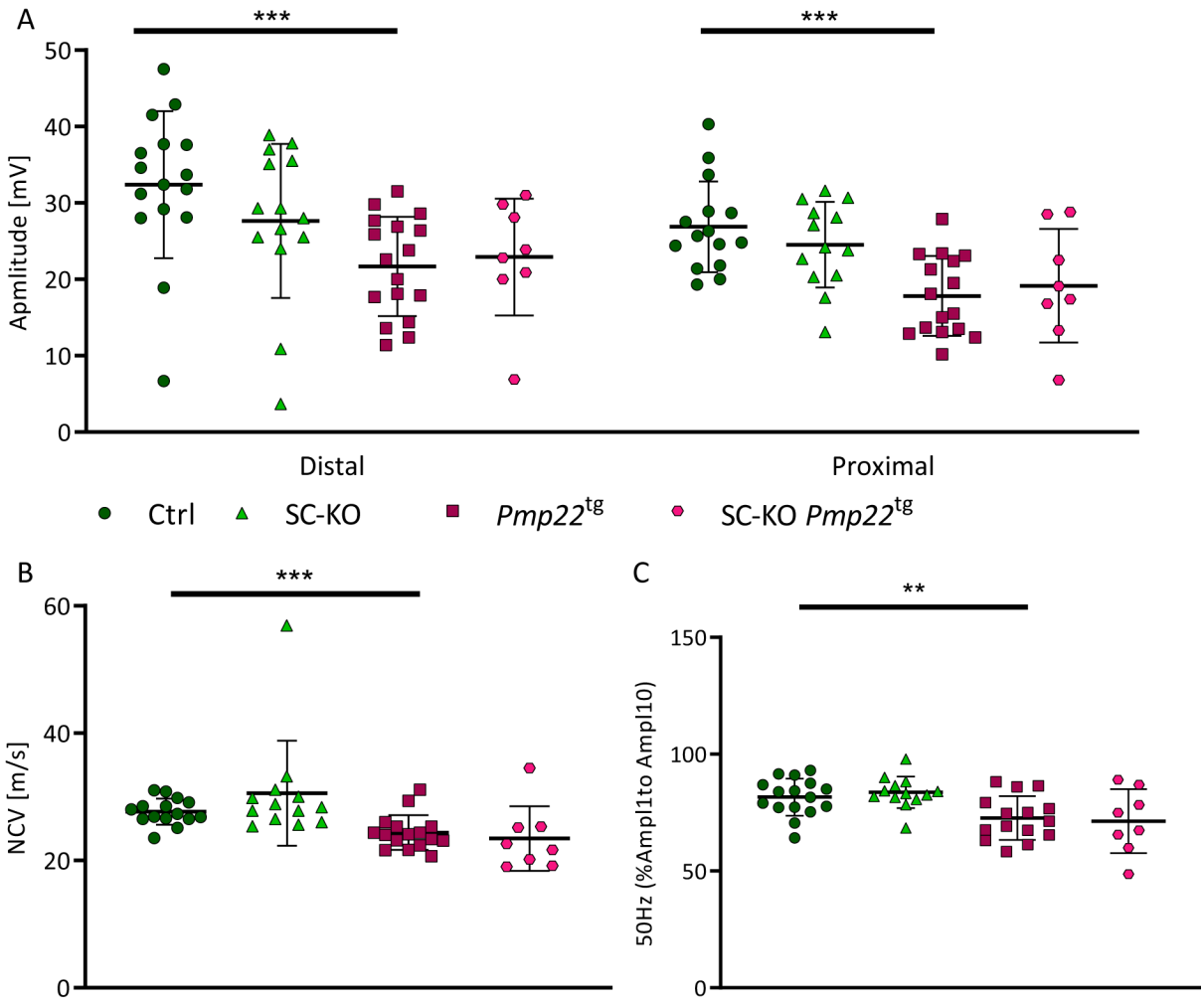

Figure 18: Electrophysiological analysis of *Slc2a1* SC-KO in *Pmp22*^{tg} mice. Analysis done at 18W. Depicted are motoric signals measured after sciatic nerve stimulation. Distal and proximal amplitude (A), NCV (B) and reduction of first to tenth amplitude during repetitive stimulation at 50Hz (C). *Pmp22*^{tg} animals present with reduced amplitudes and reduced NCV. SC-KO show no difference to control animals while SC-KO in *Pmp22*^{tg} shows no amelioration in disease phenotype. Electrophysiology was performed by Theresa Kungl (Mean ±SD; Students T-test; p≤0.01**; p≤0.001***)

Repetitive stimulations were performed as well. Sciatic nerves were stimulated with 50Hz and amplitudes were measured and compared between the 1st and 10th amplitudes recorded. Data is shown in **Figure 18C**. While control animals showed a reduction to 81.63% ±7.88, *Pmp22*^{tg} animals 10th amplitude was at 72.65% ±9.36 of the first one. This was not altered by SC-KO of GLUT1 in each of the groups (SC-KO; 83.69% ±6.78; SC-KO *Pmp22*^{tg}:71.34% ±13.66; (p-values: WT/SC-KO=0.46, WT/ *Pmp22*^{tg}=0.007, *Pmp22*^{tg}/SC-KO *Pmp22*^{tg}=0.79).

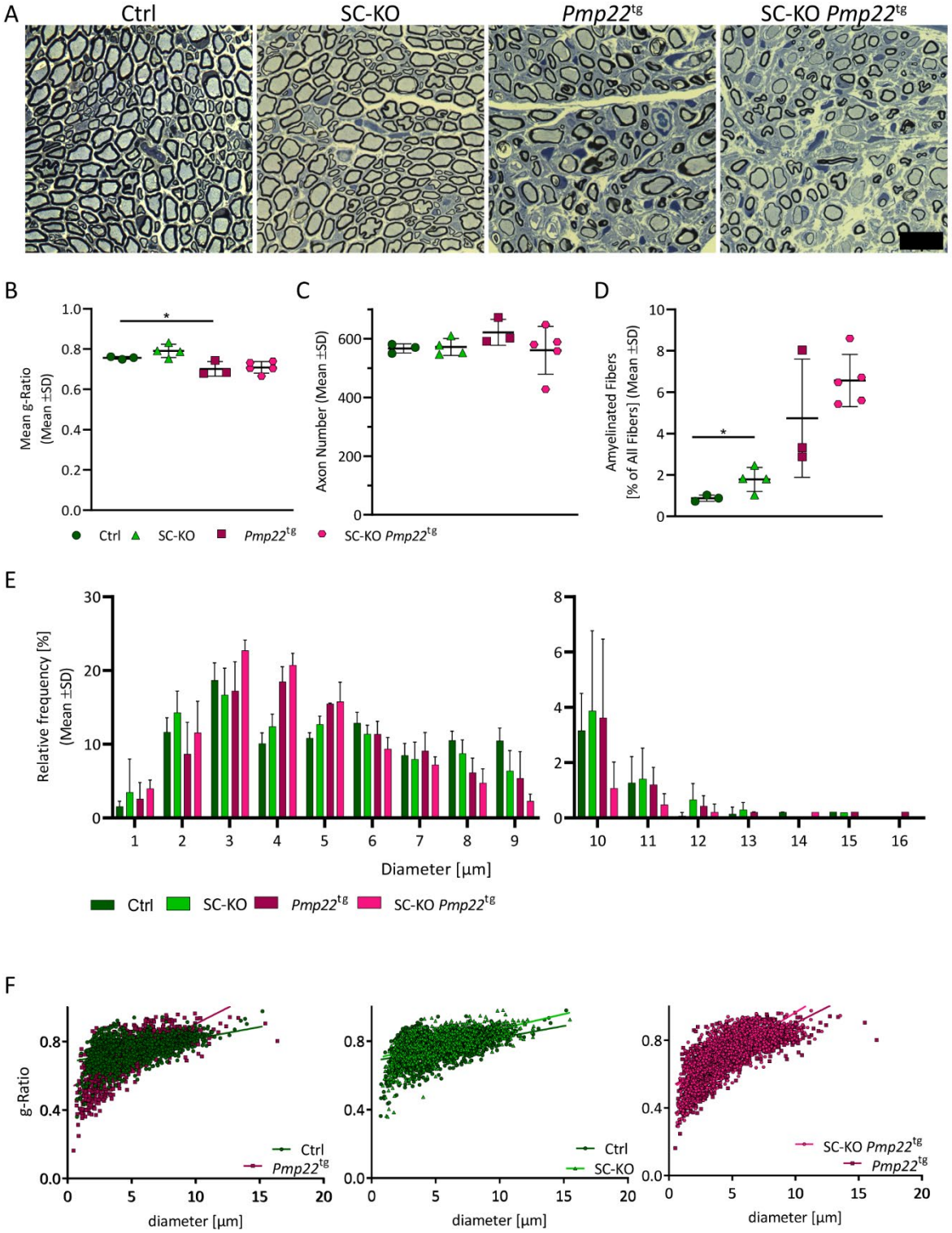

Figure 19: Histological analysis revealed no aberrant phenotype in SC-KO of GLUT1 in *Pmp22^{tg}* mice. Example pictures of semi-thin cross-sections of femoral nerves from 18W old animals gallyas-silverimpregnated and additionally stained with azurII blue (Scale bar: 20µm) (A). Mean g-ratio (B), total axon number (C) and percentage of amyelinated fibers (D) for all genotypes showed a small increase of amyelinated fibers in SC-KO. Distribution of axon diameter (E) and g-ratio depicted with corresponding axon diameter and linear regression line (F). (Mean ± SD, Students T-Test, p-value ≤0.05 *)

Histological analysis at 18W of age was done in femoral nerves. Cross sections were silver impregnated (gallyas, myelin) and azurII blue (membranes) as shown exemplary in **Figure 19A** for all four groups.

A g-ratio analysis was done by measuring the area of the outer myelin and the area of axon. The axonal values were divided by the myelin values for each axon/myelin unit respectively. An amyelinated axon would give rise to a value of 1. The thicker the myelin sheath is in comparison to the axon the lower the g-ratio is. In this study mean g-ratio of all axon in the femoral nerve, graphed in **Figure 19B** was unchanged in SC-KOs (Ctrl: 0.76 ±0.01; SC-KO: 0.79 ±0.05; *Pmp22^{tg}*:0.7±0.04; SC-KO *Pmp22^{tg}*:0.71±0.03; (p-values: WT/SC-KO=0.15; WT/ *Pmp22^{tg}*=0.04, *Pmp22^{tg}*/SC-KO *Pmp22^{tg}*=0.73). Comparable to earlier reports in literature, *Pmp22^{tg}* mice show a slight increase in mean g-ratio, which remains the same for SC-KO in CMT1A. An additional parameter analyzed is the total axonal number in the entire nerve (**Figure 19C**). Axonal numbers remain comparable across all animals analyzed (Ctrl: 567±16; SC-KO: 572±29; *Pmp22^{tg}*:622±44; SC-KO *Pmp22^{tg}*:561±81; (p-values: WT/SC-KO=0.81; WT/ *Pmp22^{tg}*=0.11; *Pmp22^{tg}*/SC-KO *Pmp22^{tg}*=0.28). Shown in **Figure 19D** is the relative amount of amyelinated fibers in comparison to all fibers in the nerve cross section. SC-KO showed as slight significant increase in amyelinated fibers in comparison to age matched control animals, while a trend towards more amyelinated fibers in *Pmp22^{tg}* animals could be observed, due to high interindividual variability within this group (Ctrl: 0.88% ±0.15; SC-KO:1.78% ±0.58; *Pmp22^{tg}*:4.74% ±2.86; SC-KO *Pmp22^{tg}*:6.57% ±1.26; (p-values: WT/SC-KO=0.05; WT/ *Pmp22^{tg}*=0.08; *Pmp22^{tg}*/SC-KO *Pmp22^{tg}*=0.25).

Depicted in **Figure 19F** is the distribution of g-ratio with corresponding axonal diameter. *Pmp22^{tg}* animals showed the typical increase of amyelinated larger caliber axons and smaller caliber axons were hypermyelinated. The cloud of SC-KO animals tended to shift up towards higher g-ratios across all axonal calibers. When comparing SC-KO *Pmp22^{tg}* animals with *Pmp22^{tg}* mice, the typical cloud distribution was maintained with a small shift towards higher g-ratio for the same axonal caliber, suggesting an additive effect of SC-KO and *Pmp22^{tg}* phenotype.

In conclusion, SCs lacking GLUT1 seemed to be not affected in their ability to myelinate and animals seemed to behave like their age matched controls. When

removing GLUT1 from *Pmp22*^{tg} animals all the above reported parameters remained unaltered.

3.2. Discussion

Overexpression of *Pmp22* causes a dysmyelinating peripheral neuropathy known as CMT1A (Li et al 2013, Lupski et al 1991, Raeymaekers et al 1991). Hallmarks are strongly reduced NCV and histological dysmyelination starting early on with reduced internodal length. Additionally, over time CMAP measurements are reduced and histologically axonal loss can be observed. It has been reported, that this axonal loss, as well as the reduced CMAP measurements correlate with disease severity, while dysmyelination happens early on already (Rossor et al 2015, Saporta et al 2009, Shy et al 2005b). Many studies have been conducted to unravel the mechanism behind this disease. Especially, since no treatment has been established yet, besides treatments to lighten symptom burden for patients. For years, there were emerging evidence for metabolic alterations. In the animal model a study in 2012 connected changes in metabolism in sciatic nerves to disease severity (Fledrich et al 2012a). Aditionally, a study by Ravera and colleagues published evidence towards impairment of SC mitochondria in the same animal model (Ravera et al 2013). However, only studies to restore the myelin itself by supplementation of lipids have been conducted (Fledrich et al 2018). The actual glial to axon support has not been investigated in detail even though more and more evidence has emerged for axonal support by Schwann cells in health and other neurpathies, e.g. failing metabolism in SCs leads to axonal degeneration (Beirowski et al 2014, Fünfschilling et al 2012, Viader et al 2011). This urged for a detailed investigation of changed metabolism and axo-glial support systems in *Pmp22*^{tg} animals. Especially since CMAP is reduced over time, the question arises whether the SCs fail to support axonal energy metabolism properly, leading to the axonal loss correlating with disease severity.

3.2.1. The metabolome of peripheral nerves

In an MS based approach to analyze changes in metabolite profiles in sciatic nerve lysates at P18 and 9W, it could be shown that significant changes increased with time. While 15% of all measured compounds were significantly changed in abundance at P18, already 40% were increased or depleted at 9W. These time points were chosen, because at P18 glial cells are highly active in myelination of axons. At 9W of age, the animals are young adults and Schwann cells are more committed to maintaining the formed myelin sheath. A comparison was performed between enrichment at both timepoints within the WT and *Pmp22*^{tg} group respectively (data not shown in this thesis). From P18 to 9W direction of changes in the metabolome persists while the

expression differences between WT and CMT1A nerves exacerbate. It can therefore be concluded, that the metabolism of peripheral nerves in this animal model does not exhibit a metabolic switch during development, per se. During all analysis conducted on this data set one has to keep in mind the nature of the sample. Sciatic nerves of the animals were isolated and the epinurium removed, before thery were quickly snap frozen. The outer layer of connective tissue was removed due to its rather metabolic active nature. However, when thinking about the structure of a peripheral nerve, one has to keep in mind that all data performed on a whole nerve lysat is still a mixture of axons, Schwann cell, occasional macrophages as well as blood vessels and remaining connective tissue. Additionally, this MS based approach only represents a snap shot of a highly dynamic flux of metabolites.

3.2.2. Alterations in glucose metabolism in peripheral nerves of *Pmp22^{tg}* animals

One of the significantly enriched compounds in sciatic nerve lysates is glucose (**Figure 5** and **Figure 20**). Enriched glucose in peripheral nerves immediately reminds of a diabetic phenotype of the glial compartment. As reported in numerous studies, under hyperglycemia SCs react with an increase of the polyol pathway (Sango et al 2014, Yabe-Nishimura 1998). Surprisingly, in this study the opposite was observed. As presented in **Figure 5**, sorbitol and fructose, the two metabolites of the pathway, are 10 fold reduced in *Pmp22^{tg}* nerve lysates. Additionally, the key enzyme of the pathway, aldose reductase (AR), exhibits reduced expression on mRNA level as well. It has been reported in *in vitro* studies, that AR reacts to hyperglycemic conditions on mRNA level as well (Maekawa et al 2001). This argues against a typical reaction Schwann cell to enhanced glucose levels in CMT1A peripheral nerves.

If the polyol pathway does not react to the hyperglycemic conditions, another possibility would be changed storage dynamics. Schwann cells are reported to store glucose as glycogen (Brown et al 2012). Glycogen content in peripheral nerves of *Pmp22^{tg}* mice was measured normalized to protein content in the sample. Animals were pooled to reach sufficient amounts to be within the sensitive range of a colorimetric plate assay. The analysis takes into account background glucose levels, to eliminate false results, due to increased glucose levels in the nerves. The results, shown in **Figure 6** did not show a significant increase in glycogen in CMT1A, but rather a trend in decreased storage pools. An upregulation on mRNA level of the key enzymes of glycogen

pathways was not detected as well. These results exclude an increased storage of glucose in nerves of *Pmp22*^{tg} animals. One has to keep in mind, that a higher need for storages could be the underlying factor as well. However, both rate limiting enzymes for glycogen storage and usage were reduced on mRNA level.

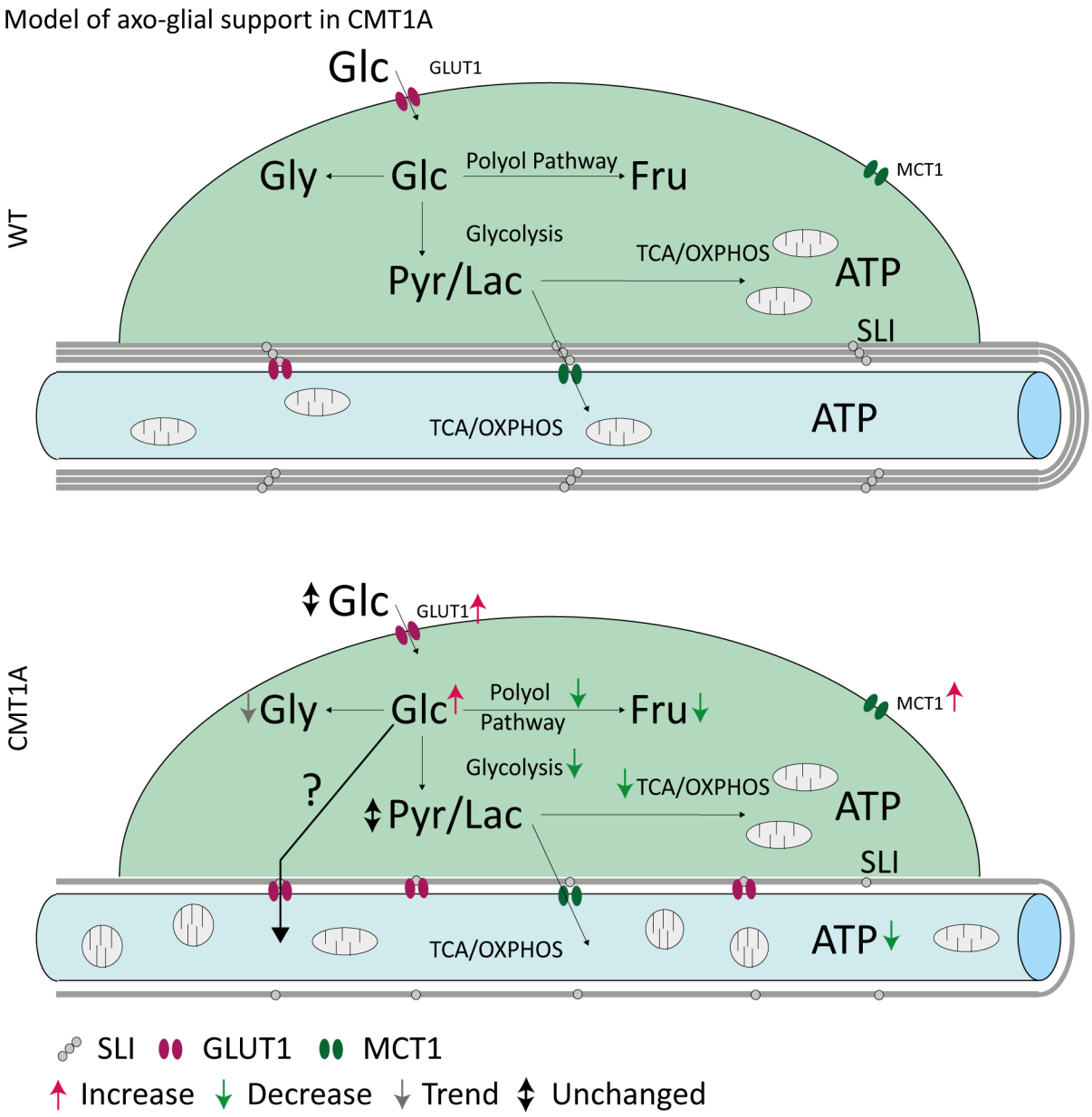

Figure 20: Model of axo-glial support in CMT1A. Upper Panel depicts the WT situation of glial axonal coupling. Glucose is taken up by the SC from the periphery and is processed to pyruvate/lactate via glycolysis. Lactate is proposed to be shuttled to the axon to fuel mitochondrial energy metabolism to support e.g. action potentials. In CMT1A (lower panel), we have shown a downregulation of mRNA of enzymes for polyol, glycolysis, glycogen and mitochondrial metabolism. While free glucose is enriched and fructose is severely depleted, pyruvate and lactate remain the same. It remains to be proven, whether free glucose is shuttled to the axonal compartment to fuel energy metabolism under disease conditions. (Glc: Glucose, Fru: Fructose, Pyr: Pyruvate, Lac: Lactate, Gly: Glycogen, SLI: Schmidt-Lanterman Incisure)

The question poses itself, are Schwann cells actually upregulating their glycolysis under CMT1A pathology conditions? As presented in **Figure 7** the glycolysis intermediate glyceraldehyde-3P is unaltered in sciatic nerve lysates. Additionally, pyruvate, the end product, and lactate, metabolized in one step from pyruvate, are maintained at wild type levels in this study. In tibial nerve lysates of the same age, glycolytic key enzymes, as well as several intermediate steps, were reduced in mRNA amounts. One has to consider the composition of a whole nerve lysate, especially when comparing mRNA expression. Schwann cell nuclei are numerously present in lysates of peripheral nerves. On the contrary, nuclei of neurons are located in the CNS and the axons project into the periphery. Nuclei of sensory fibers are located in the DRGs, while cell bodies of motor neurons can be found in the ventral horn of the spinal cord. In an attempt to evaluate this further, expression of some of the tested enzymes were compared to the expression of mRNA in DRGs. In this comparison (data not shown), no difference in glycolytic enzymes could be detected in the DRG samples of *Pmp22*^{tg} rats in comparison to WT samples. This raises evidence towards differential regulation of glycolysis in axons and SCs of peripheral nerves in the tested animal models. If it is assumed that analysis of mRNA levels in peripheral nerves represents the glial compartment rather than the axonal compartment, the question arises, where the increased glucose is metabolized, if not into metabolic pathways within the Schwann cells themselves. Data from DRGs hint towards unaltered general neuronal metabolism, which could differ from local axonal metabolism. Axonal changes are thus most likely induced by altered SC metabolic support.

3.2.3. Could glucose be transported to the axonal compartment?

Glucose transporter, reported to be responsible for glucose transport in the CNS, are expressed in the peripheral nervous system as well. GLUT1 is assumed to be the main glial transporter, while GLUT3 is suggested to facilitate diffusion on the axonal site (Jha & Morrison 2018). Expression on mRNA and protein level for the glial transporter is shown in (**Figure 7** and **Figure 8**). At first glance, the results seem to be contradicting. While *Slc2a1* levels are reduced in tibial nerves at 9W, GLUT1 is upregulated in Western Blot analysis. While mRNA content in nerve lysates may be dominated by SC nuclei rather than neuronal ones, protein is a mixture of axonal and glial compartment. Another explanation might be the disease pathology itself. As reported in patients (Sahenk & Mendell 1999, Saporta et al 2009) as well as in the animal model (Fledrich et al 2018) *Pmp22*^{tg} SCs form shorter internodes along the axon. GLUT1, as shown in

Figure 8, localizes to SLIs in the WT and it maintains this localization in disease. Shorter internodes mean, more SLIs along the same stretch of axon. This may lead to an increase in proteins localizing to the SLIs. So while *Slc2a1* expression might be influenced negatively in CMT1A the protein amount increases along the same stretch of axon analyzed due to the increase amounts of SLIs present.

Would more correctly localized transporter lead to the possibility of increased transport in the fibers? The glucose measurement represents free glucose in the nerve. Upon entry into a cell, glucose is phosphorylated to prevent an immediate export. This phosphorylation is realized by hexokinases. The amount of glucose converted to glucose-6P is limited to the amount needed in the cells for homeostasis (Dienel 2019). The transport via facilitated diffusion by GLUTs should lead to an equilibrium of glucose concentration in all compartments. When considering literature, glucose can be transported to neurons and their axons. For one, glucose transporter do localize to those membranes, as already mentioned. An uptake and utilization has been suggested for the CNS (Meyer et al 2018) as well as for the PNS (Rich & Brown 2018). Studies were *ex vivo* and conducted under block of different transport routes and deprivation conditions. Via direct transport glucose is able, to support axonal function and maintain CAPs. Supporting data for a compensational upregulation of glycolysis machinery in axons have been published for the CNS (Bas-Orth et al 2017) and the PNS (Bouçanova & Chrast 2020) as response to challenges to the axo-glial coupling. In another study by Deck and colleagues, an increase in glucose in the axonal compartment was reported, to rescue energy demand upon Schwann cell metabolism challenges (Deck et al 2020). As presented in **Figure 9** of this study, Hexokinase1 could be localized in immunofluorescent stainings to the axon and was increased in nerve lysates of *Pmp22*^{tg} animals (**Figure 8**). However, is glucose really reaching the axon in increased amounts in comparison to WT peripheral nerves? To this end, it would be necessary to localize free glucose, amongst others, in the different compartments being discussed here. As presented in **Figure 10**, experiments with sensors and labeled metabolites directed towards this question did not deliver evidence towards elucidating this topic. In order to be able to visualize actual transport fluorescently labelled compounds, e.g. 2-NBDG, could be of use. In *ex vivo* preparations of teased fibers of peripheral nerves, addition of the compound did not lead to a clear result due to experimental restraints. In the time lapse, no increase of intensity over time could be shown. The intensity rather immediately equilibrated with

the surrounding fluorescence upon addition of the compound and the fluorescent glucose seemed to stick to compact myelin, as the fluorescence coming from that area was highest in the image. Another useful tool could be sensors detecting certain metabolites expressed in specific cells by transgene integration into an animal model. A glucose FRET sensor established at the MPI-EM expressed under the control of *Cnp* promoter, in the PNS expression would be localized to SCs, did not reach sufficient intensities to be able to analyze changes in intensities (**Figure 10**). This could be due to the rather low expression rate of CNP in the PNS in comparison to the CNS (Jahn et al 2009, Siems et al 2020). An approach to circumvent such pitfalls recently used in the literature are AAV particle injections targeting certain cell types (amongst others (Deck et al 2020, van Hameren et al 2019)). By AAV injection into the ventral horn one could target motor neuronal cell bodies to reach expression of the respective sensor in the motor fibers of e.g. sciatic nerves. To yield expression in SCs the viral particles have to be injected into the epineurium surrounding the sciatic nerve in a by the animals rather well tolerated procedure. After a few weeks, these approaches can give rise to expression of the sensor in sufficient amounts for analysis in the compartment of interest. In ongoing experiments, by combining injections into ventral horn or sciatic nerves in *Pmp22^{tg}* animals and controls, the objective is to gather a specific knowledge regarding the distribution of metabolites and the changes under disease pathology.

3.2.4. Alterations in axonal mitochondria in peripheral nerves of *Pmp22^{tg}* animals

If glucose does reach the axon in increased concentrations, the question arises how the compound is metabolized to generate energy. In mitochondria, pyruvate after being reduced to acetyl-CoA enters the TCA cycle and later on fuels the electron transport chain and finally oxidative phosphorylation. As shown in **Figure 11**, expression of TCA cycle genes was analyzed by qRT-PCR. Some genes encoding enzymes catalyzing reactions in the TCA cycle are significantly down-regulated, while compounds are enriched. Genes encoding nuclear for parts of the complexes I-III are significantly reduced in amount, while none of the mitochondrial encoded candidates was altered. As already mentioned, the downregulation of nuclear expressing genes is much rather dominated by SCs than by axons taking the structure of peripheral nerve fibers into account. Is this simply the effect downstream of the observed downregulation of the entire glucose metabolism, presumably in SCs? Alternatively, do the SCs mitochondria exhibit alterations in early phases of the pathology? It has been reported by Ravera

and colleagues, that samples of isolated myelin of peripheral nerves of *Pmp22*^{tg} rats are less active in oxidative phosphorylation with age (Ravera et al 2013). Is the increase in citrate, oxaloacetate and fumarate, all part of the TCA cycle, due to axonally enriched TCA cycle activity? In the end, it matters, whether the axonal function is supported properly. As indicated in **Figure 14**, ATP measurements in *Pmp22*^{tg} animals showed maintained levels at 9W and 18W in comparison to WT animals. Therefore, at stages where significant changes can be observed in metabolome and mRNA analysis, the general ATP pools of axons do not seem affected. At 26W, a stage where nerves present with solid axonal degeneration, the analysis revealed reduced levels of ATP in axons of CMT1A animals. At 12W, the analysis of roGFP2 Grx1 redox state revealed less oxidized in mitochondria in axons of *Pmp22*^{tg} mice (**Figure 13**). Every time mitochondria are active in *in vivo* measurements, a short spike of oxidation can be seen on the single mitochondria level (van Hameren et al 2019). In the presented analysis here, an average of all fluorescent pixel was taken, leading to an average of all mitochondria in the field and plane of view. If more mitochondria are not active meaning not spiking in oxidation levels at the moment when the snap shot is taken, the average decreases. Are mitochondria in *Pmp22*^{tg} animals less active and lead to a reduced ATP pool over time? It is reported in the literature, that axons at rest often times do not reveal differences in energy pools, which become evident under challenge. In a study of an animal model of CMT2A ATP basal levels were normal and the axons only failed to increase their pools upon stimulation in saphenous nerves (van Hameren et al 2019). Deck and colleagues reported a similar finding for a genetic manipulation of lactate supply by SCs towards axons. A deficiency of lactate in axons only became apparent upon stimulation (Deck et al 2020). In the literature, it has been reported that glycogen, present in Schwann cells, supports the challenges a high frequency stimulation poses for a sciatic nerve *ex vivo* (Brown et al 2012, Rich & Brown 2018). With the trend towards reduced glycogen storages, already discussed, would this mean fibers in CMT1A are not able to compensate for raised energy demands under challenges? In electrophysiology (**Figure 18**), *Pmp22*^{tg} animals show reduced ability to keep amplitudes constant upon repetitive stimulation, indicating difficulties with high frequency stimulations. Under glucose deprivation *ex vivo* without stimulation of sciatic nerves acutely isolated at 9W (**Figure 14**), nerves from *Pmp22*^{tg} animals had a trend towards a steeper slope of decrease. The data shown is normalized to 1 at time point zero, which is the baseline level of ATP in fibers in sciatic nerves. The last

time point at 12 hours was set to 0. It is assumed here, that the nerves plateau in their values when they reach depletion. It has been reported before, that sciatic nerves under glucose deprivation and baseline stimulations CAPs start to fail around two hours and reach total failure at 4.5 hours (Brown et al 2012). This is around the time, where values in this study reach a plateau like behavior. A control at 10mM glucose until 12 hours was not performed, but based on literature sciatic nerves keep a stable CAP under 10mM glucose for up to eight hours (Rich & Brown 2018). Therefore, it would not be expected, to observe a similar behavior under high glucose conditions, but rather that the decline results from the deprivation conditions. To unravel differences between the genotypes, it could be beneficial, to shorten the time span of the experiment, but to increase the time resolution. This would deliver more precise insight into how the dynamics of ATP levels are behaving in *Pmp22^{tg}* animals in comparison to controls. A complementary approach would be an additional challenge presented to the nerves, e.g. high frequency stimulations. In electrophysiology measurement of *Pmp22^{tg}* mice at 18W, (**Figure 18**) repetitive stimulations revealed a higher reduction of the amplitudes over time in comparison to WT animals. This indicates a phenotype under exhaustion. Possibly the fibers, also due to the dysmyelination phenotype exhibit a mixture of action potential profiles. Demyelinated segments lead to slower conduction velocities in comparison to myelinated fibers, potentially to temporary conduction blocks. In consequence, fewer fibers elicit muscle action potentials at the same time, reducing the CMAPs, nonetheless the ATP pools would be sufficient to keep up action potentials initially.

As reported in this study in **Figure 12** alterations in mitochondrial morphology could be observed for organelles in axons of *Pmp22^{tg}* animals. The results suggest that mitochondria are, in comparison to the WT group, rather fragmented and a population of organelles is enlarged in cross section. It was shown, that MT-CO1 is significantly enriched in protein analyses of whole nerve lysates. This difference cannot be found in primary Schwann cell culture. The observed enrichment does not seem to be an SC intrinsic change, but rather comes from the axonal compartment or the axo-glial interaction. To this end, it has been suggested in the literature, that an observed decrease in expression of mitochondrial enzymes in skin samples of patients precedes a loss of intradermal nerve fibers, which can be observed (Soldevilla et al 2017). So if glucose really is transported into the axons and metabolized there, is it damaging to the mitochondria? Alternatively, is this change of mitochondrial morphology a

compensatory mechanism to reach higher efficiency? After all, ATP levels were unaltered at earlier time points. In an *in vitro* study cells under high glucose conditions increased reactive oxygen species (ROS) production and the mitochondria became fragmented, which lead to oxidative stress and eventually cell death (Yu et al 2008). Bas-Orth and colleagues reported for a study conducted in the CNS, a mechanism of a neuronal switch to glycolysis away from oxidative phosphorylation (Warburg Effect like) to protect axons from stress under synaptic activity (Bas-Orth et al 2017). Is a chronic upregulation of mitochondrial metabolism in axons slowly killing the axons in *Pmp22*^{tg} fibers? To test for the question we aimed to prevent excess glucose uptake to the neurons be ablating GLUT1 or 3 in SC or neurons respectively.

3.2.5. Does a deficiency of GLUT1 in Schwann cells have an impact on the CMT1A phenotype?

In this study, GLUT1 was removed from SCs (with *Dhh* cre driver line) in *Pmp22*^{tg} animals. As presented here the SC-KO by itself had no effects on Grip strength behavior (**Figure 17**) or electrophysiology measurements (**Figure 18**). No change in expression of other transporter tested was reported (**Figure 16**) and only slight alterations were detectable in histology analysis conducted (**Figure 19**). These findings are in accordance with a study by Babetto and colleagues, stating no abnormalities in a conditional KO of GLUT1 using *P0* cre in the absence of an additional challenge (Babetto et al 2020). Even though GLUT3 expression has not been observed to be upregulated in compensation in the here presented data, the expression in SCs, as reported in literature, could be enough for import under healthy conditions. Only under challenge, e.g. injury, the lack of transporter becomes apparent (Babetto et al 2020). Here, a SC-KO in *Pmp22*^{tg} did not affect the already existing phenotype. No amelioration, nor an additive effect could be shown. This supports the notion of non-diabetic SCs or at least does not provide evidence, that SCs are stressed by an accumulation of glucose. However, it also did not worsen the phenotype of *Pmp22*^{tg} animals. Are the axons not supplied via the Schwann cells anyway? Would a transport at the nodes of Ranvier via GLUT3 present there be sufficient to supply the axon with energy? Are other transporter involved? Especially for non-myelinating SCs is has been proposed, that metabolites are transferred from one SC to adjacent one by gap junctions (Véga et al 2003).

The findings in this study tend towards the hypothesis of axons first supporting itself, over time and with challenge, this compensatory state is not sufficient. There are speculations for CNS and PNS that the upkeep of resting potential and action potential generation are not the most energy consuming for an axon to supply. Much rather the transport of organelles is hypothesized to consume large amounts (Deck et al 2020, Harris & Attwell 2012). Deck and colleagues showed that depletion of lactate in Schwann cells could be compensated by an increase of glucose in axons. However, this does not support ATP pools as sufficiently. In nerve injury studies observations were made that Schwann cells undergo a glycolytic switch to support the axon with more lactate under this challenge (Babetto et al 2020). When MCT are removed from SCs, axons first adapt by an upregulation of glycolysis mRNA in neuronal cell bodies of the ventral horn, however over time animals nonetheless, exhibit a loss of functional NMJs, indicating axonal failure (Bouçanova & Chrast 2020). A compromised axo-glial coupling seems to be compensated by axons with upregulating their own glucose metabolism machinery. However, over time and with added challenges, this compensatory mechanism fails to support the axonal function leading to axonal degeneration. To this end, investigations of axonal glucose transport in *Pmp22*^{tg} animals is of high interest.

3.2.6. A putative role of the polyol pathway in CMT1A pathology

One of the most striking alterations in this study, as already mentioned, is the polyol pathway. As shown in **Figure 5** this downregulation of the pathway, including the key enzyme on mRNA level, is an effect that is present early on. The WT animals show an upregulation of expression between P6 and P18. *Pmp22*^{tg} rats fail to do so. Expression of the enzyme shows a faint induction of expression but until 16W is not comparable to expression of WT animals. This alteration at P18 precedes many of the described alterations, making it a candidate for interference. The aldose reductase the key regulatory enzyme of the polyol pathway is described to be expressed in SCs of animal models in dogs and rats (Kasajima et al 2002, Kern & Engerman 1982, Ludvigson & Sorenson 1980). Aldose reductase reacts *in vitro* to high glucose and osmotic pressure by increase mRNA amounts (Maekawa et al 2001), a mechanism playing a role in pathology of diabetes. Under normal conditions, it is reported, that 3% of all glucose consumed by cells in funneled into the polyol pathway (Morrison et al 1970). Under hyperglycemic conditions, like diabetes, it has been described to be up to 30% (González et al 1984). Just recently, the pathway has been implicated to play a role in

glucose sensing of cells via *Mondo* pathway in drosophila (Sano et al 2020). In mammals, the homologue MondoA/ChrREBP has been observed to be a major pathway in glucose sensing of cell (Havula & Hietakangas 2012). Up to now, the precise link has not been evaluated in mammals. If Schwann cells upregulate the pathway towards the end of myelination, it is possible, that SCs as well use this axis of polyol pathway and MondoA/ChrREBP to sense glucose concentrations to regulate metabolism accordingly. If that is the case, this feedback mechanism is lacking in *Pmp22^{tg}* animals. The polyol pathway is heavily implicated in diabetes to be a contributing mechanism in pathophysiology. In peripheral neurodegenerative diseases, a rare subtype of axonal CMT2 has been recently reported to be caused by a missense mutation in *SORD* the gene encoding for sorbitol dehydrogenase the second step of the pathway. This mutations leads to a non-functioning enzyme, which accumulated sorbitol. Patients experience an axonal form of CMT with lower limb muscle weakness. In drosophila, this missense mutation lead to a neurodegenerative phenotype, which could be rescued by aldose reductase inhibitors (Cortese et al 2020). In the here mentioned rat model, animals experience a downregulation of the pathway. In a therapy study by Prukop and colleagues conducted in the same model, animals were treated with a combination of baclofen, naltrexone and sorbitol. This treatment lead to a rescue of grip strength, increased CMAP and a rescue of functioning NMJs, with a possible involvement of axonal mitochondria discussed (Prukop et al 2019, Prukop et al 2020). The here discussed evidence suggests that the polyol pathway activity is necessary to be fine-tuned in peripheral neuropathies. A possible link could be cJun expression, which is increased in *Pmp22^{tg}* mice (Fledrich et al 2014). In mice, *cJun* inhibits expression of *Nrf2*/*TonEBP* which in turn activates expression of *Akr1b3*, a gene expressing aldose reductase in mice (Nishinaka et al 2019). In normal development, *cJun* is downregulated, when Schwann cells become more mature. The persistent high levels of *cJun* could prevent the upregulation of expression of polyol pathway, leading to a lack in sensing glucose and lack of upregulation of glucose metabolism genes. The question is how such a dysregulation also affects the axo-glial coupling. A glial cell with no metabolic homeostasis may not be able to support the underlying axon according to its needs.

4. Identifying novel circulating disease marker in blood of CMT1A patients and *Pmp22^{tg}* rats

4.1. Results

4.1.1. Study design

CMT1A is a slowly progressive disease with a high disease variability among patients. The causes for the high diversity remain unknown and in day-to-day patient care makes it challenging to counsel patients. The slowly progressive nature makes clinical trials and appropriate recruitment numbers a demanding task, highlighting the need to search for highly sensitive surrogate disease makers. A translational screen was performed using *Pmp22* overexpressing rats (*Pmp22^{tg}*) and patient material. Therefore, out of 150 animals 4 or 5 animals out of the two extremes for mild and severe disease phenotypes were selected, respectively (**Figure 21**). At 6W, blood was sampled and the disease progression was monitored every four weeks until the age of 18W, when blood was sampled again. The 6W time point was used to conduct an RNA screen (Nirmal Kannaiyan and Moritz Rossner, LMU Munich).

Patients were recruited within the CMT-NET network. In total, 139 CMT1A patients (male and female) were seen three times over the course of two years. Patients were examined thoroughly and CMTNSv2 as a disease score was determined (Examinations done within CMT-NET Study Centers) and blood samples were obtained. Again, the first time point was used to conduct an RNAseq screen (**Figure 21**). Out of the male cohort 4 mildly affected patients (age: 30-45 years; CMTNSv2: 3-11) and 4 severely affected patients (age: 35-47 years; CMTNSv2: 20-27) were selected for sequencing.

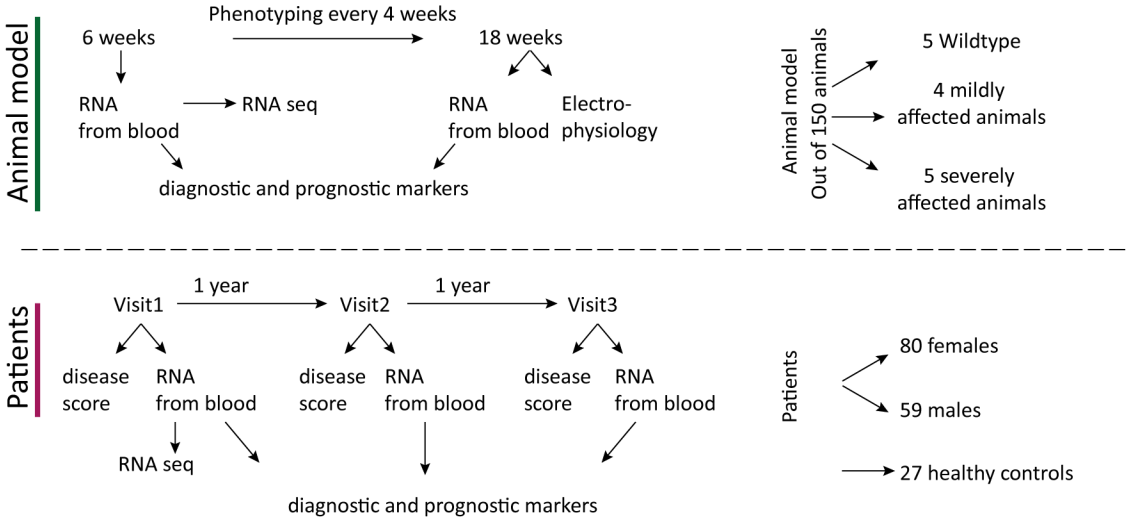

Figure 21: Study design to identify circulating disease marker in CMT1A patients and *Pmp22^{tg}* rats. Upper panel: *Pmp22^{tg}* rats were phenotyped every four weeks starting at the age of six weeks until 18 weeks. At six weeks, based on the phenotype, 4 mildly and 5 severely affected animals were selected from a group of 150 animals. 5 WT age matched animals were used as control animals. Blood was sampled at ages of 6 and 18W and electrophysiologic analysis was done at 18W. Blood samples at 6W were used for an RNAseq screen to identify disease marker. Lower panel: 80 female and 59 male CMT1A patients were recruited and examined over the course of two years in three visits. Each visit consisted of a detailed examination and blood sampling. 4 mildly and severely affected patients were selected to obtain an RNAseq data set using the blood sampled at visit 1. 27 healthy control patients were recruited for subsequent more detailed analysis steps(animals phenotyping by Stephanie Wernick; Patient examination by CMT-NET Study Centers, RNAseq screen by Nirmal Kannaiyan and Moritz Rossner, LMU Munich).

4.1.2. RNAseq analysis identifies several candidates overlapping in CMT1A patients and *Pmp22^{tg}* rats

As described above, blood samples of 4 mildly and 5 severely affected *Pmp22^{tg}* animals and 4 mildly and severely affected patients were selected from within the male CMT-NET CMT1A patient cohort to conduct an RNAseq screen in order to identify disease marker. As depicted in **Figure 22 A** and **B**, in the animal model as well as in the patient group significant differential expression of genes could be detected between mild and severe disease phenotypes.

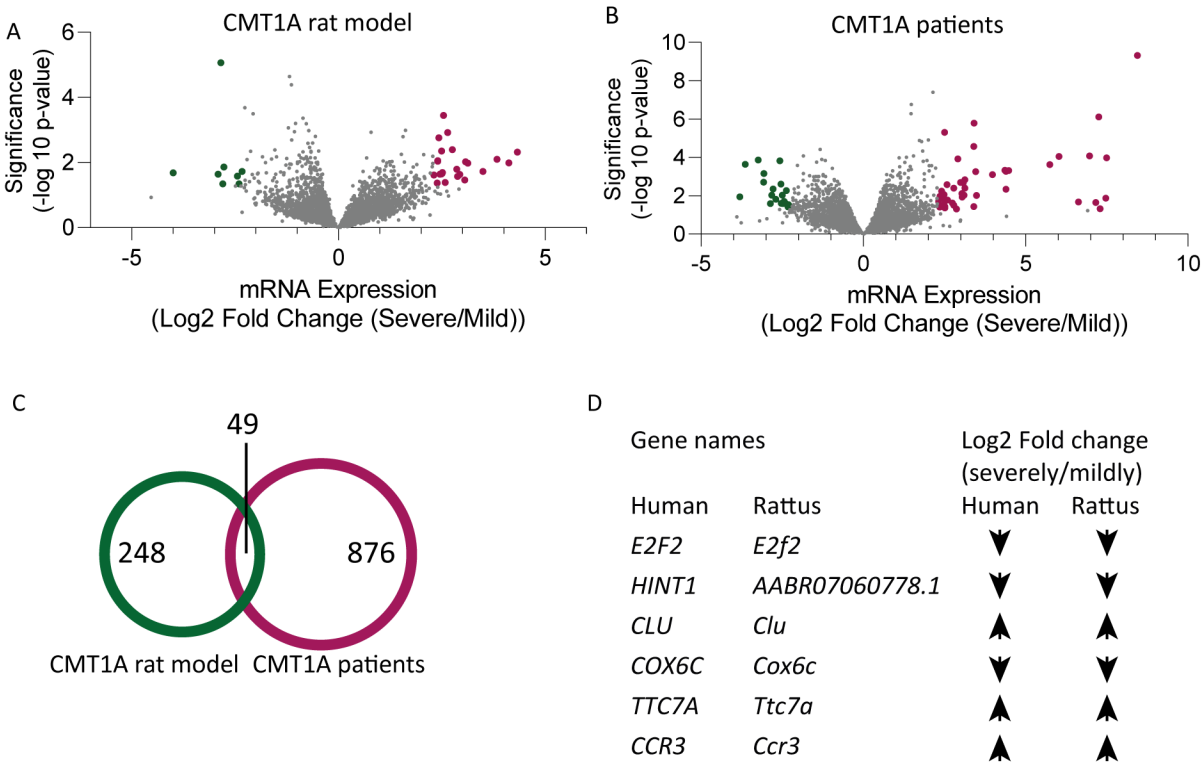

Figure 22: RNAseq screen for circulating disease markers in CMT1A patients and *Pmp22*^{tg} rats. An RNAseq screen was performed comparing 4 mild and 5 severe affected rats in expression levels in blood samples. Shown is a comparison of severe/mild with log2 fold change and –log10 p-value (A). In parallel, the same analysis was performed for an exemplary 4 mild and 4 severe affected male patients (B). 248 significantly differentially expressed genes were identified in the animal model, while 876 were identified in the patient group (C). 49 genes overlapped between the two analyses. Comparing the two data sets, a candidate list was selected based on direction of regulation between mild and severe for the animals and the patients (D). RNAseq analysis done by Nirmal Kannaiyan and Moritz Rossner (LMU Munich) Cut off: -log10 p-Value: 1.3; log2 fold change: -2.3 and 2.3; (Students T-test)

When comparing significantly regulated genes (249 for the animal model and 876 for patients), an overlap of 49 genes was identified (**Figure 22C**) by applying a cut off for significance level of p-value ≤0.05 only for the human dataset. The list of candidates was further investigated. To select genes for subsequent validation of mRNA expression in the entire cohort by qRT-PCR, only candidates with the same direction of change between animal and patient groups were taken into account. As an order of priority, significance and magnitude of change within the patient groups was applied. A list of top candidates is shown in **Figure 22 D**.

4.1.3. *COX6C/Cox6c* as a disease marker candidate in *Pmp22^{tg}* rats as well as CMT1A patients

As already mentioned qRT-PCR analysis was performed to verify expression levels in animals and the entire patient cohort at the time points 6W (for the animals) and visit (V) 1 (for patients). One candidate was *COX6C,* which is a nuclear encoded subunit of cytochrome C oxidase (COX) also known as complex IV of mitochondria (Dhar et al 2009, Grossman & Lomax 1997). For the animal model, the expression levels of *Cox6c* at 6W were correlated to the measured grip strength of each animal at that time point. As shown in **Figure 23A**, the expression correlated positively with the observed strength, suggesting the more gene is expressed the stronger the animals actually are. The expression at 6W was also positively correlated to the grip strength at 18W (**Figure 23B**). In conclusion, *Cox6c* expression levels may serve as diagnostic as well as prognostic disease marker in *Pmp22^{tg}* animals. As a first step for the patients cohort, the expression of *COX6C* was compared in CMT1A patients with healthy controls (**Figure 23C**). The expression in patient blood samples was significantly down regulated in comparison to healthy controls (Healthy: 1±0.32; CMT1A: 0.7±0.24; $p \leq 0.001$). Additionally, the expression was correlated to handgrip strength measurements from the corresponding examination. In agreement with the animal data, *COX6C* was higher expressed in patients with more handgrip strength (**Figure 23D**).

In conclusion, *Cox6c* and its homologue *COX6C* may serve as a possible surrogate disease marker in CMT1A patients and *Pmp22^{tg}* rats.

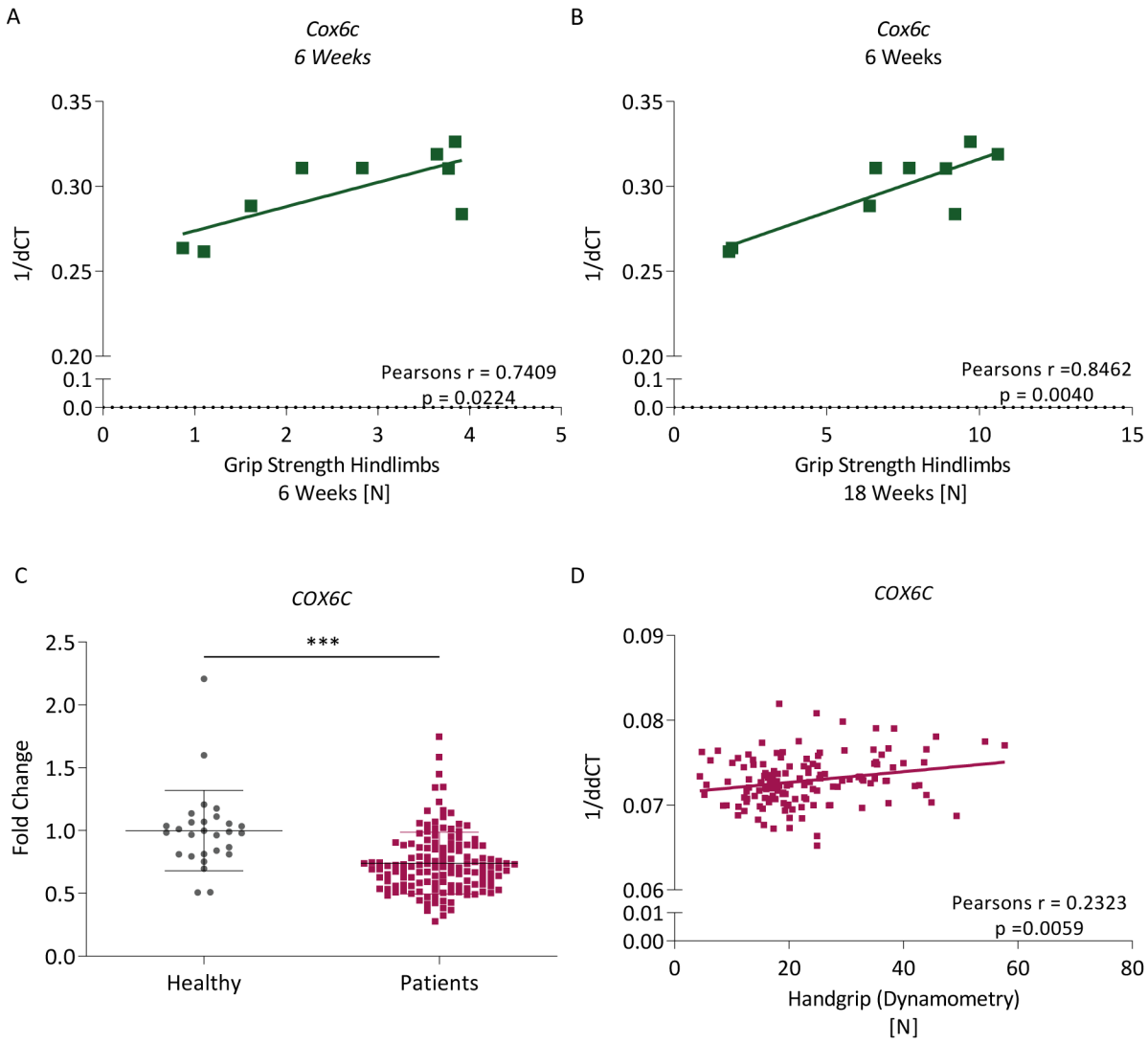

Figure 23: *Cox6c/COX6C* as a candidate for disease marker in CMT1A patients as well as *Pmp22*^{tg} rats. Expression of *Cox6c* at 6W correlates with grip strength of hind limbs at 6W (A) and 18W (B). *COX6C* is differentially expressed in blood samples of patients in comparison to healthy controls (C) and expression correlated with handgrip strength in patients (D). qRT-PCR was pipetted by Beate Veith (Mean ±SD; p-value ≤0.001 ***; Patients: n=137; Healthy controls: n=27; Pearson's Correlation)

4.2. Discussion

CMT1A is a dysmyelinating neuropathy caused by an overexpression of *PMP22* in Schwann cells (Raeymaekers et al 1991). Typical hallmarks observed in patients can be reproduced in animal models by inserting extra copies of the *Pmp22* gene (Fledrich et al 2012a, Sereda et al 1996). One characteristic is the slowly progressive nature of the degenerative phenotype (Rossor et al 2015). Additionally, high disease variability has been observed even among twins (Garcia et al 1995). The cause for the high variability, leading to a varying experience of disease burden in day-to-day life, remains unknown. It would be highly beneficial to predict disease progression, not only for patients themselves but also for determining most efficient treatment plans. The slow disease progression harbors difficulties in treatment implementation in clinical trials. Alterations in disease score are minimal over short periods of time requiring high patient numbers to reach statistical meaningful number (Rossor et al 2020). The prevalence of 10-28/100 000 (Pareyson et al 2017) makes this a challenging task. It is assumed that the insensitivity of known disease scores has masked successful treatment outcomes in the past (Fledrich et al 2012b, Rossor et al 2016). Therefore, the here presented study was designed to screen for sensitive surrogate markers in blood of CMT1A patients and *Pmp22*^{tg} rats in a translational approach.

4.2.1. The mitochondrial gene *COX6C* as a putative disease marker in CMT1A patients

Using representative samples of both extremes of disease severity in the animal model an RNAseq screen was performed for blood samples. In addition, analysis of mRNA expressions was done in representative mildly and severely affected patients from within a patient cohort of CMT-NET. In patients and in the animal model differential expression could be detected between mildly and severely affected individuals (**Figure 22 A** and **B**). Due to the small overlap between both datasets when applying stringent significance, cut offs were only applied for the human dataset. With these parameters, a list of 49 genes were found to be regulated in both data sets (**Figure 22 C**). This overlap already demonstrates the feasibility of this translational approach. As additional parameter, the direction of change was taken into account, leading to a list of prioritized candidates for further investigation (**Figure 22 D**). Most promising candidates were verified via mRNA expression by qRT-PCR analysis in the entire patient cohort (**Figure 23**). One candidate analyzed in this study was *COX6C,* encoding for one of the subunits of cytochrome C oxidase (COX) also known as

complex IV of mitochondria (Dhar et al 2009, Grossman & Lomax 1997). COX is assumed to have major impact on regulating respiratory activity of mitochondria in tissues, which can be altered drastically by disturbance of one of the subunits, e.g. *COX6C* (Srinivasan & Avadhani 2012, Villani & Attardi 2000, Yang et al 2018).

The homologue of rats *Cox6c* correlated in expression at 6W with hind limb grip strength at 6W and 18W. In the human cohort, *COX6C* was differentially regulated in CMT1A patients in comparison to healthy controls and correlated with grip strength in CMT1A patients. This finding suggests COX6C/Cox6C as a putative candidate for diagnostic as well as prognostic disease marker.

Additional investigations for expression over time have to be conducted to verify feasibility for clinical use. To combine other candidates into a cluster of markers would produce a more robust surrogate disease marker that should be correlated to a broad set of clinical outcome measures, beyond handgrip strength itself. Finally, findings need to be validated in an independent patient cohort to demonstrate capability as outcome measure for clinical trials.

4.2.2. Suitability of blood biomarkers as surrogate markers of CMT1A disease

It remains unknown, how blood expression of candidates relates to pathology in peripheral nerves of patients. It has been demonstrated that expression of a cluster of five genes in skin biopsies of patients correlates with disease severity. Additionally, the same expression patterns have been reported in *Pmp22^{tg}* rats and significant regulation of expression was shown for nervous tissue of the animals as well (Fledrich et al 2017, Fledrich et al 2012a, Gautier et al 2020). In plasma of patients, neurofilament light chain was detected as a disease marker representative for axonal damage (Sandelius et al 2018). Recently, also TMPRSS5 has been shown to be changed on protein level in CMT1A patients. Nonetheless, expression does not correlate with disease severity (Wang et al 2020). In a third study, metabolites in plasma of CMT1A patients have been significantly correlated to disease phenotype (Soldevilla et al 2017). Thus, molecular markers from plasma samples seem to be able to serve as surrogate disease markers. A factor arguing strongly in favor of plasma samples is accessibility. Blood sampling is low in costs and can easily be integrated into day-to-day outpatient care with minimal invasiveness for the individual. Analyzing mRNA expression is especially feasible as levels can be preserved in routine storage conditions, as with the right kits, storage temperatures are not demanding to maintain.

Seeing the implications of *COX6C* as a putative disease marker in blood of CMT1A patients, in context of in Chapter 3.1.5 presented results towards changes in mitochondrial energy metabolism highlight the importance of mitochondrial alteration in disease pathology. As already suggested in a preclinical therapy study, PXT3003 treatment ameliorates disease phenotype of CMT1A rats by decreasing mitochondrial alterations (Prukop et al 2019). Further, early loss of enzymatic machinery of mitochondria has been suggested in skin biopsies of CMT1A patients (Soldevilla et al 2017). This strengthens the involvement of mitochondrial metabolism in CMT1A pathology and further research may provide new treatment strategies.

In conclusion, this data can open the path to new easily accessible disease markers useful for the optimization of current standard patient care based on disease severity at hand. Further, disease markers open up new possibilities for clinical trials with more sensitive surrogate readouts, past the currently used limited clinical readouts due to slowly progressive disease course.

5. Conclusions

Failed axonal support by glia cells has been proposed as a common feature in peripheral neuropathies. Therefore, it is of great interest to identify players of this complex relationship. Axonal loss is correlated to disease severity in CMT1A patients. As this histological hallmark is an irreversible one, it is of great interest to identify key players targetable with novel treatments that may be able to prevent axonal loss and the disease course. We therefore aimed to decipher the changed dynamic of metabolic support from glia towards fibers in nerves of *Pmp22^{tg}* animals.

In this study, it has been shown that *Pmp22^{tg}* animals acquire an alteration in metabolite profile in peripheral nerves in the final stages of development. Despite enriched glucose levels, no upregulation of glycolysis in Schwann cells was detected. Additionally, Schwann cells do not seem to increase their glycogen storages and do not react with a severe increase of polyol pathway activity as would be expected of Schwann cells under hyperglycemic conditions e.g. in diabetes.

FLIM measurements demonstrated reduced ATP pools in axons of old *Pmp22^{tg}* animals and less oxidized mitochondria were observed. Morphologically axonal mitochondria showed rather fragmented organelles and an increase of mitochondrial protein in nerve lysates was shown for MT-CO1. Additionally, protein expression of Hexokinase1, representative for glucose metabolism enzymes was increased in whole nerve lysates, and was localized to axons and SCs in *Pmp22^{tg}* animals.

We hypothesize, that glucose reaches the axonal compartment in peripheral nerves of CMT1A animals and is able to compensate for missing metabolic support from the glia cell. With time, it is possible that the increase in glucose in the axon does lead to deleterious effects in the fibers, leading to axonal degeneration, loss of NMJs and in the end reduced muscle strength.

In the translational part of this study, evidence was presented for a putative surrogate disease marker in blood of CMT1A rats and patients. Expression of *COX6C* correlated with handgrip strength in the German CMT-NET patient cohort, implicating the involvement of mitochondrial alterations in disease pathology.

A putative mechanistic link we suggest is that a persistent expression of *cJun* in late developmental stages prevents the Schwann cells from upregulating activity of the

polyol pathway to WT levels. The polyol pathway has been implicated in sensing glucose to upregulate expression of corresponding enzymes.

Several investigations may be of interest to prove the hypothesis in the future:

1) A precise characterization of metabolites in the glial and axonal compartment separately would enable a deeper understanding of the dynamics present in peripheral nerves of *Pmp22*^{tg} animals. In the past, many sensors for different metabolites have been engineered which can be expressed by AAVs. AAVs could be injected into the ventral horn or DRGs to target neuronal cell bodies projecting into the periphery and as a second injection site to target Schwann cells into the epineurium enwrapping the sciatic nerve. With this approach, one could compare the abundance of glucose, lactate and ATP in the two mentioned compartments.

2) By utilizing already mentioned *Slc2a3* floxed animals, the role of glucose transport into the axons of *Pmp22*^{tg} animals could be deciphered. Due to a lack of appropriate *cre* driver lines, one approach could be the injection of AAVs expressing *cre* recombinase into the ventral horn to target motor neuron cell bodies. A KO of GLUT3 in *Pmp22*^{tg} should speed up the disease phenotype if the proposed theory holds true or shield the axon from glucose overload.

3) To test the hypothesis of an axis of *cJun* - *Akr1b3* - MondoA/ChrREBP - glucose enzymes it would be of interest to utilize DRG co-cultures. By interfering with siRNAs or overexpression at different steps of the proposed axis, one could check the feasibility of this mechanistic explanation.

In conclusion, evidence for changes in SC metabolism regarding glucose metabolism have been presented. SCs seem to not support CMT1A axons metabolically, leaving the axon to fend for itself. Primarily beneficial compensational changes could lead to deleterious effects with time driving the axonal degenerative pathogenesis.

6. Materials and Methods

6.1. Materials

6.1.1. Cell culture

Ascorbic acid	SIGMA
Bovine pituitary extract (BPE)	Th. Geyer
Collagenase II	Worthington
Cytosine β-D-arabinofuranoside hydrochloride (AraC)	SIGMA
DMEM(glucose 4.5g/L, pyruvate(-), L-glutamine (+))	GIBCO
Fetal calf serum (FCS)	Hyclone
Forskolin	Sigma
GlutaMax^{Tm}	GIBCO
MEM (+L-glutamin, Earle's salts)	GIBCO/Invitrogen
NGF (Neuronal growth factor) 2.5S	Alomone Labs
Pen/Strep	Lonza
Poly-L-Lysine (PLL)	SIGMA
RLT buffer	Qiagen
Trypsin/EDTA	Lonza
DB-cAMP	Biolog

6.1.2. DNA

dNTP Mix	Boehringer
GelRed Nucleic acid	Biotium
Genomic DNA isolation kit for tissue and cells	Nexttec
GenRuler 100bp DNA ladder	Thermo Fisher Scientific
GenRuler 1kB DNA ladder	Thermo Fisher Scientific
GoTaq G2 Polymerase kit	Promega
Proteinase K	Roth

Primer ID	*Sequence (5'-3')*
2016	GCCTTCAAACTGTCCATCTC
2201	CCAGAAAGCCAGGGAACTC
2202	GACAAACCCCAGACAGTTG
2444	GTAGCTTTCCCCACCACAGA
4858	CGCTGAACTTGTGGCCGTTTACG

4859	TCTGAGTGGCAAAGGACCTTAGG
7315	CCCAGCCCTTTTATTACCAC
10967	CAGCCCGGACCGACGATGAA
10967	CAGCCCGGACCGACGATGAA
11906	TCAGGATATCTATCTGATTCTC
11907	AAGCTCATGGAGCACAAAACC
15793	CCTGCGGAGATGCCCAATTG
23312	CTGGATAGGAGTGAGAACAGC
23313	ATGAATCCATTGAGTGACAGG
30901	CAGACTGCCGCGGCGTAGATG
30951	CGGCGTGGACGAGGACACAG
37740	CTGTGAGTTCCTGAGACCCTG
37741	CCCAGGCAAGGAAGTAGTTC
37768	CCAACTTAAACACAATTGCCTGGTG
37769	GGCTCACAATTACCCATAATGA
38311	TGAATCCCTCATCTGCCTGC
38548	GGGCTTGATGAACACAACCAC
38549	CTATGGCAAAGAGGCTACTTCC

6.1.3. RNA

dNTP Mix	Boehringer
GoTaq qPCR Master Mix	Promega
Random 9mer (NNNNNNNNN)	AGCT-Lab MPI EM
Oligo dT (TTTTTTTTTTTTTTTTTTTTTTTVN)	AGCT-Lab MPI EM
Paxgene Blood RNA Kit	Qiagen
Paxgene Tubes	Qiagen
QIAzol Lysis Reagent	Qiagen
RNeasy Mini Kit	Qiagen
SuperScript III Reverse Transcriptase Kit	Invitrogen

Target	*Sequence (5'-3')*	
	forward	reverse
18s	GCTCTAGAATTACCACAGTTATCCAA	AAATCAGTTATGGTTCCTTTGGTC
Aco2	CACAAAATGGCGCCTTACA	GACAGAGGCCACATGGTACTG
Akr1b1	AGCCATCTGGAACTCAACAAC	TCACAGCCTCGGTCACCT
Aldoa	CTTTCACTGCACCACAGGAA	CTACAATTCGGTGAGCGATG

Aldoc	TGTTGCTAACCAGACCAAAGTG	TATGAGTGGGGCATGGTGA
Atp5f1a	ATGGTATTGCGCGAGTGC	CCAAGTTCAGGGACATACCC
Cox4i1	TCACTGCGCTCGTTCTGAT	CGATCGAAAGTATGAGGGATG
Cycpha	CACAAACGGTTCCCAGTTTT	TTCCCAAAGACCACATGCTT
G6pd	GGAAGAGTTGTACCAGGGTGA	GATCTTCTTCTTGGCCAGGTC
Gapdh	GGCTCACAATTACCCATAATGA	ATGGCCCCTCTGGAAAGCT
Gys1	CGTGCGCAAACAGCTATG	GAGCTTCCTCCCAAATTTCTC
Hk1	GTGGACGGGACGCTCTAC	TTCACTGTTTGGTGCATGATT
Hk2	ACTCCGGATGGGACAGAAC	CACACGGAAGTTGGTTCCTC
Ldha	CCATTGGCCTCTCTGTGG	GGAAGACATCCTCATTGATTCC
Mdh2	TGACCTGTTCAACACCAACG	GATGGGGATGGTGGAGTTC
mtAtp6	TAAGCATAGCCATCCCCCTA	TTAGTTTGTGTCGGAAGCCTAGA
mtCo1	TGTAGTAGCTCACTTCCACTATGTCTT	GGACGAAGCCAGCTATGATG
mtCytb	CCCTAGTACTATTCTTCCCAGACCT	AGGGGGTTAGCGGGTGTAT
mtNd2	CCATTCTCGCAATTTCATCA	TTTCGTGTTTGGGTCTGGTT
Nduv2	TGAACTCAGAGCTGGGAAAGT	GCTGGCTCACAACAGAAGC
Pfkm	AGATCGTAGACGCCATCACC	GGCCCATCACTTCTAACACAA
Pkm2	AAGGGGGACTACCCTCTGG	CCTCGAATAGCTGCAAGTGG
Pygb	AGGGTCCTGTATCCCAATGA	CAGCCACCACAAAGTACTCCT
Rplp0	GATGCCCAGGGAAGACAG	ACAATGAAGCATTTTGGATAATCA
mouse		
Rplp0 rat	GATGCCCAGGGAAGACAG	ACAATGAAGCATTTTGGATAATCA
Sdha	CAGTTCCACCCCACAGGTA	TCTCCACGACACCCTTCTG
Slc16a1	ATGCTGCCCTGTCCTCCT	CCACAAGCCCAGTACGTGTAT
Slc16a7	TGGAGTGTTGCCCAGTTCTT	TCCCACTGGCTATGTACAGGT
Slc2a1	GACCCTGCACCTCATTGG	GATGCTCAGATAGGACATCCAAG
Slc2a3	TTTGCCCTGAGAGTCCAAGA	ACAAGCGCTGCAGGATCT
mouse		
Slc2a3 rat	TCTCTGGGATCAATGCTGTG	CCAATCGTGGCATAGATGG
Uqcr10	GTCAGCTGTCAGCCTGGAG	TGCTCCCTCTTGTACCCTGT
COX6C	CCCGCATCTACTCTCTCACG	CTGTCCTTGATACGTATGCTAACC
human		
Cox6c rat	ATATTGTTGGCGCATTCGTT	GTTCAGCCACGCCAAACT
18s rat	AAATCAGTTATGGTTCCTTTGGTC	GCTCTAGAATTACCACAGTTATCCAA

Actb rat	CGCTCAGGAGGAGCAATG	TGACAGGATGCAGAAGGAGA
ACTB human	CCAACCGCGAGAAGATGA	CCAGAGGCGTACAGGGATAG
B2M human	TTCTGGCCTGGAGGCTATC	TCAGGAAATTTGACTTTCCATTC
CYCPHA human	ATGCTGGACCCAACACAAAT	TCTTTCACTTTGCCAAACACC
RPLP0 human	TCTACAACCCTGAAGTGCTTGAT	CAATCTGCAGACAGACACTGG

6.1.4. Protein

Acrylamid M-Bis (30% w/V) solution 29/1	GERBU
FastGreen FCF	Serva
PageRuler Plus Prestained Protein ladder	Thermo Fisher Scientific
Phosphatase inhibitor PhosStop	Roche
Polyvinylidene diuoride (PVDF) blotting membrane Hybond P pore size 0.45µm	Amersham Hybond Bioscience
Protease Inhibitor cOmpete tablets EASY	Roche
PVDF membrane (Immobilon-FL 0.45µm)	Merck Milipore
SuperSignal West Atto	Thermo Fisher Scientific
Western Lightning Plus ECL Enhanced chemiluminescence	Perkin Elmer

Target	*Company*	*Species*	*Dilution*
Primary Antibody			
GLUT1	Custom Made (Kathrin Kusch) (Berghoff et al 2017)	Rabbit	1:10 000
MCT1	Custom Made (Kathrin Kusch) (Stumpf et al 2019)	Rabbit	1:5000
GLUT3	Abcam (ab191071)	rabbit	1:1000
Hexokinase1	Cell signaling (C35C4)	rabbit	1:1000
MT-CO1	Abcam (ab14705)	Mouse	1:2500

Secondary Antibody			
Mouse-HRP	Dianova	Goat	1:5000
Rabbit-HRP	Dianova	Goat	1:5000

6.1.5. EM

Copper grids	Gilder Grids
DDSA	Serva
DMP-30	Serva
Eukitt	Kindler/Science Services
Formvar	Plano
Glutaraledhyde	Electron Microscopy Science
Glycidether 100	Serva
MNA	Serva
Osmium tetraoxide	Science Services
UranylLess	Science Services
Uranylacetate	Merck
Methylcellulose Uranylacetate	Serva

Target	*Company*	*Species*	*Dilution*
Primary Antibody			
GLUT1	Self made by Kathrin Kusch (Berghoff et al 2017)	Rabbit	1:200
MCT1	Self made by Kathrin Kusch (Stumpf et al 2019)	Rabbit	1:100
Secondary Antibody			
Rabbit Protein A Gold 10nm	CMC Utrecht		1:50

6.1.6. Histology and staining

Bovine serum albumin (BSA)	BioMol
Coverslips #1.5 (different sizes)	Thermo Fisher Scientific Menzel Gläser
Goat serum	Gibco
Histobond Slides	Marienfeld

Horse serum	Gibco
Mowiol 4-88	Roth
Paraformaldehyde	Serva
Superfrost Plus slides	Thermo Scientific Menzel-Gläser

Target	*Company*	*Species*	*Dilution*	
Primary Antibodies				
GLUT1	Kathrin Kusch self made (Berghoff et al 2017)	rabbit	1:100	STED, Immunofluorescence
Hexokinase1	Cell signaling (C35C4)	rabbit	1:50	Immunofluorescence
MAG (clone 513)	Chemicon	mouse	1:50	STED, Immunofluorescence
TUJ	Covance	mouse	1:200	Immunofluorescence
Secondary Antibodies				
Alexa 488	Anti mouse (Invitrogen)	donkey	1:1000	Immunofluorescence
Alexa 568	Anti rabbit (Invitrogen)	donkey	1:1000	Immunofluorescence
Starred	Anti rabbit (Abberior)	donkey	1:30	STED
Alexa 594	Anti mouse (Invitrogen)	donkey	1:100	STED

6.1.7. 2-NBDG tracing

2-NBDG	Cayman Chemical Company

6.1.8. FLIM analysis

Sea Plaque Agarose (low melting temperature agarose)	Lonza
Glucose	Fluka BioChemika
Sucrose	Milipore

6.1.9. roGFP2

Diamide	Sigma
Dithiothreitol (DTT)	Biomol
N-Ethylmaleimide (NEM)	Sigma

6.2. Methods

6.2.1. Animals

Animals were bred and kept in the animal facility at the MPI for experimental Medicine in Göttingen on a 12/12h dark-light cycle with access to water and food ad libitum and were treated in accordance with the German Protection of Animals Act (TSchG §4 Abs. 3), with the guidelines for the welfare of experimental animals issued by the European Communities Council Directive 2010/63/EU as well as the regulation of the institutional 'Tierschutzkommission' and the local authorities (LAVES Niedersachsen). The experiments presented here were all applied for under the license number 16/2200, 17/2460 and 18/2938. For this study, two animal models for CMT1A were used. On the one hand, the 'CMT rat' (SD-Tg(*Pmp22*)^{Kan} (RDG ID: 2312447)) a Sprague Dawley rat harboring additional copies of the murine *Pmp22* gene (Sereda et al 1996) was bred heterozygously for this study. As a mouse model of the disease, the C61 animal model was used harboring additional copies of the human gene (MGI: 4819405 (Huxley et al 1998)). The mice were bred heterozygously as well. The mouse model was further crossed to a mouse expressing a transgene for the ATP FRET sensor AT1.03^{YEMK}, under the *Thy1* Promoter (MGI:5882597 (Trevisiol et al 2017)) for ATP measurements in axons. For redox status measurements the C61 mouse model was crossed to *Thy1*-mito-*Grx1*-roGFP2 animals (Breckwoldt et al 2014) (provided by Thomas Misgeld). Both sensors were kept heterozygously as well. Mice expressing a glucose sensor (CNPGLC) or a lactate sensor (CNPLAC) under the *Cnp* promoter were generated by Andrea Trevisiol and Johannes Hirrlinger at the MPI-EM. For a knockout of *Slc2a1* in SC, we used animals with flox sites flanking exon 3-8 of the gene ((Young et al 2011) provided by Dale Abel) and bred them with animals expressing the cre recombinase under the *Dhh* promoter (MGI:4359600 (Jaegle et al 2003)). For a knockout of *Slc2a3,* we used animals with flox sites flanking exon 7 of the gene ((Fidler et al 2017) provided by Dale Abel) and bred them with animals expressing cre recombinase under the *Olig2* promoter (Dessaud et al 2007). All mice used in this study were on a C57Bl6 background. As controls age matched wild types were used. Whenever possible the wild type littermates were corresponding controls. For cre/flox mediated Ko models, fl/fl animals negative for the cre allele were used as controls.

6.2.1.1. Dissection

Animals were sacrificed, unless stated otherwise, by cervical dislocation for mice and by CO_2 inhalation and consecutive cervical dislocation for rats. Biopsies of the tail (mice) or ear (rats) were used for genotyping. For protein or RNA analysis the peripheral nerves were transferred into ice cold PBS and the epineurium was removed. The samples were snap frozen and stored at -80°C until further processing. For histological analysis, the tissue was transferred onto a Whatman paper and stored in the corresponding fixative. For teased fibers the sciatic nerves were transferred into ice cold PBS and the epineurium was removed. The nerve tissue was split into smaller parts longitudinal along the nerve. One of these smaller parts was transferred onto superfrosted slides in a small drop of PBS and the axons were separated carefully with fine forceps so areas of single axons were achieved. The samples were air dried and stored at -20°C until staining. For RNA analysis of blood, blood was collected and transferred to a Pax Gene blood tube.

6.2.1.2. Behavior

For the characterization of SC-KO of GLUT1, animals were weight at 12W and 18W and a grip strength analysis was performed for forelimbs and hind limbs. A newton meter from Alluris (FMI210B2) with a T-Bar attached was used. For forelimb measurements, the mouse was broad close to the bar until it hold on tightly with both paws. Then, the mouse was pulled horizontally away from the bar by the tail until it let go and the force measured was recorded. This was repeated five times per animal. After a break, the hind limb measurement was performed. The front paws of the animal were supported while the hind limbs were broad closer to the bar so the animal could hold onto the bar with both paws. The animal was then pulled away from the bar horizontally by the tail, making sure the forelimbs do not touch the bar. The force was recorded and the measurement repeated 5 times. For analysis a nested 1way ANOVA was performed with GraphPad Prism.

For the phenotyping of *Pnp22*^{tg} rats for the biomarker analysis, behavior of rats was analyzed every 4 weeks. Experiments were performed by Stephanie Wernick. A battery of tests was performed as described in (Prukop et al 2019, Prukop et al 2020). The only data shown here are grip strength analysis of hind limbs, done as described above.

6.2.1.3. Electrophysiology

Electrophysiology was performed by Theresa Kungl. In short, a Ketamine (100mg/kg)/ Xylazine(20mg/kg) injection i.p. was used for anesthesia and success was checked by the absence of toe pinch reflexes. Afterwards, motor electrophysiological measurements on the sciatic/ tibial nerve were performed. Stimulation needle electrodes were applied subcutaneously close to the sciatic notch (proximal stimulation) and in close proximity to the ankle (distal stimulation). For recording of the signals, electrodes were inserted in the small muscle on the plantar surface (**Figure 24**).

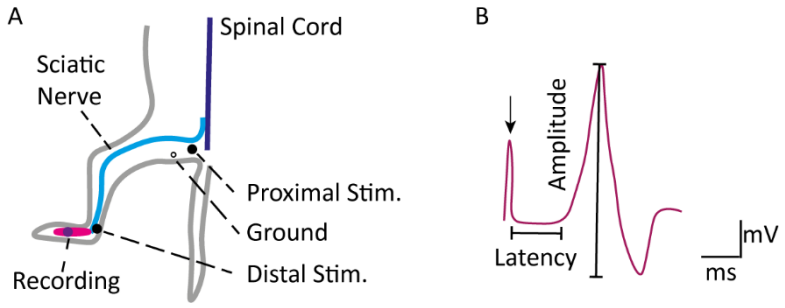

Figure 24: Schematic representation of electrophysiological measurements. (A) Placement of electrodes is shown. Stimulation electrodes (black dots) are placed close to the sciatic notch (proximal) and close to the ankle (distal). Recording by a pair of electrodes (purple dot) from the small muscle on the plantar surface. Grounding electrode is displayed as gray circle. (B) Typical CMAP recorded from motoric signals. Stimulus is marked with an arrow. Latency and Amplitude are measured from the signal.

After proximal and distal supramaximal stimulation, the compound muscle action potential (CMAP) was recorded. The NCV was calculated as follows:

$$NCV[\frac{m}{s}] = \frac{distance\ between\ stimulation\ sites\ [m]}{difference\ of\ latencies\ [s]}$$

Additionally, repetitive stimulations were performed. Therefore, bursts of 10 stimuli at frequencies of 3 Hz, 10 Hz and 50 Hz were applied with a supramaximal stimulation of 3 mA (only 50Hz measurement shown). The decrement between first and last CMAP was calculated to assess exhaustion of the given frequency.

6.2.1.4. Blood glucose content

Blood was taken from the tip of the tail of rats and content was measured using Freestyle Precision strips (Abbott).

6.2.2. Patients CMT-NET cohort

The study was positively voted by Ethics Committee of the University Medical Center Göttingen (UMG) under application number 31/2/16 on the 28th of July 2016 and amended on the 22nd of May 2018. Patients were recruited and examined within the German CMT-NET. (https://www.cmt-net.de/). In short, CMTSv2, ONLS, 6 min walk test, 10 meter walk and nine hole peg test, Maximal voluntary isometric contraction (MVIC (Fist Grip, three point Grip, Foot dorsal flexion, foot plantar flexion)) were measured according to published procedure (Mannil et al 2014, Murphy et al 2011). Patients were seen three times over the course of two years and blood samples were taken, directly transferring blood into PaxGene tubes. Examinations were done by the study centers of CMT-NET.

6.2.3. Cell culture

6.2.3.1. Primary Schwann cell culture

Schwann cell purification from Sciatic nerves of neonatal rats was adapted from Brockes and colleagues (Brockes et al 1979). P2-P4 rats were sacrificed by decapitation and sciatic nerves were removed and the epineurium was removed in DMEM. The nervous tissue was digested in trypsin (2.5mg/mL in PBS) and collagenase (800U/mL) at 37°C and 5% CO_2 for one hour. The nerves were triturated by passing them through pipette tips. Digestion was stopped with FCS and the cells were spun down with a centrifuge. The pellet was resuspended and the cells were plated in DMEM and 10% FCS onto PLL coated dishes. The next day cells were switched to selection medium for 72 hours. After that, cells were kept in expansion medium until experiments. All cells can be passaged until passage 4. The cells were kept in an incubator at 37°C and 5% CO_2.

DMEM:	+ Pen/Strep (100U/mL)
	+GlutaMax
	In DMEM high glucose

Selection medium:	10% [v/v]	FCS
	10µM	AraC
	In DMEM	

Expansion medium:	10% [v/v]	FCS
	4µM	Forskolin
	100µg/mL	BPE
	In DMEM	

Stimulation medium:	2% [v/v]	FCS
	1mM	DB-cAMP
	In DMEM	

PLL coating: cover dish with 100µg/mL PLL in water and incubate for one hour at 37°C; wash with sterile water

6.2.3.2. DRG co-culture

For co-cultures of DRGs, mice were used with E13.5 and rats with E15.5. The mother was sacrificed and the embryos were removed and transferred into basal medium on ice. The DRGs from the embryos were carefully dissected taking care to get rid of all spinal cord tissue. The DRGs were transferred into a tube and spun down. The supernatant was replaced by 0.25% trypsin and digested for 45min at 37°C. The digestion was stopped with FCS and the tissue was triturated by passing through a heat sealed Pasteur pipet. The cells were spun down and the pellet was platted in a drop of basic medium onto collagen-coated cover slips. The next days the wells were filled with basic medium. When indicated, cells were incubated with an AAV1/2-hSyn-Cre-WPRE virus (provided by Waja Wegner& Katrin Willig) in the medium. After one week, the medium was switched to myelination medium. After changing the medium (2-3 days) for two weeks the cover slips were fixed in 4% PFA or collected in RLT buffer for RNA isolation.

MEM:	100 U/mL	Pen/Strep
	10% [v/v]	FCS
	In MEM	

Basic medium:	50ng/mL	NGF
	In MEM	

Myelination medium:	50ng/mL	NGF
	50µg/mL	Ascorbic acid
	In MEM	

Collagen coating: Pure collagen was self-made by collecting tendons from rat tails and using dialysis tubes to achieve pure collagen. 1mL collagen was diluted in 1mL 0.001% acetic acid. Small drops were placed on coverslips and distributed with a spatula and left to dry.

6.2.4. Sample processing and analysis

6.2.4.1. DNA extraction and genotyping

DNA extraction was done in Modified Gitschier buffer (MGB) and Proteinase K at 55°C and shaking overnight followed by incubation at 95°C for 10min. For sensitive Polymerase chain reactions (PCR), the DNA was isolated using the Genomic DNA isolation kit for tissue and cells from Nexttec following the manufacturer's instructions. PCR was done with the protocols and primers (all diluted to 10pmol) listed below. The PCR product was run on agarose gel using GelRed (1:20 000) to stain the DNA fragments and the gels were imaged using the Intas UV illuminator.

MGB:	67 mM	Tris pH 8.8
	16.6 mM	$(NH_4)2SO_4$
	6.5 mM	$MgCl_2$
	0.5% [v/v]	Triton X-100
	1mg/mL	Proteinase K

200µL per biopsie

Pmp22^{tg} rats (WT ~300bp; tg ~500bp)

DNA	1µL	95°C		
Buffer 5x	4µL	95°C	3min	
dNTPs (2mM)	1µL	56°C	30s	35 cycles
Primer 2201	1µL	72°C	30s	
Primer 2202	1µL	95°C	30s	
Primer 23312	1µL	56°C	1min	
Primer 23313	1µL	72°	5min	
GoTaq (5units/µL)	0.1µL			
ddH_2O	10.9µL			

Pmp22^{tg} mice (WT ~700bp; tg ~150bp)

DNA	1µL	94°C		
Buffer 5x	4µL	94°C	3min	
dNTPs (2mM)	1µL	56°C	45s	35 cycles
Primer 11906	1µL	72°C	30s	
Primer 11907	1µL	95°C	30s	
Primer 2016	1µL	56°C	1min	
Primer 7315	1µL			
GoTaq (5units/µL)	0.1µL			
ddH_2O	10.9µL			

ATeam (tg ~247bp)

DNA	0.5µL	95°C		
Buffer 5x	4µL	95°C	3min	
dNTPs (2mM)	2µL	60°C	30s	25 cycles
Primer 4858	1µL	72°C	30s	
Primer 4859	1µL	95°C	30s	
GoTaq (5units/µL)	0.1µL	60°C	30s	
ddH_2O	11.9µL	72°C	3min	

roGFP2 (WT ~159bp; cre ~339bp)

DNA	1µL	94°C		
Buffer 5x	4µL	94°C	5min	
dNTPs (2mM)	2µL	94°C	30s	30 cycles
Primer 2444	0.5µL	60°C	30s	
Primer 38548	0.5µL	72°C	30s	
Primer 38549	0.5µL	72°C	5min	
GoTaq (5units/µL)	0.1µL			
ddH_2O	12.4µL			

Dhh Cre (WT ~700bp; cre ~400bp)

DNA	1µL	94°C		
Buffer 5x	4µL	94°C	1min 30s	
dNTPs (2mM)	1µL	94°C	30s	30 cycles
Primer 10967	1µL	58°C	30s	
Primer 15793	1µL	72°C	30s	
Primer 2016	2µL	72°C	2min	
Primer 7315	2µL			
GoTaq (5units/µL)	0.1µL			
ddH_2O	8.9µL			

Slc2a1 fl (WT ~335bp; loxp ~420bp)

DNA	0.5µL	94°C		
Buffer 5x	4µL	94°C	5min	
dNTPs (2mM)	2µL	94°C	30s	30 cycles
Primer 37740	1µL	60°C	30s	
Primer 37741	1µL	72°C	45s	
GoTaq (5units/µL)	0.1µL	72°C	5min	
ddH_2O	11.9µL			

Olig2 Cre (WT ~355bp; cre ~600bp)

DNA	1µL	95°C			
Buffer 5x	4.2µL	95°C	3min		
dNTPs (2mM)	2.1µL	95°C	30s		35 cycles
Primer 30901	0.5µL	60°C	30s		
Primer 30951	0.25µL	72°C	60s		
Primer 10967	0.5µL	72°C	5min		
GoTaq (5units/µL)	0.07µL				
ddH_2O	12.38µL				

Slc2a3 fl (WT ~348bp; floxp ~400bp)

DNA (diluted 1:5)	1.5µL	94°C			
Buffer 5x	4µL	94°C	5min		
dNTPs (2mM)	1µL	94°C	30s		35 cycles
Primer 37768	1µL	62°C	30s		
Primer 37769	1µL	72°C	2min		
GoTaq (5units/µL)	0.1µL	72°C	5min		
ddH_2O	12.9µL				

Slc2a3 fl rec (WT and floxp >1kb; rec ~361bp)

DNA (diluted 1:5)	1.5µL	94°C			
Buffer 5x	4µL	94°C	5min		
dNTPs (2mM)	1µL	94°C	30s		35 cycles
Primer 37768	1µL	62°C	30s		
Primer 38311	1µL	72°C	2min		
GoTaq (5units/µL)	0.1µL	72°C	5min		
ddH_2O	12.9µL				

6.2.4.2. RNA isolation

The dissected tissue was transferred into QIAzol Lysis Reagent and homogenized using the Precellys homogenizer (PeqLab) (2 times at 6000rpm for 15s with 30s break). This was repeated if lysate did not appear clear. Chloroform was added and the samples were centrifuged to separate organic and aquatic phase. Using the Qiagen

RNeasy Mini Kit, the aquatic phase was further processed using the manufacturer's instructions for cleaned lysates. The RNA was eluated in 30µL. RNA quality and quantity were analyzed using the NanoDrop 2000 spectrophotometer (ThermoScientifc).

RNA isolation from blood was performed by Beate Veith. The kit Pax Gene blood RNA kit from Qiagen was used according to the manufacturer's instructions.

6.2.4.3. cDNA synthesis

For mRNA analysis RNA was then used to synthesis cDNA.

~ 400ng	RNA (in 22µL)
2µL	Oligo dT (0.6 pmol/µL)
2µL	N9 primer (25 pmol/µL)

For 2min at 70°C the primers and RNA was denatured. On ice, the following Master Mix was added.

8µL	1st Strand Buffer
4µL	0.1mM DTT
1µL	dNTP Mix (each 10mM)
1µL	SuperScript III reverse transcriptase (200U/µL)

The samples were incubated at 25°C for 10min followed by 50°C and 55°C each for 45min before the cDNA was diluted to 1ng/µL and stored at -20°C until further use.

6.2.4.4. Quantitative real time polymerase chain reaction (qRT-PCR)

To quantify mRNA the GoTaq qPCR system by Promega was used.

2ng	cDNA
0.2µL	each of forward and reverse Primer (50pmol/µL)
5µL	2x GoTaq qPCR Master Mix
	Total volume 10µL

For each sample, technical replicates were done and water as a negative control was included. The reaction was run on a Light Cycler 480 (Roche) using the following protocol.

50°C	120s	Warm up
95°C	600s	Melting
60°C	20s	Annealing
72°C	60s	Elongation and detection
95°C	10s	Melting → back to step 3 → 45 cycles

Using the light cyclers corresponding software the Ct values were extracted from the raw data. In Excel, the technical replicates for each sample were averaged. Statistical outlier using Grubbs Test were excluded at this step. To counteract differences in cDNA input Ct values of housekeeper genes were subtracted from the gene of interests Ct (*Rplp0* and *18s* for mice and *Rplp0* and *CyPhA* for rats). After the normalization, the Ct values were delogartimized using the 1.8^{th} square root and the fold change of all biological replicates was determined setting the control group to 1.

The specificity of new primers was determined by testing the melting curve of PCR products after qRT-PCR. The plates were analyzed on the light cycler using the following protocol.

95°C	60s	Warm Up
40°C	60s	-
60°C - 95°C	1s/ 1°C	Continuous increment of temperature until 95°C

It is assumed that a specific primer pair only gives rise to one PCR product, which will in turn have the same Melting Temperature.

6.2.4.5. Protein isolation

Nervous tissue was homogenized using the Precellys homogenizer (PeqLab) (2 times at 6000rpm for 15s with 30s break). This was repeated if lysate did not appear clear in the following sucrose buffer.

Sucrose Buffer:	270mM	Sucrose
	10mM	Tris-HCl pH7.4
	1mM	$NaHCO_3$
	1mM	$MgCl_2$
		Protease inhibitor
		Phosphatase inhibitor

Protein concentrations were determined using the NanoDrop 2000.

6.2.4.6. SDS-Page and Western Blot

To investigate the quantity of proteins of interest SDS-page and Western Blot was used.

Samples were prepared with 5x loading dye and 20µM DTT.

5xLoading dye	0.227 M	Tris (pH 6.8)
	5% [w/v]	SDS
	25%[v/v]	Glycerol
	0.5%[w/v]	Bromphenol blue

To separate the proteins in one sample according to size SDS-Page gels with 12% acrylamide separation gels were used. The gels were casted using the following protocols.

Separation gel:	12% [v/v]	Acrylamide
	0.4 M	Tris-HCl (pH 8.8)
	0.1% [w/v]	SDS
	0.03% [w/v]	APS
	0.08% [v/v]	TEMED

Stacking gel:	4% [v/v]	Acrylamide
	125 mM	Tris-HCl (pH 6.8)
	0.05% [w/v]	APS
	0.1% [v/v]	TEMED

The samples were loaded in desired quantity into the pockets of the gels and the gels were run using the BioRad system first with lower voltage and then up to 100V. PageRuler was used as a marker.

Running buffer (Laemmli):	25 mM	Tris-HCl
	192 mM	Glycine
	1% [w/v]	SDS

Following the separation according to size the proteins were blotted onto PVDF membranes using a wet chamber system at 65V for two hours.

Transfer buffer:	39 mM	Glycine
	48 mM	Tris-HCl
	20% [v/v]	Methanol

After the transfer of the proteins onto the membrane a total protein stain was performed. The membrane was washed several times with water, which was followed by 5min in staining solution. Subsequently membranes were washed twice for 1min. The membrane was imaged using the Intas ECL ChemoStar in the red channel.

Staining solution:	7% [v/v]	Acetic acid
	30% [v/v]	Methanol
	6.2µM	FastGreen

Washing solution:	7% [v/v]	Acetic acid
	30% [v/v]	Methanol

The membranes were washed in water and then incubate in blocking buffer for 45min at room temperature. Primary antibody incubation was done overnight at 4°C and after washing with TBST secondary antibody incubation was carried out at room temperature for 1hr. After several washing steps, the membrane was imaged using ECL and the Intas ECL ChemoStar. Protein quantification was done using ImageJ and the function “Gels”. Fold changes were calculated setting the control group to 1.

TBS with Tween20 (TBST):	50 mM	Tris-HCl (pH 7.4)
	150 mM	NaCl
	0.05% [v/v]	Tween20

Blocking buffer:	5% [w/v]	Low fat milk powder in 1x TBST

6.2.4.7. EM

After dissection, nerves were transferred into Karlsson and Schulz (K&S) buffer for immersion fixation. Incubation was done at 4°C for at least one week.

Phosphate buffer (PB):	13mM	$NaH_2PO_4 \cdot H_2O$
pH7.4	84mM	$Na_2HPO_4 \cdot 2H_2O$
	85mM	NaCl

K&S:	4%	Paraformaldehyde
	2.5%	Glutaraldehyde
		In PB Buffer

Afterwards samples were post fixed in osmium tetraoxide and dehydrated to be embedded in epoxy resin. Embedding was done automated using LYNX with the following protocol.

Epon:	Glycidether 100	21.4g
	DDSA	14.4g
	MNA	11.3g
Stir for 10min		
	DMP-30	0.84mL
Stir for 20min		

PB	3x10min	4°C
2% OsO_4	4h	
PB	3x10min	4°C
30%/50%/70%/90% Acetone	20min each	Room Temp.
100% Acetone	4x10min	Room Temp.
Aceton/Epon 2:1	2h	Room Temp.
Aceton/Epon 1:1	2h	Room Temp.
Aceton/Epon 1:2	4h	Room Temp.
Epon	4h	Room Temp.

Epon needs to be polymerized for 24h at 60°C. Embedded tissue was cut in semi thin (0.5µm) or ultrathin (50nm) sections using the UltracutS (Leica) and diamond knifes. Semi thin sections were stained with a combination of Gallays staining and methylene blue /Azure II blue staining.

Etching solution:	13.34% [w/v]	Potassium hydroxide
	100 ml	Methanol
	50 ml	Propylene oxide
	Stir for 30 min on ice.	
Incubation solution	0.1%[w/v]	Ammoniumnitrat
	0.1%[w/v]	Silbernitrat
	0.3%[v/v]	4% Natriumhydroxid(pH7.4-7.6)

Developing solution	Solution A (100mL):	5% [w/v]	Sodium carbonate
	Solution B (70mL):	0.2%[w/v]	Ammonium nitrate
		0.2%[w/v]	Silver nitrate
		1% [w/v]	Silicotungstic acid
	Solution C (30mL):	0.2%[w/v]	Ammonium nitrate
		0.2%[w/v]	Silver nitrate
		1% [w/v]	Silicotungstic acid
		0.7% [v/v]	37%Formol

Methylene/Azure II Blue:	1% [w/v] Azure II in ddH_2O	
	1% [w/v] Methylene Blue in 1% sodium borate	
	Mix both solutions equally and filter before use.	

Etching solution	5min	
90%/70%/50% Ethanol	5min each	
Running ddH_2O	5min	
Pyridine:acetic anhydride 1:2	30min	
ddH_2O	10x1min	
Incubation solution	1min	Microwave 150watts
Cooling down	10min	Room temperature.
0.5% acetic acid	3x5min	
Developing solution	1min	(prepare freshly)
1% acetic acid	3x5min	
ddH_2O	1min	
2% sodium thiosulfate	5min	
ddH_2O	5min	
Methylene/Azure II blue	1min	
Running ddH_2O		

After drying, the slides were mounted in Eukitt. Imaging was done using Axiophot ImagerZ1 (Zeiss) and the ZEN2 imaging software.

Semi thin sections were used to analyze g-ratio. ImageJ was used for this analysis. Shortly the images were converted to 8bit and the threshold was adjusted to recognize the axons. The particle analyszer was used to identify ROIs (single axons). This was done again with an inverted image for the myelin sheaths. The area was used to calculate the diameter of both circles in Excel.

$$\text{g-ratio} = \frac{diameter\ axon}{diameter\ outer\ myelin\ boarder}$$

Ultrathin sections were transferred onto mesh grids (coated with Formvar) and contrasted following the protocol below.

Formvar:	1.25% [w/v]	Formvar
		In chloroform

Lead citrate:	1.33g	$Pb(NO_3)_2$
	1.76g	$Na_3(C_6H_5O_7)$

In 30mL ddH_2O; shaking for 30min

1M NaOH →pH12

Fill up to 50mL

Centrifuge before using solution

UranylLess	20min
ddH_2O	5x1min
Lead citrate	5min
ddH_2O	5x1min

Imaging was done using EM900 (Zeiss) with wide-angle dual speed 2K-CCD-Cameras (TRS, Moorenweis) using the imaging software ImageSP (TRS, SysProg).

For cryo Immuno-electron microscopy, to be able to label proteins of interest in electron micrographs, nerves were immersion fixed in the following solution and then infiltrated with 2.3M sucrose.

IEM-K&S:	0.2% [v/v]	Glutaraldehyde
	4% [v/v]	PFA
	In PB buffer	

Filtrate and check pH

Samples were sectioned with UC6 (Leica) (sectioning done by Christian Maack) and stained with the following protocol for protein A Gold labelling.

PBS	3x2min
PBS 0.1% Glycin	3x2min
PBS 1% BSA	30min
1st AB in PBS 1% BSA	1h
PBS 0.1% BSA	5x2min
Protein-A-Gold in PBS 1%BSA	20min
PBS	5x2min
PBS 1% glutaraldehyde	5min
ddH_2O	10x1min
Uranylacetate	5min on ice
Methylcellulose uranylacetate	5min on ice
	Let dry

6.2.4.8. Histology

After dissection, the nerves were immersion fixed in PFA for 24hr at 4°C and then stored in PBS until further processing.

PFA: 4% Paraformaldehyde
In PB buffer

PBS:	170mM	NaCl
pH7.4	3.4mM	KCl
	4mM	$Na_2HPO_4 2H_2O$
	1.8mM	KH_2PO_4

For easier handling, the nerves were embedded in 2% agarose in PBS before being paraffin infiltrated using the STP120-2 Spin Tissue Processor (Thermo Scientific) with the following protocol.

50% Ethanol	1h
70% Ethanol	2x 2h
96% Ethanol	2x 1h
100% Ethanol	2x 1h
2-Propanol	1h
Xylol	2x 2h
Paraffin wax (60°C)	2x 1h

Following paraffin infiltration, the samples were embedded in wax block with the help of the HistoStar™ Embedding Workstation (Thermo Scientific). Blocks were cut into 5µm thin sections and dried at 37°C over night. To prepare sections for staining they were deparaffinised and rehydrated.

Citrate buffer:	1.8mM	Citric acid
pH6.0	8.2mM	Sodium citrate

TRIS-buffer	50mM	Tris-HCl pH7.6
	0.9% [w/v]	NaCl

TRIS-buffer/milk	2% [w/v]	Low fat milk powder
	In TRIS Buffer.	
	Filter before use.	

	10min	60°C
Xylol/Xylol/Isopropanol:Xylol	10min each	
100/90/70/50% Ethanol	5min each	
ddH_2O	5min	
Citrate buffer	5min	
Citrate buffer (hot)	10min	600Watt microwave
	20min	Room temp.
TRIS-buffer/milk	5min	

Blocking was done in PBS/BSA and 20% goat serum at room temperature for 20 min followed by primary antibody in PBS/BSA incubation at 4°C overnight. After 3x5min washing steps in TRIS-buffer/milk the sections were incubated in secondary antibody coupled to fluorophores and DAPI in PBS/BSA at room temperature for 1hr. Before mounting the samples in mowiol three washing steps in TRIS-buffer were done.

PBS/BSA	40mM	Sodium dihydrogen phosphate
	160mM	Disodium hydrogen phosphate
	1.8%[w/v]	NaCl
	1.0% [w/v]	BSA

Mowiol:	9.6% [w/v]	Mowiol 4-88
	24% [w/v]	Glycerol
	Stir. Add ddH_2O and stir again	
	0.1M	Tris-HCl pH8.5
	50°C for 2hr. Centrifuge 5000xg 15min and take supernatant	

Imaging was performed using the Observer (Zeiss) and the imaging software ZEN2.

6.2.4.9. Teased fiber staining

Using the samples prepared as described in 6.2.1.1 the slides were taken from -20°C and incubated directly in PFA for 5min followed by short washing step in PBS and 5min in ice-cold methanol. After three washing steps for 5min in PBS the samples were blocked at room temperature for 1hr. Primary antibody incubation was done at 4°C

overnight. Subsequently, the teased fibers were washed three times for 5min in PBS and incubated with secondary antibody coupled to fluorophores and DAPI for 1hr at room temperature. The samples were washed again for three times for 5min in PBS before there were shortly washed in ddH_2O and mounted with Mowiol. Imaging was done at the Observer Z.1 (Zeiss) or the SP5 (Leica).

Blocking solution:	10% [v/v]	Horse serum
	1% [w/v]	BSA
	0.025% [v/v]	Triton X100
	In PBS	

Antibody solution:	1.5% [v/v]	Horse serum
	0.025% [v/v]	Triton X100

6.2.4.10. STED

Teased Fibers were teased on the cover glass. Staining protocol for teased fibers was followed. Blocking was done at room temperature for two hours. Imaging was done together with Joris van Dort and Katrin Willig (Optical Nanoscopy in the Neuroscience, Max-Planck Institute of Experimental Medicine) with a custom-built set up (Dort 2018).

6.2.5. Metabolome

For Metabolome analysis P18 rats were sacrificed by cervical dislocation and subsequent decapitation. 9W old animals were decapitated using decapicones. Sciatic nerves were dissected and the epineurium was removed without PBS on a glass plate. The samples were snap frozen and the weight of the tubes measured before and after adding the samples to deduct the weight of the tissue. This was used to determine the input for the following processing. Further sample processing was done by Lisa Schlicker, Yannic Nonnenmacher und Karsten Hiller (TU Braunschweig). The protocol was adapted from Jäger and colleagues (Jäger et al 2016). Solutions were added in appropriate volumes according to the weight of the tissue sample.

EF1 (4+1 MeOH : H_2O; 1.25µg/mL $U^{13}C$-Ribitol (Internal standard)
EF2 (1µg/mL D6 glut. Acid in water)

For P18 samples, 500µL/10mg EF1, 250µL/10mg of EF2 and 400µL/10mg of $ChCl_3$ were added and 200µL of the solution was used as input. For samples obtained from 9W old rats, 1000µL/100mg of EF1, 500µL/100mg of EF2 and 800µL/100mg of $CHCl_3$ was added and 60µL of the solution was used as input.

6.2.6. Glycogen assay

To determine the glycogen content in sciatic nerves, the tissue was dissected, epineurium removed and all tissue was snap frozen after the same amount of time passed after cervical dislocation (~7min). To quantify the content the glycogen assay kit (ab65620) by Abcam was used as a colorimetric assay. Tissue of three animals was pooled for one biological replicate and cryo grinded on liquid nitrogen and dissolved in 200µL ddH_2O. Subsequently, after boiling the solution for 10min the tubes were centrifuged at 16g for 10min at 4°C. 50µL of the sample was used to perform a BCA protein assay (DC Protein Assay by Biorad) while 150µL was diluted with 50µL buffer and split into four wells (two technical replicated for glycogen measurement and for glucose background control). The manufacturer's instructions for colorimetric assay design were followed for further steps.

6.2.7. Glucose tracing experiments with 2-NBDG

Teased fibers were prepared acutely and life imaging was performed. DMEM medium with glucose and 10µM 2NBDG was added to the cells. For imaging Nikon Andor spinning disk set up was used at 37°C and 5%CO_2 ambient air for the sample.

6.2.8. FLIM acquisition and analysis

For ATP measurements *Pmp22*^{wt}*ThyAT^{tg} and *Pmp22*^{tg}*ThyAT^{tg} animals were used. The animals were sacrificed, and the Sciatic nerves were immediately isolated and transferred into artificial cerebrospinal fluid (aCSF).

aCSF:	124mM	NaCl
	2mM	$CaCl_2$
	2mM	$MgSO_4$
	1.25mM	NaH_2PO_4
	23mM	$NaHCO_3$

The nerves were fixed to the bottom of a flow through chamber with agarose pinning both extremities, and were superfused constantly with carbogen-bubbled aCSF, while being maintained at 37°C using an incubation open chamber system (ALA scientific). The lifetime measurements were performed by a 2-photon laser scanning microscope (LaVision TriMscope II setup) equipped with a pulsed laser (Cronus), a 20x immersion objective (Zeiss 20x/1.0 W Plan-Apochromat DIC Corr UV-VIS-IR), and a FLIM X1 module (LaVision Biotech). The lifetime signal of the donor fluorophore of the ATeam1.03^{YEMK} was acquired via a GaAsP/hybrid detector (Hamamatsu) in time-correlated single photon counting mode (TCSPC) while the acceptor fluorescence intensity was detected using a second GaAsP detector. The lifetime and intensity signals were digitized and displayed in the proprietary software Imspector Pro (LaVision, also used for adjusting the acquisition settings). both nerves were scanned subsequently by tile-scanning along the three dimensions xyz, to cover an area of 491*196*18 µm with a voxel size of 0.192*0.192*2.000 µm. To collect TCSPC data of the donor fluorophore (mseCFP) of ATeam 1.03^{YEMK}, the sample was first excited at 840 nm and photons with wavelength <495 nm were sent to the FLIM detector, while photons with wavelength >495 were directed to a GaAsP detector with a 542nm/50 filter to acquire the intensity signal of the acceptor fluorophore (cpYFP). Both intensity signals were used for setting ROI in correspondence of the axons in each z-plane for further lifetime calculation. To perform temporal deconvolution the instrument response function (IRF) was measured following excitation of sugar crystals at 840nm and collection of second harmonic signals (nearly instantaneous signals) between 400-440 nm, by keeping the same acquisition settings used for the experimental nerves (no immersion). The IRF was acquired at the end of each acquisition session and used to temporally deconvolve the TCSPC data. The obtained data was stitched and the lifetime was subsequently calculated as average arrival time using a MATLAB script, following the described procedure (Trevisiol et al 2020):

In time-domain fluorescence decay measurements the measured histogram $f(t)$ is a convolution of exponential decay functions with the instrument response function (IRF), $h(t)$:

$$f(t) = \int_{-\infty}^{t} dt' \sum_{j=1}^{m} \frac{A_j}{\tau_j} exp\left(-\frac{t-t'}{\tau_j}\right) h(t')$$

The reported lifetime values were then calculated as average fluorescence lifetimes $\bar{\tau}$, defined as

$$\bar{\tau} = \frac{\sum_{j=1}^{m} A_j \tau_j}{\sum_{j=1}^{m} A_j}$$

Obtained by integrating $f(t)t$ over time t

$$F_1 = \left(\int_{-\infty}^{\infty} dt'\, t' h(t')\right) \sum_{j=1}^{m} A_j + \left(\int_{-\infty}^{\infty} dt'\, h(t')\right) \sum_{j=1}^{m} A_j \tau_j$$

Where integrals over $h(t)$ are the zero[th] and first moment of the IRF, respectively:

$$H_0 = \int_{-\infty}^{\infty} dt'\, h(t') \qquad \text{and} \qquad H_1 = \int_{-\infty}^{\infty} dt' t'\, h(t')$$

And, in an analogous way, by integrating $f(t)$ over time:

$$F_0 = \int_{-\infty}^{\infty} dt'\, f(t')$$

We can then derive the average arrival time as

$$\bar{\tau} = \frac{F_1}{F_0} - \frac{H_1}{H_0}$$

The ATeam1.03[YEMK] sensor is a FRET-based sensor changing to FRET emission upon bounding to its substrate (ATP): moreover, the bound state and the change in emission lead to a reduction in lifetime of the donor moiety. The longer the measured lifetime is, the lesser the ATP content is. For that reason, the ATP concentration is better described by $\frac{1}{lifetime}$ meaning the lower the lifetime value, the higher the concentration of ATP. Through calibration experiments in vitro, using the purified protein, it has been reported that the AT1.03[YEMK], expressed by the ThyAT[tg] mice, has a sensitivity range between 0.1 mM and 10 mM ATP.

For glucose deprivation, experiments the nerves were isolated and incubated in 0 mM glucose aCSF (substituted by 10mM sucrose to maintain constant osmolarity). The incubation was performed at 37°C under carbogen bubbling. At indicated time points, the lifetime was measured and analyzed as described above. Values are depicted as a Min/Max normalization. Time point zero is set as maximum value, while time point 12 is set as minimum.

6.2.9. roGFP2 analysis

For redox state analysis $Pmp22^{wt}$*$roGFP2^{tg}$ and $Pmp22^{tg}$*$roGFP2^{tg}$ animals were used. Animals were sacrificed and sciatic nerves were freshly dissected. The samples were directly processed adapting a protocol used to fix the redox state of the sensor published before by Fujikawa and colleagues (Fujikawa et al 2016).

The following solutions were prepared freshly in PBS:

50mM NEM	Fixation
1mM DA	Oxidation
20mM DTT	Reducing

After the dissection, the nerves were transferred into NEM solution (or control solution) to remove the epineurium. All steps were done on ice.

1mM DA or 20mM DTT	10min (Only done for controls)
50mM NEM	10min
4% PFA	10min
PBS	2x5min

After incubation, the samples were mounted in Mowiol between Coverslip and slide. Storage at 4°C was done until imaging was performed. For all animals, both nerves were used. For the control samples no technical replicate was performed.

Imaging was done using an SP5 (Leica). Excitation was 405nm and 488m, while measurement was done for both channels in the green channel. Using FIJI the data was analyzed. With Auto threshholding, the images were processed and the intensity for both channels was determined. To determine the Ratio intensity at 405nm was

divided by the intensity at 488nm. The data was normalized to the value of the DTT treated sample (R_{red}).

6.2.10. RNAseq screen for disease marker identification

Analysis was performed by Nirmal Kannaiyan and Moritz Rossner (LMU Munich).

6.2.10.1. Library Preparation

Libraries were prepared from 400ng of extracted RNA using QuantSeq 3' mRNA-Seq Library Prep Kit FWD for Illumina (Lexogen, SKU 015.24) according the manufacturers protocol. Briefly, the first strand cDNA synthesis was performed using a poly-dT oligonucleotide also containing a illumina compatible sequence at its 5' end. Before the second strand synthesis, the RNA was degraded along with globin blocking primers. The second strand synthesis was initiated by a random primer also containing illumine compatible sequence at its 5' end. Subsequently, the double-stranded library was purified using magnetic beads to remove all reaction components. The purified library was further amplified using illumina compatible primers. The required number cycle was determined using PCR Add-on kit for Illumina (Lexogen, SKU 020.96). Indices were added by PCR for multiplexing. The concentration of the final yield was determined using KAPA Library Quantification Kit and was pooled in equimolar concentrations. The samples were sequenced on an Illumina NexSeq 500 Sequencer.

6.2.10.2. Data Analysis

The fastq files were demultiplexed based on the indices used. The sample specific fastq reads were then quality controlled using FASTQC and subsequently mapped to genome using STAR aligner. For patients genome version hg19 was used and the reads were quantified based on Ensembl Transcript release (version 75) at the gene level. For rat samples the rat genome version rn6 and Ensembl Transcripts release 93 was used instead. Count normalization & differential gene expression analysis were performed using DESeq2 R Package.

6.2.10.3. Further processing for list of candidates

A homology conversion was performed for the list of differentially expressed genes in patients in order to perform an overlap between patients and animal model.

Significance levels were set to 1 for rats and 0.05 for patients to prioritize the list of candidates.

6.2.11. Data analysis and statistics

Unless otherwise stated all values are Mean values of biological replicates with standard deviation. Analysis was done in Excel and Statistics and graph design were done in GraphPad Prism. Figures were assembled using Adobe Illustrator. Statistics unless stated otherwise are Student's T-test. p-values *≤0.05; **≤0.01; ***≤0.001

7. Supplement

Table S 1: List of significantly altered metabolites analyzed in an MS based approach shown in **Figure 4**.

	P18					9W					
	WT		CMT1A			WT		CMT1A			
Metabolite	Log2 FC	SD	Log2 FC	SD	p-value	Log2 FC	SD	Log2 FC	SD	p-value	
Alanine	-0.024	0.307	-0.131	0.754	0.798	-0.024	0.296	0.579	0.152	0.004	Amino acids
Aspartic acid	-0.012	0.218	0.599	0.163	0.002	-0.121	0.683	0.323	0.647	0.322	
Isoleucine	-0.092	0.610	0.121	1.343	0.779	-0.124	0.690	0.715	0.345	0.041	
Leucine	-0.123	0.712	0.332	0.733	0.380	-0.183	0.873	0.822	0.360	0.045	
Methionine	-0.129	0.721	0.235	0.430	0.374	-0.179	0.866	1.071	0.515	0.024	
N-acetyl-L-aspartic acid	-0.001	0.057	0.196	0.145	0.039	-0.003	0.109	-0.733	0.264	≤0.001	
Phenylalanine	-0.053	0.435	0.574	0.092	0.015	-0.052	0.442	0.656	0.212	0.012	
Threonine	-0.080	0.541	1.410	1.232	0.061	-0.038	0.377	0.710	0.259	0.006	
Urea	-0.091	0.587	0.303	0.515	0.319	-0.036	0.371	0.526	0.164	0.015	
Valine	-0.035	0.373	0.410	0.872	0.377	-0.040	0.387	1.102	0.221	≤0.001	
N-acetylaspartyl-glutamic acid	-0.019	0.273	-0.882	0.799	0.080	-0.030	0.330	-1.225	0.368	≤0.001	
Oxalic acid	-2.412	2.933	1.091	1.269	0.071	-0.767	2.008	1.172	0.341	0.066	Fatty aids
2-Hydroxyglutaric acid	-0.077	0.583	0.226	0.244	0.322	-0.014	0.224	-1.137	0.288	≤0.001	Mitochon-dria
3-Hydroxymethyl glutaric acid	-0.029	0.342	0.214	1.678	0.783	-0.009	0.182	-1.852	0.789	≤0.001	
Fructose	-0.019	0.276	-1.243	0.795	0.023	-0.003	0.107	-3.485	0.294	≤0.001	Monosac-charides
Galactose	-0.198	0.956	0.297	0.387	0.321	-0.010	0.186	-2.055	1.201	0.006	
Glucose	-0.093	0.592	0.812	0.586	0.056	-0.004	0.123	0.645	0.158	≤0.001	
Inosine	-0.012	0.210	1.752	0.923	0.008	-0.020	0.270	1.502	0.302	≤0.001	Purine
Threonic acid	-1.908	2.877	1.627	1.024	0.060	-0.603	2.018	0.912	0.194	0.133	Sugar acids
Glycerol	-0.050	0.430	0.753	0.484	0.036	-0.038	0.374	0.533	0.378	0.043	Sugar alcohols
Sorbitol	-0.080	0.572	-0.825	0.673	0.122	-0.015	0.233	-2.723	0.413	≤0.001	
meso-Erythritol	-0.008	0.182	-0.125	0.115	0.275	-0.012	0.214	-0.944	0.110	≤0.001	
Citric acid	-0.021	0.277	-0.019	0.211	0.994	-0.005	0.137	0.687	0.216	≤0.001	TCA acids
Fumaric acid	-0.015	0.241	0.295	0.356	0.200	-0.014	0.225	0.363	0.259	0.040	
Myo-inositol	-0.003	0.100	-0.211	0.177	0.075	-0.024	0.296	-0.543	0.253	0.018	Others
Glycolic acid-2-phosphate	-0.050	0.445	0.018	0.454	0.829	-0.015	0.230	-0.836	0.198	≤0.001	
Pyroglutamic acid	-0.011	0.202	0.400	0.718	0.309	-0.013	0.212	0.661	0.060	≤0.001	
Pyrophosphate	-0.331	1.257	-0.785	3.127	0.797	-0.198	0.900	-0.529	0.408	0.476	

Table S 2: Summary of metabolites in 9W sciatic nerve lysate and mRNA levels in tibial nerve lysates at 9W in *Pmp22*^{tg} rats (CMT1A) and age matched controls depicted in metabolic pathway summaries of **Figure 6**, **Figure 7**, **Figure 11** (Key enzymes depicted in bold, FC: fold change, SD: Standard Deviation, Students T-Test)

Metabolites						
	WT		CMT1A			
Compound	FC	SD	FC	SD	p-value	
Sorbitol	1	0.164	0.157	0.047	≤0.001	Polyol pathway
Fructose	1	0.073	0.091	0.019	≤0.001	
Glucose	1	0.084	1.571	0.171	≤0.001	Glycolysis
Glyceraldehde-3P	1	0.141	1.141	0.124	0.133	
Pyruvate	1	0.367	0.973	0.116	0.881	
Lactate	1	0.191	1.172	0.168	0.170	
Citrate	1	0.094	1.625	0.262	0.001	TCA
Succinate	1	0.120	0.927	0.044	0.240	
Fumarate	1	0.155	1.303	0.237	0.044	
Malate	1	0.087	1.051	0.097	0.411	
Oxaloacetate	1	0.783	2.301	0.499	0.014	
mRNA Expression						
	WT		CMT1A			
Gene	FC	SD	FC	SD	p-value	
Akr1b1 (Aldose reductase)	1	0.118	0.191	0.032	≤0.001	Polyol pathway
Gys1 (Glycogen synthase)	1	0.103	0.766	0.134	0.053	Glycogen
Pygb (Glycogen phosphorylase B)	1	0.200	0.713	0.125	0.079	
Slc2a1 (Solute carrier family 2 member 1)	1	0.164	0.555	0.038	0.004	Transporter
Slc2a3 (Solute carrier family 2 member 3)	1	0.032	0.523	0.144	0.001	
Slc16a1 (Solute carrier family 16 member1)	1	0.123	0.866	0.331	0.534	
Slc16a7 (Solute carrier family 16 member 7)	1	0.148	0.738	0.082	0.066	
G6pd (Glucose-6-phosphate dehydrogenase)	1	0.050	0.777	0.190	0.096	PPP
Hk1 (Hexokinase1)	1	0.062	0.699	0.153	0.020	Glycolysis
Hk2 (Hexokinase2)	1	0.093	0.701	0.165	0.034	
Pfkm (Phosphofructokinase M)	1	0.245	0.271	0.258	0.012	
Aldoa (Aldolase, Fructose-bisphosphate A)	1	0.132	0.366	0.066	≤0.001	
Aldoc (Aldolase, Fructose-bisphosphate C)	1	0.255	0.430	0.052	0.009	
Gapdh (Glyceraldehyde-3-phosphate dehydrogenase)	1	0.039	0.479	0.060	≤0.001	
Pkm2 (Pyruvate kinase M 2)	1	0.029	0.707	0.156	0.019	
Ldha (Lactate dehydrogenase A)	1	0.210	0.628	0.122	0.055	
Aco2 (Aconitase 2)	1	0.063	0.755	0.054	0.002	TCA

Mdh2 (Malate dehydrogenase 2)	1	0.300	0.755	0.183	0.272	
Sdha (Succinate dehydrogenase complex flavoprotein subunit A)	1	0.070	0.776	0.050	0.004	TCA/OXPHOS
Ndufv2 (NADH:Ubiquinone Oxidoreductase Core Subunit V2)	1	0.090	0.648	0.068	0.002	OXPHOS
Uqcr10 (Ubiquinol-cytochrome C reductase, complex III subunit X)	1	0.123	0.758	0.053	0.020	
Cox4i1 (Cytochrome c oxidase subunit 4 Isoform 1, Mitochondrial)	1	0.184	0.756	0.123	0.105	
Atp5f1a (ATP synthase F1 subunit alpha)	1	0.071	0.860	0.115	0.124	
Mtnd2 (NADH-ubiquinone oxidoreductase chain 2)	1	0.075	0.887	0.133	0.245	
Mtcytb (Cytochrome b)	1	0.115	0.969	0.075	0.707	
mtCo1 (Mitochondrial encoded cytochrome C oxidase I)	1	0.119	0.917	0.103	0.394	
mtAtp6 (mitochondrial encoded ATP synthase membrane subunit 6)	1	0.106	0.909	0.152	0.428	

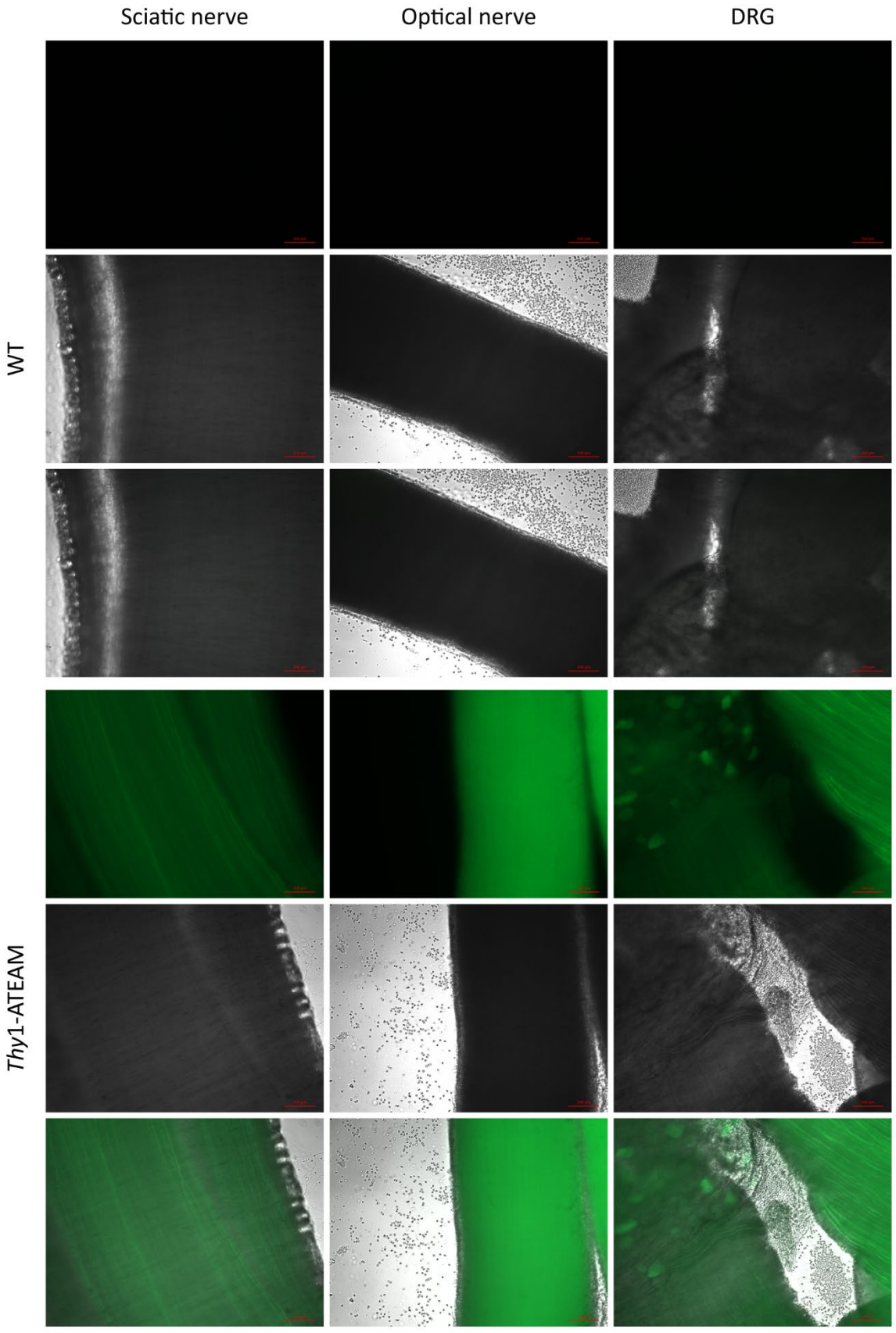

Figure S 1: Expression of *Thy1*-ATEAM. Upper panels background level of WT animals without the transgene coding for the sensor. Lower panels' intensity of sensor expression in sciatic nerves, optic nerves and dorsal root ganglia. (Scale bar: 100µm)

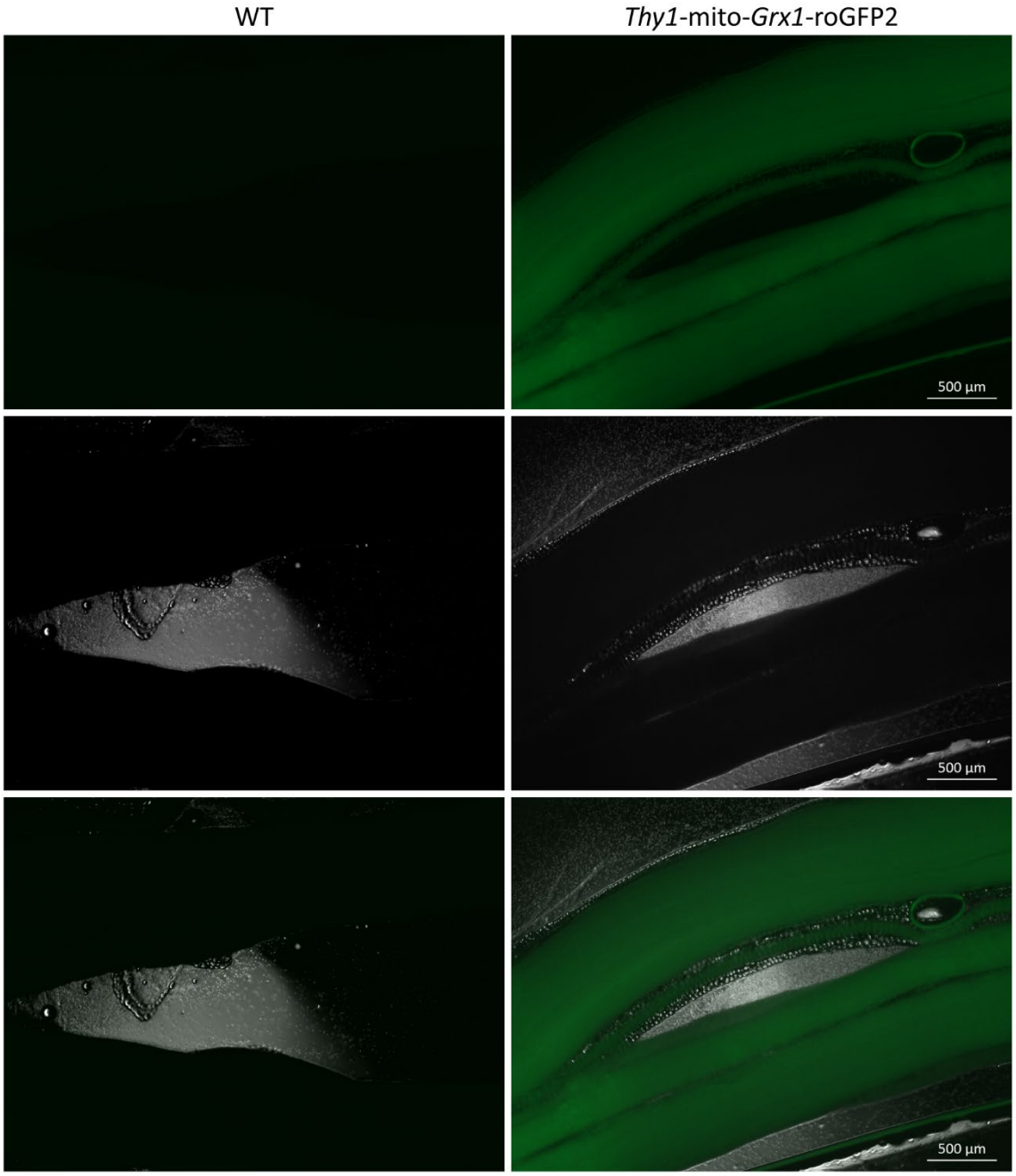

Figure S 2: Expression of *Thy1*-mito-*Grx1*-roGFP2. (Left panels) WT animal not expressing the sensor in sciatic nerve in comparison to (Right panels) animal expressing the sensor. (Scale bar: 500µm)

8. References

Altevogt BM, Kleopa KA, Postma FR, Scherer SS, Paul DL. 2002. Connexin29 is uniquely distributed within myelinating glial cells of the central and peripheral nervous systems. *The Journal of neuroscience : the official journal of the Society for Neuroscience* 22: 6458-70

Arroyo EJ, Scherer SS. 2000. On the molecular architecture of myelinated fibers. *Histochemistry and cell biology* 113: 1-18

Attarian S, Vallat JM, Magy L, Funalot B, Gonnaud PM, et al. 2014. An exploratory randomised double-blind and placebo-controlled phase 2 study of a combination of baclofen, naltrexone and sorbitol (PXT3003) in patients with Charcot-Marie-Tooth disease type 1A. *Orphanet journal of rare diseases* 9: 199

Babetto E, Wong KM, Beirowski B. 2020. A glycolytic shift in Schwann cells supports injured axons. *Nature neuroscience* 23: 1215-28

Bajar BT, Wang ES, Zhang S, Lin MZ, Chu J. 2016. A Guide to Fluorescent Protein FRET Pairs. 16: 1488

Bao J, Wolpowitz D, Role LW, Talmage DA. 2003. Back signaling by the Nrg-1 intracellular domain. *The Journal of cell biology* 161: 1133-41

Bas-Orth C, Tan YW, Lau D, Bading H. 2017. Synaptic Activity Drives a Genomic Program That Promotes a Neuronal Warburg Effect. *The Journal of biological chemistry* 292: 5183-94

Beirowski B, Babetto E, Golden JP, Chen YJ, Yang K, et al. 2014. Metabolic regulator LKB1 is crucial for Schwann cell-mediated axon maintenance. *Nature neuroscience* 17: 1351-61

Berghoff SA, Düking T, Spieth L, Winchenbach J, Stumpf SK, et al. 2017. Blood-brain barrier hyperpermeability precedes demyelination in the cuprizone model. *Acta Neuropathologica Communications* 5: 94

Berthold CH, Rydmark M. 1983. Electron microscopic serial section analysis of nodes of Ranvier in lumbosacral spinal roots of the cat: ultrastructural organization of nodal compartments in fibres of different sizes. *Journal of neurocytology* 12: 475-505

Birchmeier C. 2009. ErbB receptors and the development of the nervous system. *Experimental cell research* 315: 611-8

Birchmeier C, Nave KA. 2008. Neuregulin-1, a key axonal signal that drives Schwann cell growth and differentiation. *Glia* 56: 1491-7

Bouçanova F, Chrast R. 2020. Metabolic Interaction Between Schwann Cells and Axons Under Physiological and Disease Conditions. *Frontiers in cellular neuroscience* 14: 148

Boyle ME, Berglund EO, Murai KK, Weber L, Peles E, Ranscht B. 2001. Contactin orchestrates assembly of the septate-like junctions at the paranode in myelinated peripheral nerve. *Neuron* 30: 385-97

Breckwoldt M, Pfister F, Bradley P, Marinkovic P, Williams P, et al. 2014. Multiparametric optical analysis of mitochondrial redox signals during neuronal physiology and pathology in vivo. *Nature medicine* 20

Brennan A, Dean CH, Zhang AL, Cass DT, Mirsky R, Jessen KR. 2000. Endothelins control the timing of Schwann cell generation in vitro and in vivo. *Developmental biology* 227: 545-57

Britsch S, Goerich DE, Riethmacher D, Peirano RI, Rossner M, et al. 2001. The transcription factor Sox10 is a key regulator of peripheral glial development. *Genes & development* 15: 66-78

Brockes JP, Fields KL, Raff MC. 1979. Studies on cultured rat Schwann cells. I. Establishment of purified populations from cultures of peripheral nerve. *Brain research* 165: 105-18

Brown AM, Evans RD, Black J, Ransom BR. 2012. Schwann cell glycogen selectively supports myelinated axon function. *Annals of neurology* 72: 406-18

Buchstaller J, Sommer L, Bodmer M, Hoffmann R, Suter U, Mantei N. 2004. Efficient isolation and gene expression profiling of small numbers of neural crest stem cells and developing Schwann cells. *The Journal of neuroscience : the official journal of the Society for Neuroscience* 24: 2357-65

Burns J, Ouvrier R, Estilow T, Shy R, Laurá M, et al. 2012. Validation of the Charcot–Marie–Tooth disease pediatric scale as an outcome measure of disability. 71: 642-52

Caldwell JH, Schaller KL, Lasher RS, Peles E, Levinson SR. 2000. Sodium channel Na(v)1.6 is localized at nodes of ranvier, dendrites, and synapses. *Proceedings of the National Academy of Sciences of the United States of America* 97: 5616-20

Cisterna BA, Arroyo P, Puebla C. 2019. Role of Connexin-Based Gap Junction Channels in Communication of Myelin Sheath in Schwann Cells. 13

Cornett KMD, Menezes MP, Shy RR, Moroni I, Pagliano E, et al. 2017. Natural history of Charcot-Marie-Tooth disease during childhood. 82: 353-59

Cortese A, Zhu Y, Rebelo AP, Negri S, Courel S, et al. 2020. Biallelic mutations in SORD cause a common and potentially treatable hereditary neuropathy with implications for diabetes. *Nature genetics* 52: 473-81

D'Antonio M, Droggiti A, Feltri ML, Roes J, Wrabetz L, et al. 2006. TGFbeta type II receptor signaling controls Schwann cell death and proliferation in developing nerves. *The Journal of neuroscience : the official journal of the Society for Neuroscience* 26: 8417-27

Davis JQ, Lambert S, Bennett V. 1996. Molecular composition of the node of Ranvier: identification of ankyrin-binding cell adhesion molecules neurofascin (mucin+/third FNIII domain-) and NrCAM at nodal axon segments. *The Journal of cell biology* 135: 1355-67

Deck M, Van Hameren G, Campbell G, Bernard-Marissal N, Devaux J, et al. 2020. Myelinating Schwann cells use Warburg effect to sustain axonal physiology and function. 2020.04.23.049056

Dessaud E, Yang LL, Hill K, Cox B, Ulloa F, et al. 2007. Interpretation of the sonic hedgehog morphogen gradient by a temporal adaptation mechanism. *Nature* 450: 717-20

Dhar SS, Ongwijitwat S, Wong-Riley MT. 2009. Chromosome conformation capture of all 13 genomic Loci in the transcriptional regulation of the multisubunit bigenomic cytochrome C oxidase in neurons. *The Journal of biological chemistry* 284: 18644-50

Dienel GA. 2019. Brain Glucose Metabolism: Integration of Energetics with Function. 99: 949-1045

Domènech-Estévez E, Baloui H, Repond C, Rosafio K, Médard JJ, et al. 2015. Distribution of monocarboxylate transporters in the peripheral nervous system suggests putative roles in lactate shuttling and myelination. *The Journal of neuroscience : the official journal of the Society for Neuroscience* 35: 4151-6

Dong Z, Brennan A, Liu N, Yarden Y, Lefkowitz G, et al. 1995. Neu differentiation factor is a neuron-glia signal and regulates survival, proliferation, and maturation of rat Schwann cell precursors. *Neuron* 15: 585-96

Dort Jv. 2018. *Aberration correction in STED microscopy*. Georg-August University Göttingen

Edgar JM, McLaughlin M, Werner HB, McCulloch MC, Barrie JA, et al. 2009. Early ultrastructural defects of axons and axon-glia junctions in mice lacking expression of Cnp1. *Glia* 57: 1815-24

Eichel MA, Gargareta VI, D'Este E, Fledrich R, Kungl T, et al. 2020. CMTM6 expressed on the adaxonal Schwann cell surface restricts axonal diameters in peripheral nerves. *Nature communications* 11: 4514

Eichinger K, Burns J, Cornett K, Bacon C, Shepherd ML, et al. 2018. The Charcot-Marie-Tooth Functional Outcome Measure (CMT-FOM). *Neurology* 91: e1381

Feltri ML, Poitelon Y, Previtali SC. 2016. How Schwann Cells Sort Axons: New Concepts. *The Neuroscientist : a review journal bringing neurobiology, neurology and psychiatry* 22: 252-65

Fidler TP, Campbell RA, Funari T, Dunne N, Balderas Angeles E, et al. 2017. Deletion of GLUT1 and GLUT3 Reveals Multiple Roles for Glucose Metabolism in Platelet and Megakaryocyte Function. *Cell reports* 20: 881-94

Fjell J, Hjelmström P, Hormuzdiar W, Milenkovic M, Aglieco F, et al. 2000. Localization of the tetrodotoxin-resistant sodium channel NaN in nociceptors. *Neuroreport* 11: 199-202

Fledrich R, Abdelaal T, Rasch L, Bansal V, Schütza V, et al. 2018. Targeting myelin lipid metabolism as a potential therapeutic strategy in a model of CMT1A neuropathy. *Nature communications* 9: 3025

Fledrich R, Kungl T, Nave KA, Stassart RM. 2019. Axo-glial interdependence in peripheral nerve development. *Development (Cambridge, England)* 146

Fledrich R, Mannil M, Leha A, Ehbrecht C, Solari A, et al. 2017. Biomarkers predict outcome in Charcot-Marie-Tooth disease 1A. *Journal of Neurology, Neurosurgery & Psychiatry* 88: 941

Fledrich R, Schlotter-Weigel B, Schnizer TJ, Wichert SP, Stassart RM, et al. 2012a. A rat model of Charcot-Marie-Tooth disease 1A recapitulates disease variability and supplies biomarkers of axonal loss in patients. *Brain : a journal of neurology* 135: 72-87

Fledrich R, Stassart RM, Klink A, Rasch LM, Prukop T, et al. 2014. Soluble neuregulin-1 modulates disease pathogenesis in rodent models of Charcot-Marie-Tooth disease 1A. *Nature medicine* 20: 1055-61

Fledrich R, Stassart RM, Sereda MW. 2012b. Murine therapeutic models for Charcot-Marie-Tooth (CMT) disease. *British medical bulletin* 102: 89-113

Fujikawa Y, Roma LP, Sobotta MC, Rose AJ, Diaz MB, et al. 2016. Mouse redox histology using genetically encoded probes. *Science signaling* 9: rs1

Fünfschilling U, Supplie LM, Mahad D, Boretius S, Saab AS, et al. 2012. Glycolytic oligodendrocytes maintain myelin and long-term axonal integrity. *Nature* 485: 517-21

Garcia CA, Malamut RE, England JD, Parry GS, Liu P, Lupski JR. 1995. Clinical variability in two pairs of identical twins with the Charcot-Marie-Tooth disease type 1A duplication. *Neurology* 45: 2090-3

Gautier B, Hajjar H, Soares S, Berthelot J, Deck M, et al. 2020. Long term AAV2/9-mediated silencing of PMP22 prevents CMT1A disease in rats and validates skin biomarkers as treatment outcome measure. *bioRxiv*: 2020.01.29.924605

González RG, Barnett P, Aguayo J, Cheng HM, Chylack LT, Jr. 1984. Direct measurement of polyol pathway activity in the ocular lens. *Diabetes* 33: 196-9

Graham RC, Hughes RAC. 2006. A modified peripheral neuropathy scale: the Overall Neuropathy Limitations Scale. *Journal of Neurology, Neurosurgery & Psychiatry* 77: 973

Grossman LI, Lomax MI. 1997. Nuclear genes for cytochrome c oxidase. *Biochimica et Biophysica Acta (BBA) - Gene Structure and Expression* 1352: 174-92

Harris JJ, Attwell D. 2012. The Energetics of CNS White Matter. 32: 356-71

Hartmannsberger B, Doppler K, Stauber J, Schlotter-Weigel B, Young P, et al. 2020. Intraepidermal nerve fibre density as biomarker in Charcot–Marie–Tooth disease type 1A. *Brain Communications* 2

Havula E, Hietakangas V. 2012. Glucose sensing by ChREBP/MondoA–Mlx transcription factors. *Seminars in Cell & Developmental Biology* 23: 640-47

Hers HG. 1956. The mechanism of the transformation of glucose in fructose in the seminal vesicles. *Biochimica et biophysica acta* 22: 202-3

Huxley C, Passage E, Robertson AM, Youl B, Huston S, et al. 1998. Correlation between varying levels of PMP22 expression and the degree of demyelination and reduction in nerve conduction velocity in transgenic mice. *Human molecular genetics* 7: 449-58

Jacob C, Christen CN, Pereira JA, Somandin C, Baggiolini A, et al. 2011. HDAC1 and HDAC2 control the transcriptional program of myelination and the survival of Schwann cells. *Nature neuroscience* 14: 429-36

Jaegle M, Ghazvini M, Mandemakers W, Piirsoo M, Driegen S, et al. 2003. The POU proteins Brn-2 and Oct-6 share important functions in Schwann cell development. *Genes & development* 17: 1380-91

Jäger C, Hiller K, Buttini M. 2016. Metabolic Profiling and Quantification of Neurotransmitters in Mouse Brain by Gas Chromatography-Mass Spectrometry. *Current protocols in mouse biology* 6: 333-42

Jahn O, Tenzer S, Werner HB. 2009. Myelin Proteomics: Molecular Anatomy of an Insulating Sheath. *Molecular Neurobiology* 40: 55-72

Jessen KR. 2004. Glial cells. *The international journal of biochemistry & cell biology* 36: 1861-7

Jessen KR, Brennan A, Morgan L, Mirsky R, Kent A, et al. 1994. The Schwann cell precursor and its fate: a study of cell death and differentiation during gliogenesis in rat embryonic nerves. *Neuron* 12: 509-27

Jessen KR, Mirsky R. 2002. Signals that determine Schwann cell identity. *Journal of anatomy* 200: 367-76

Jessen KR, Mirsky R. 2005. The origin and development of glial cells in peripheral nerves. *Nature reviews. Neuroscience* 6: 671-82

Jessen KR, Mirsky R. 2016. The repair Schwann cell and its function in regenerating nerves. 594: 3521-31

Jessen KR, Mirsky R. 2019. Schwann Cell Precursors; Multipotent Glial Cells in Embryonic Nerves. *Frontiers in molecular neuroscience* 12: 69

Jha MK, Morrison BM. 2018. Glia-neuron energy metabolism in health and diseases: New insights into the role of nervous system metabolic transporters. *Experimental neurology* 309: 23-31

Johnson NE, Heatwole C, Creigh P, McDermott MP, Dilek N, et al. 2018. The Charcot–Marie–Tooth Health Index: Evaluation of a Patient-Reported Outcome. 84: 225-33

Joseph NM, Mukouyama YS, Mosher JT, Jaegle M, Crone SA, et al. 2004. Neural crest stem cells undergo multilineage differentiation in developing peripheral nerves to generate endoneurial fibroblasts in addition to Schwann cells. *Development (Cambridge, England)* 131: 5599-612

Kasajima H, Yamagishi S, Sugai S, Yagihashi N, Yagihashi S. 2002. Enhanced in situ expression of aldose reductase in peripheral nerve and renal glomeruli in diabetic patients. 7: 134-34

Kern TS, Engerman RL. 1982. Immunohistochemical distribution of aldose reductase. *The Histochemical journal* 14: 507-15

Kordeli E, Davis J, Trapp B, Bennett V. 1990. An isoform of ankyrin is localized at nodes of Ranvier in myelinated axons of central and peripheral nerves. *The Journal of cell biology* 110: 1341-52

Landon DN, Langley OK. 1971. The local chemical environment of nodes of Ranvier: a study of cation binding. *Journal of anatomy* 108: 419-32

Lappe-Siefke C, Goebbels S, Gravel M, Nicksch E, Lee J, et al. 2003. Disruption of Cnp1 uncouples oligodendroglial functions in axonal support and myelination. *Nature genetics* 33: 366-74

Le Douarin N, Dulac C, Dupin E, Cameron-Curry P. 1991. Glial cell lineages in the neural crest. *Glia* 4: 175-84

Lee J-S, Lee JY, Song DW, Bae HS, Doo HM, et al. 2019. Targeted PMP22 TATA-box editing by CRISPR/Cas9 reduces demyelinating neuropathy of Charcot-Marie-Tooth disease type 1A in mice. *Nucleic Acids Research* 48: 130-40

Lee Y, Morrison BM, Li Y, Lengacher S, Farah MH, et al. 2012. Oligodendroglia metabolically support axons and contribute to neurodegeneration. *Nature* 487: 443-8

Li J, Parker B, Martyn C, Natarajan C, Guo J. 2013. The PMP22 Gene and Its Related Diseases. *Molecular Neurobiology* 47: 673-98

Li X, Lynn BD, Olson C, Meier C, Davidson KG, et al. 2002. Connexin29 expression, immunocytochemistry and freeze-fracture replica immunogold labelling (FRIL) in sciatic nerve. *The European journal of neuroscience* 16: 795-806

Ludvigson MA, Sorenson RL. 1980. Immunohistochemical localization of aldose reductase. I. Enzyme purification and antibody preparation--localization in peripheral nerve, artery, and testis. *Diabetes* 29: 438-49

Lupski JR, de Oca-Luna RM, Slaugenhaupt S, Pentao L, Guzzetta V, et al. 1991. DNA duplication associated with Charcot-Marie-Tooth disease type 1A. *Cell* 66: 219-32

Lyons DA, Pogoda HM, Voas MG, Woods IG, Diamond B, et al. 2005. erbb3 and erbb2 are essential for schwann cell migration and myelination in zebrafish. *Current biology : CB* 15: 513-24

Maekawa K, Tanimoto T, Okada S, Suzuki T, Suzuki T, Yabe-Nishimura C. 2001. Expression of aldose reductase and sorbitol dehydrogenase genes in Schwann cells isolated from rat: effects of high glucose and osmotic stress. *Brain research. Molecular brain research* 87: 251-6

Magnani P, Cherian PV, Gould GW, Greene DA, Sima AAF, Brosius FC. 1996. Glucose transporters in rat peripheral nerve: Paranodal expression of GLUT1 and GLUT3. *Metabolism* 45: 1466-73

Mannil M, Solari A, Leha A, Pelayo-Negro AL, Berciano J, et al. 2014. Selected items from the Charcot-Marie-Tooth (CMT) Neuropathy Score and secondary clinical outcome measures serve as sensitive clinical markers of disease severity in CMT1A patients. *Neuromuscular Disorders* 24: 1003-17

Meier C, Parmantier E, Brennan A, Mirsky R, Jessen KR. 1999. Developing Schwann cells acquire the ability to survive without axons by establishing an autocrine circuit involving insulin-like growth factor, neurotrophin-3, and platelet-derived growth factor-BB. *The Journal of neuroscience : the official journal of the Society for Neuroscience* 19: 3847-59

Meyer N, Richter N, Fan Z, Siemonsmeier G, Pivneva T, et al. 2018. Oligodendrocytes in the Mouse Corpus Callosum Maintain Axonal Function by Delivery of Glucose. *Cell reports* 22: 2383-94

Meyer zu Horste G, Miesbach TA, Muller JI, Fledrich R, Stassart RM, et al. 2011. The Wlds transgene reduces axon loss in a Charcot-Marie-Tooth disease 1A rat model and nicotinamide delays post-traumatic axonal degeneration. *Neurobiology of disease* 42: 1-8

Meyer zu Horste G, Prukop T, Liebetanz D, Mobius W, Nave KA, Sereda MW. 2007. Antiprogesterone therapy uncouples axonal loss from demyelination in a transgenic rat model of CMT1A neuropathy. *Annals of neurology* 61: 61-72

Michailov GV, Sereda MW, Brinkmann BG, Fischer TM, Haug B, et al. 2004. Axonal neuregulin-1 regulates myelin sheath thickness. *Science (New York, N.Y.)* 304: 700-3

Morrison AD, Clements RS, Jr., Travis SB, Oski F, Winegrad AI. 1970. Glucose utilization by the polyol pathway in human erythrocytes. *Biochemical and biophysical research communications* 40: 199-205

Morrison BM, Tsingalia A, Vidensky S, Lee Y, Jin L, et al. 2015. Deficiency in monocarboxylate transporter 1 (MCT1) in mice delays regeneration of peripheral nerves following sciatic nerve crush. *Experimental neurology* 263: 325-38

Morrow JM, Evans MRB, Grider T, Sinclair CDJ, Thedens D, et al. 2018. Validation of MRC Centre MRI calf muscle fat fraction protocol as an outcome measure in CMT1A. *Neurology* 91: e1125

Morrow JM, Sinclair CDJ, Fischmann A, Machado PM, Reilly MM, et al. 2016. MRI biomarker assessment of neuromuscular disease progression: a prospective observational cohort study. *The Lancet Neurology* 15: 65-77

Muona P, Sollberg S, Peltonen J, Uitto J. 1992. Glucose Transporters of Rat Peripheral Nerve: Differential Expression of GLUT1 Gene by Schwann Cells and Perineurial Cells In Vivo and In Vitro. 41: 1587-96

Murphy SM, Herrmann DN, McDermott MP, Scherer SS, Shy ME, et al. 2011. Reliability of the CMT neuropathy score (second version) in Charcot-Marie-Tooth disease. 16: 191-98

Nave K-A, Werner HB. 2014. Myelination of the Nervous System: Mechanisms and Functions. 30: 503-33

Nave KA. 2010. Myelination and the trophic support of long axons. *Nature reviews. Neuroscience* 11: 275-83

Nishinaka T, Shimizu K, Miura T, Yabe-Nishimura C, Terada T. 2019. Cooperative regulation of mouse aldose reductase (AKR1B3) gene transcription by Nrf2, TonEBP, and c-jun. *Chemico-Biological Interactions* 302: 36-45

Norton WT, Poduslo SE. 1973. Myelination in rat brain: changes in myelin composition during brain maturation. *Journal of neurochemistry* 21: 759-73

Pareyson D, Saveri P, Pisciotta C. 2017. New developments in Charcot-Marie-Tooth neuropathy and related diseases. *Current opinion in neurology* 30: 471-80

Pellerin L, Magistretti PJ. 1994. Glutamate uptake into astrocytes stimulates aerobic glycolysis: a mechanism coupling neuronal activity to glucose utilization. *Proceedings of the National Academy of Sciences of the United States of America* 91: 10625-9

Pillai AM, Thaxton C, Pribisko AL, Cheng JG, Dupree JL, Bhat MA. 2009. Spatiotemporal ablation of myelinating glia-specific neurofascin (Nfasc NF155) in mice reveals gradual loss of paranodal axoglial junctions and concomitant disorganization of axonal domains. *Journal of neuroscience research* 87: 1773-93

Poliak S, Matlis S, Ullmer C, Scherer SS, Peles E. 2002. Distinct claudins and associated PDZ proteins form different autotypic tight junctions in myelinating Schwann cells. *The Journal of cell biology* 159: 361-72

Poliak S, Peles E. 2003. The local differentiation of myelinated axons at nodes of Ranvier. *Nature reviews. Neuroscience* 4: 968-80

Pooya S, Liu X, Kumar VB, Anderson J, Imai F, et al. 2014. The tumour suppressor LKB1 regulates myelination through mitochondrial metabolism. *Nature communications* 5: 4993

Prukop T, Stenzel J, Wernick S, Kungl T, Mroczek M, et al. 2019. Early short-term PXT3003 combinational therapy delays disease onset in a transgenic rat model of Charcot-Marie-Tooth disease 1A (CMT1A). *PloS one* 14: e0209752

Prukop T, Wernick S, Boussicault L, Ewers D, Jäger K, et al. 2020. Synergistic PXT3003 therapy uncouples neuromuscular function from dysmyelination in male Charcot-Marie-Tooth disease type 1A (CMT1A) rats. *Journal of neuroscience research* 98: 1933-52

Raeymaekers P, Timmerman V, Nelis E, De Jonghe P, Hoogendijk JE, et al. 1991. Duplication in chromosome 17p11.2 in Charcot-Marie-Tooth neuropathy type 1a (CMT 1a). The HMSN Collaborative Research Group. *Neuromuscular disorders : NMD* 1: 93-7

Rasband MN, Tayler J, Kaga Y, Yang Y, Lappe-Siefke C, et al. 2005. CNP is required for maintenance of axon-glia interactions at nodes of Ranvier in the CNS. *Glia* 50: 86-90

Ravera S, Nobbio L, Visigalli D, Bartolucci M, Calzia D, et al. 2013. Oxydative phosphorylation in sciatic nerve myelin and its impairment in a model of dysmyelinating peripheral neuropathy. 126: 82-92

Rich LR, Brown AM. 2018. Fibre sub-type specific conduction reveals metabolic function in mouse sciatic nerve. *The Journal of physiology* 596: 1795-812

Riethmacher D, Sonnenberg-Riethmacher E, Brinkmann V, Yamaai T, Lewin GR, Birchmeier C. 1997. Severe neuropathies in mice with targeted mutations in the ErbB3 receptor. *Nature* 389: 725-30

Rossor AM, Evans MR, Reilly MM. 2015. A practical approach to the genetic neuropathies. *Practical neurology* 15: 187-98

Rossor AM, Shy ME, Reilly MM. 2020. Are we prepared for clinical trials in Charcot-Marie-Tooth disease? *Brain research* 1729: 146625

Rossor AM, Tomaselli PJ, Reilly MM. 2016. Recent advances in the genetic neuropathies. *Current opinion in neurology* 29: 537-48

Sahenk Z, Mendell JR. 1999. Alterations in Nodes of Ranvier and Schmidt-Lanterman Incisures in Charcot-Marie-Tooth Neuropathies. 883: 508-12

Saher G, Quintes S, Möbius W, Wehr MC, Krämer-Albers EM, et al. 2009. Cholesterol regulates the endoplasmic reticulum exit of the major membrane protein P0 required for peripheral myelin compaction. *The Journal of neuroscience : the official journal of the Society for Neuroscience* 29: 6094-104

Sandelius Å, Zetterberg H, Blennow K, Adiutori R, Malaspina A, et al. 2018. Plasma neurofilament light chain concentration in the inherited peripheral neuropathies. *Neurology* 90: e518

Sango K, Kato K, Tsukamoto M, Niimi N, Utsunomiya K, Watabe KJJMGMS. 2014. Physiological and pathological roles of aldose reductase in Schwann cells. 1: 012

Sano H, Nakamura A, Yamane M, Niwa H, Nishimura T, Kojima M. 2020. The polyol pathway is a crucial glucose sensor in Drosophila. 2020.03.16.993170

Saporta MA, Katona I, Lewis RA, Masse S, Shy ME, Li J. 2009. Shortened internodal length of dermal myelinated nerve fibres in Charcot-Marie-Tooth disease type 1A. *Brain : a journal of neurology* 132: 3263-73

Sereda M, Griffiths I, Pühlhofer A, Stewart H, Rossner MJ, et al. 1996. A transgenic rat model of Charcot-Marie-Tooth disease. *Neuron* 16: 1049-60

Sereda MW, Meyer zu Hörste G, Suter U, Uzma N, Nave KA. 2003. Therapeutic administration of progesterone antagonist in a model of Charcot-Marie-Tooth disease (CMT-1A). *Nature medicine* 9: 1533-7

Shy ME, Blake J, Krajewski K, Fuerst DR, Laura M, et al. 2005a. Reliability and validity of the CMT neuropathy score as a measure of disability. *Neurology* 64: 1209

Shy ME, Lupski JR, Chance PF, Klein CJ, Dyck PJ. 2005b. Chapter 69 - Hereditary Motor and Sensory Neuropathies: An Overview of Clinical, Genetic, Electrophysiologic, and Pathologic Features In *Peripheral Neuropathy (Fourth Edition)*, ed. PJ Dyck, PK Thomas, pp. 1623-58. Philadelphia: W.B. Saunders

Siems SB, Jahn O, Eichel MA, Kannaiyan N, Wu LMN, et al. 2020. Proteome profile of peripheral myelin in healthy mice and in a neuropathy model. *Elife* 9

Simpson IA, Dwyer D, Malide D, Moley KH, Travis A, Vannucci SJ. 2008. The facilitative glucose transporter GLUT3: 20 years of distinction. *American journal of physiology. Endocrinology and metabolism* 295: E242-53

Smith CM, Cooksey E, Duncan ID. 2013. Myelin Loss Does Not Lead to Axonal Degeneration in a Long-Lived Model of Chronic Demyelination. 33: 2718-27

Soldevilla B, Cuevas-Martín C, Ibáñez C, Santacatterina F, Alberti MA, et al. 2017. Plasma metabolome and skin proteins in Charcot-Marie-Tooth 1A patients. *PloS one* 12: e0178376

Srinivasan S, Avadhani NG. 2012. Cytochrome c oxidase dysfunction in oxidative stress. *Free Radical Biology and Medicine* 53: 1252-63

Stathopoulos P, Alexopoulos H, Dalakas MC. 2015. Autoimmune antigenic targets at the node of Ranvier in demyelinating disorders. *Nature reviews. Neurology* 11: 143-56

Stecker MM, Stevenson M. 2014. Effect of glucose concentration on peripheral nerve and its response to anoxia. *Muscle & nerve* 49: 370-7

Stuart CA, Wen G, Peng BH, Popov VL, Hudnall SD, Campbell GA. 2000. GLUT-3 expression in human skeletal muscle. *American Journal of Physiology - Endocrinology and Metabolism* 279: E855-E61

Stumpf SK, Berghoff SA, Trevisiol A, Spieth L, Düking T, et al. 2019. Ketogenic diet ameliorates axonal defects and promotes myelination in Pelizaeus–Merzbacher disease. *Acta Neuropathologica* 138: 147-61

Svaren J, Moran JJ, Wu X, Zuccarino R, Bacon C, et al. 2019. Schwann cell transcript biomarkers for hereditary neuropathy skin biopsies. 85: 887-98

Tao-Cheng JH, Rosenbluth J. 1983. Axolemmal differentiation in myelinated fibers of rat peripheral nerves. *Brain research* 285: 251-63

Tasaki I. 1939. THE ELECTRO-SALTATORY TRANSMISSION OF THE NERVE IMPULSE AND THE EFFECT OF NARCOSIS UPON THE NERVE FIBER. 127: 211-27

Taveggia C, Zanazzi G, Petrylak A, Yano H, Rosenbluth J, et al. 2005. Neuregulin-1 type III determines the ensheathment fate of axons. *Neuron* 47: 681-94

Traka M, Dupree JL, Popko B, Karagogeos D. 2002. The neuronal adhesion protein TAG-1 is expressed by Schwann cells and oligodendrocytes and is localized to the juxtaparanodal region of myelinated fibers. *The Journal of neuroscience : the official journal of the Society for Neuroscience* 22: 3016-24

Trevisiol A, Kusch K, Steyer AM, Gregor I, Nardis C, et al. 2020. Structural myelin defects are associated with low axonal ATP levels but rapid recovery from energy deprivation in a mouse model of spastic paraplegia. *PLOS Biology* 18: e3000943

Trevisiol A, Saab AS, Winkler U, Marx G, Imamura H, et al. 2017. Monitoring ATP dynamics in electrically active white matter tracts. *eLife* 6: e24241

van Hameren G, Campbell G, Deck M, Berthelot J, Gautier B, et al. 2019. In vivo real-time dynamics of ATP and ROS production in axonal mitochondria show decoupling in mouse models of peripheral neuropathies. *Acta Neuropathologica Communications* 7: 86

Véga C, Martiel JL, Drouhault D, Burckhart MF, Coles JA. 2003. Uptake of locally applied deoxyglucose, glucose and lactate by axons and Schwann cells of rat vagus nerve. *The Journal of physiology* 546: 551-64

Viader A, Golden JP, Baloh RH, Schmidt RE, Hunter DA, Milbrandt J. 2011. Schwann cell mitochondrial metabolism supports long-term axonal survival and peripheral nerve function. *The Journal of neuroscience : the official journal of the Society for Neuroscience* 31: 10128-40

Viader A, Sasaki Y, Kim S, Strickland A, Workman CS, et al. 2013. Aberrant Schwann cell lipid metabolism linked to mitochondrial deficits leads to axon degeneration and neuropathy. *Neuron* 77: 886-98

Villani G, Attardi G. 2000. In vivo control of respiration by cytochrome c oxidase in human cells. *Free radical biology & medicine* 29: 202-10

Wang H, Davison M, Wang K, Xia T-H, Kramer M, et al. 2020. Transmembrane protease serine 5: a novel Schwann cell plasma marker for CMT1A. 7: 69-82

Wang W, Guedj M, Bertrand V, Foucquier J, Jouve E, et al. 2017. A Rasch Analysis of the Charcot-Marie-Tooth Neuropathy Score (CMTNS) in a Cohort of Charcot-Marie-Tooth Type 1A Patients. *PloS one* 12: e0169878

Wanner IB, Guerra NK, Mahoney J, Kumar A, Wood PM, et al. 2006. Role of N-cadherin in Schwann cell precursors of growing nerves. *Glia* 54: 439-59

Webster HD, Martin R, O'Connell MF. 1973. The relationships between interphase Schwann cells and axons before myelination: a quantitative electron microscopic study. *Developmental biology* 32: 401-16

Weil M-T, Heibeck S, Töpperwien M, tom Dieck S, Ruhwedel T, et al. 2018. Axonal Ensheathment in the Nervous System of Lamprey: Implications for the Evolution of Myelinating Glia. *The Journal of Neuroscience* 38: 6586

Winseck AK, Oppenheim RW. 2006. An in vivo analysis of Schwann cell programmed cell death in embryonic mice: the role of axons, glial growth factor, and the pro-apoptotic gene Bax. *The European journal of neuroscience* 24: 2105-17

Woldeyesus MT, Britsch S, Riethmacher D, Xu L, Sonnenberg-Riethmacher E, et al. 1999. Peripheral nervous system defects in erbB2 mutants following genetic rescue of heart development. *Genes & development* 13: 2538-48

Wolpowitz D, Mason TB, Dietrich P, Mendelsohn M, Talmage DA, Role LW. 2000. Cysteine-rich domain isoforms of the neuregulin-1 gene are required for maintenance of peripheral synapses. *Neuron* 25: 79-91

Woodhoo A, Alonso MB, Droggiti A, Turmaine M, D'Antonio M, et al. 2009. Notch controls embryonic Schwann cell differentiation, postnatal myelination and adult plasticity. *Nature neuroscience* 12: 839-47

Yabe-Nishimura C. 1998. Aldose reductase in glucose toxicity: a potential target for the prevention of diabetic complications. *Pharmacological reviews* 50: 21-33

Yang J, Liu J, Zhang S, Yang Y, Gong JJTCR. 2018. The overexpression of cytochrome c oxidase subunit 6C activated by Kras mutation is related to energy metabolism in pancreatic cancer. *2018* 7: 290-300

Yellen G. 2018. Fueling thought: Management of glycolysis and oxidative phosphorylation in neuronal metabolism. *The Journal of cell biology* 217: 2235-46

Yin X, Crawford TO, Griffin JW, Tu P, Lee VM, et al. 1998. Myelin-associated glycoprotein is a myelin signal that modulates the caliber of myelinated axons. *The Journal of neuroscience : the official journal of the Society for Neuroscience* 18: 1953-62

Young CD, Lewis AS, Rudolph MC, Ruehle MD, Jackman MR, et al. 2011. Modulation of Glucose Transporter 1 (GLUT1) Expression Levels Alters Mouse Mammary Tumor Cell Growth In Vitro and In Vivo. *PloS one* 6: e23205

Yu T, Sheu SS, Robotham JL, Yoon Y. 2008. Mitochondrial fission mediates high glucose-induced cell death through elevated production of reactive oxygen species. *Cardiovascular research* 79: 341-51